Compact array emitters for terahertz spectroscopy and imaging

Sørensen, Christian Buhl

Publication date:
2019

Document Version
Publisher's PDF, also known as Version of record

COMPACT ARRAY EMITTERS FOR TERAHERTZ SPECTROSCOPY AND IMAGING

BY
CHRISTIAN BUHL SØRENSEN

DISSERTATION SUBMITTED 2019

AALBORG UNIVERSITY
DENMARK

Compact array emitters for terahertz spectroscopy and imaging

Ph.D. Dissertation

Christian Buhl Sørensen

Dissertation submitted December 30th, 2019

Dissertation submitted: December 30, 2019

PhD supervisor: Assoc. Prof. Esben Skovsen
Aalborg University

PhD committee: Associate Professor Vladimir Popok (chairman)
Aalborg University

Professor Peter Uhd Jepsen
DTU Photonics

Professor Daniel Mittleman
Brown University, New England

PhD Series: Faculty of Engineering and Science, Aalborg University

Department: Department of Materials and Production

ISSN (online): 2446-1636
ISBN (online): 978-87-7210-577-2

Published by:
Aalborg University Press
Langagervej 2
DK – 9220 Aalborg Ø
Phone: +45 99407140
aauf@forlag.aau.dk
forlag.aau.dk

Printed in Denmark by Rosendahls, 2020

Abstract

Electromagnetic radiation in the terahertz frequency range is a useful tool for many security applications, but the technique's most distinct drawback is the absence of intense compact sources. This thesis presents significant steps toward an integrated array of discrete antennas, by employing an etched substrate lens array with an array pitch similar to the free space wavelength. A peak 10 dB increase in the signal to noise ratio was demonstrated near 0.5 THz, and the emitted power was doubled between 0.4 THz and 0.75 THz. It was further demonstrated that the echos from the flat substrate were reduced. The reproducibility of performance metrics was improved through three generations of antennas. The combination substrate is motivated as a future key-enabling technology for dense arrays of emitters.

Furthermore, the spatial emission profile of terahertz radiation from two-color air plasma filaments has been characterized. It was demonstrated that significant care is required in selection and implementation of filters to remove forward-propagating visible light from the generated beam. When using a silicon filter, a conical emission pattern was induced, but when preceding the silicon filter with a high bandgap ceramic filter, a Gaussian-like emission pattern was observed. The observed conical emission pattern was consistent with previous reports claiming an intrinsic conical emission profile from similar plasma filaments. The fine details of the conical profile recorded here were further consistent with simulations of diffraction around a central occlusion in the silicon filter.

Finally, additive manufacturing of low cost reflective optics are presented as a viable option for the comparatively long wavelengths of terahertz. An off-axis parabolic mirror with an effective focal length of 150 mm, and a diameter of 100 mm is used as a test platform. Subsequent manual polishing provides a surface roughness that support up to 10 THz, while the geometric shape of the curved surface support 2-3 THz. Sputter coating is used to apply a gold surface that reflects the electromagnetic radiation.

Resumé

Elektromagnetisk stråling i frekvensområdet terahertz er et nyttigt værktøj i mange sikkerhedstekniske brugsområder, men teknikkernes tydeligste mangel ligger i fraværet af intense, kompakte kilder. Denne tese præsenterer signifikante skridt mod et integreret array af diskrete antenner, ved at benytte et tilsvarende sæt linser ætset ind i bagsiden af substratet. Den realiserede antenne-antenne afstand havde samme størrelsesorden som bølgelængden for det frit propagerende lys. En maksimal forøgelse på 10 dB af signal/støjforholdet blev demonstreret ved 0,5 THz, og den udstrålede effekt var fordoblet mellem 0,4 THz og 0,75 THz. Yderligere blev det demonstereret at ekkoerne fra de flade substrater var reducerede. Reproducerbarheden af ydelsesparametre er blevet forbedret gennem tre generationer af antenner. Kombinationssubstratet motiveres som en fremtidig nøgle-teknologi for kompakte arrays af kilder.

Yderligere er den rumlige udstrålingsprofil af terahertz stråling fra tofarve plasmastrenge i luft blevet karakteriseret. Det demonstreres at stor omhyggelighed er nødvendig i valget og implementeringen af filtre til at fjerne fremadrettet synligt lys fra den genererede stråle. Brugen af et silicium filter inducerer en konisk udstrålingsprofil, men da et keramisk filter med stort båndgab blev placeret foran, blev en Gauss-lignende udstrålingsprofil observeret. Den afbillede koniske udstrålingsprofil var konsistent med tidligere publikationer der foreslog en iboende konisk udstrålingsmekanisme fra lignende filamenter. De finere detaljer i den koniske profil der er dokumenteret her, var yderligere konsistente med simuleringer af diffraktion fra en central blokering i silicium filteret.

Sidst, men ikke mindst, er additiv fabrikation af billig refleksiv optik præsenteret som en brugbar mulighed, for de forholdsvist lange bølgelængder for terahertz stråling. Et vinklende parabolspejl med en effektiv fokallængde på 150 mm, og en diameter på 100 mm blev brugt som test emne. Påfølgende manuel polering gav en overfladeruhed på emner der understøttede op til 10 THz, mens den geometriske form på den krumme overflade oppebar 2-3 THz. Sputter coating blev benyttet til at påføre et guldlag der reflekterede den elektromagnetiske stråling.

Acknowledgements

I am sincerely grateful for all the help I have received during this project. The academic support and the possibility of this work has come from my supervisor Associate Professor Esben Skovsen. The funding was provided by the Independent Research Fund Denmark, for the CITS project (DFF-6111-00119).

Furthermore, I am deeply grateful for the supervision and time spent by Professor Emmanuel Abraham - Merci bien. There is of course no mention of Emmanuel, without his partner in crime Jérôme Degert. It has been a pleasure to learn from you both.

I would like to thank our collaborators at University of Southern Denmark, Jacek Fiutowski and Arkadiusz Goszczak for fabrication of the substrate lens arrays.

Tremendous thanks are due for the full staff at the physics group at Aalborg University. The continued support and help from the scientific, technical and administrative staff has been heartwarming. Especially Mathias Kristensen and Pawel Cielecki, for making the office a fun and pleasant place to be at. I've enjoyed discussions and help from You, to no end.

My dear friends and co-workers Pawel Cielecki, Bjarke Jensen, Kristoffer Piil and Kristian Kjærgaard have helped me greatly with the revision of the thesis. Your help has raised the quality considerably.

I owe my dearest Anne a lifetime of gratitude for keeping me sane, and Sigma for always being cheerful and excited to see me.

I am sure that I have forgotten some names, but I will forever be thankful for your help.

Contents

Preface

This thesis is the result of the work performed by the author, in the three year research project *Compact Integrated Terahertz Sources*. The project was funded by the Independent Research Fund Denmark, and was part of a research consortium between Aalborg University, Aarhus University, University of Southern Denmark and the danish company MyDefence.

This thesis shows the first experimental results from the terahertz group at Aalborg University, and documents the journey from severely limited single point emitters, to the characterization of arrayed emitters with significantly higher output.

A research stay was carried out at University of Bordeaux in the Laboratoire Ondes et Matière d'Aquitaine, where the author participated in and led experimental work on fundamental characterization of complementary high-intensity pulsed sources of terahertz radiation. The research stay was four months from October 2018, at the invitation of Professor Emmanuel Abraham. Partial funding was obtained from the PhD mobility grant from the LAPHIA Cluster of Excellence.

Christian Buhl Sørensen
Aalborg University, December 30, 2019.

Thesis Structure

The thesis is structured in five chapters. While each chapter may be read individually, the introduction and concluding chapters will provide context, similarities and overall conclusions to the work. Each chapter begins with an introduction to the relevant themes, and ends with a discussion of the results. The conclusions are formalized in the last chapter.

I **Introduction:** The project context is presented, along with the formal research aims. Theory on the methods of terahertz generation and detection which apply to the work in this thesis is presented.

II **Arrayed Photoconductive emitters:** A significant part of the CITS project aims towards antenna optimization, and their implementation into an array.

III **Two-color plasma terahertz generation:** This section describes the work performed during the external research stay, which experimentally characterizes the emission of terahertz radiation from a two-color plasma.

IV **Low cost fabrication of optical components:** The work with the two-color plasma indicated a need for low cost bespoke optical components for the terahertz range of frequencies.

V **Synthesis and conclusion:** The work is concluded, and suggestions for future work is offered.

Appendices include the papers and abstracts for conferences that were submitted during the project, as well as the cleanroom standard operating procedures for fabrication of the antennas. Furthermore the design of a balanced photodiode amplifier is also provided.

The citation style used throughout the thesis is e.g. [1], and the list of references is provided before the appendices.

Mentions of "optical" and "visible" wavelengths broadly corresponds to between 200 nm and 1100 nm, and "terahertz" wavelengths are in a broad sense assumed to be between 30 μm and 3 mm.

Part I

Introduction

1 Project context

The aim of this project is to develop emitters of terahertz (THz) radiation, for use in security, defense and military applications. Contemporary challenges for armed forces in confrontation zones and security screening in e.g. airports motivate the development towards stand-off detection systems for explosives in improvised explosive devices, concealed weapons and controlled substances.

Furthermore, developments in the application of unmanned vehicles and their payload allowances also indicate a favourable opportunity to develop terahertz sources and detectors for mobile applications.

1.1 Stand-off detection with THz radiation

Terahertz radiation lies between infrared radiation and microwave radiation. With a wavelength of 3 µm to 1000 µm, it has enticing potential in its interaction with complex molecules.

It has been shown that this particular range of wavelengths are useful for identifying explosives[2], concealed weapons[3] and controlled substances, using reflection and transmission spectroscopy. The comparatively short wavelength provides reasonable spatial resolution, allowing imaging of e.g. printed and handwritten letters inside envelopes[3]. While near-infrared and Raman spectroscopy may also provide similar results in detection and identification, it has also been demonstrated that terahertz enables measurements through clothes[4] and common packaging materials[5], further inspiring work on security applications.

Work on remote sensing with terahertz is still in development, but positive identification of samples of high energy explosives was demonstrated almost 15 years ago[6], and a type of explosive (RDX) had the broad peak around 0.85 THz detected at a 30 m distance at 56% relative humidity[7]. Detection of landmines have also been hypothesized, and it was shown that imaging of metal elements is possible through up to 3 cm of sand[8]. Relatively recently, the issue of waterlines were treated; while the humidity in air is strongly absorbing in several bands in the terahertz range, it was demonstrated that dense fog does not lead to other spectral components or shifts, over long distances[9].

While the potential is clear, a significant challenge lies in the signal budget. The electrical-optical conversion is still low for terahertz emitters, and absorption in air is significant. Thermal issues inhibit significant power scaling of conventional emitters e.g. photomixers[10], so alternative paths must be explored.

This thesis will work towards improving the power emission density of terahertz emitters, using arrays and small-pitch substrate lenses. A strong focus will be held on experimental verification and fabrication.

1.2 Research objectives

This section describes the research objectives for the core research project. Work on pulsed plasma sources and rapid prototyping of optical components has also been done during this project, and is considered secondary.

Developing optimal antenna geometries for narrowband continuous wave systems. The methodology is experimental realizations of combinations of emitter primitives, and broadband characterization with time-domain systems.

Developing a functional array geometry for 4 by 4 terahertz emitters. Experimental characterization with a time-domain system will be performed.

Characterize the performance gain from a substrate lens array. The methodology is experimental characterization of performance for arrays of lenses and single lenses.

2 Generation and detection of terahertz radiation

This section compares and discusses the fundamental theory underlying three popular methodologies for THz spectroscopy. The following technologies are discussed, but many more avenues for THz generation and detection are available. This work concerns itself purely with:

- Photoconductive antennas for generation and detection in time domain spectroscopy (TDS).
- Photomixers for generation and detection.
- two-color air-plasma generation and electro-optic sampling in crystals.

2.1 Generation with photoconductive antennas

The first photoconductive systems sparked attention in the 70s, with Auston et al.[11] showing sub-picosecond response times in switching a current through a silicon slab, very similar to the presently known photoconductive antennas. The first propagating pulses were measured by G. Mourou[12], and the time-domain measurements started to look like the emitter-detector measurements of contemporary THz TDS systems by 1984[13]. The latter half of the 80s saw the first time-domain spectroscopic measurements of $LiTaO_3$ showing the absorbance and refractive index up to 1.6 THz[14].

The field garnered momentum, and systems closely resembling todays showed up; van Exter et al.[15] performed measurements of the water absorption lines in atmospheric air, Birch et al.[16] measured the absorption and dispersion of high-density polyethylene (HDPE) and low-density polyethylene (LDPE), and Grischkowsky et al.[17] measured the optical constants in the THz range of relevant dielectrics and semiconductors. These papers laid the foundation for the most commonly used materials in THz optics and generation. Another essential paper was written by Jepsen et al.[18], describing a well fitting model for the generation and detection of terahertz radiation from pulsed emitters.

Optimizations were performed on the substrates. By 1995, low-temperature grown gallium arsenide (LT-GaAs) increased the available bandwidth significantly[19]. This work was done with the photomixing technique[20], where the oscillating electric field would be driven by the beat note between two closely spaced continuous wave (CW) lasers. The method is brie described in section 2.3. Further recent work has increased the signal-noise ratio (SNR) considerably, using multilayer heterostructures of InGaAs and InAlAs on InP-carriers[21].

Early photoconductive switch geometry were parallel coplanar waveguides, but different geometries were rapidly used for receiver and emitter antennas[22]. The work by Tani et al.[23] showed the three fundamental antenna types that were subsequently employed; the dipole antenna, the bow-tie antenna and the strip line antenna. It was found that the bandwidth was higher for the stripline (approximately 4 THz), slightly lower for the dipole antenna (3 THz) and somewhat lower yet for the bow-tie (3 THz, but high low-frequency intensity). The work on antennas for CW emitters split away and focused on resonant antennas, while the work on emitters in pulsed systems centered on materials with well-tailored lifetimes and mobilities.

Inspiration was found from the advanced possibilities of planar waveguide layouts, and Duffy et al. presented a significantly more complicated antenna geometry[24], with two dipoles, inductive chokes and an interdigitated excitation center. For antennas fabricated on low-temperature grown GaAs, the resonant dipoles are experimentally shown to be narrow-band, with a frequency roll-off of the potential performance that decays at 8 dB/octave – significantly less severe than their reference, a broadband spiral antenna. Furthermore the peak emission power was 6-10 dB higher. Substrate developments have led to very efficient CW systems, with an emission power of several μW[4]

The resonant antenna principle was further cemented when a full-width half maximum linewidth for a 400 GHz emitter was measured to have an upper bound of 80 GHz[25], with similar gains in power. Subsequent work on e.g. folded dipoles[26, 27] and travelling wave generators[28] has also been done. CW excitation at telecom wavelengths[29] was presented in an all-fiber implementation that drastically increased the robustness of a THz spectrometer. The phase information in the CW system can be extracted, using either a delay line or a fiber stretcher[30].

For the time-domain antennas, it has been shown that there is a potential for improvement by using plasmonic structures[31] to both improve the laser-substrate coupling, while also decreasing lifetimes of charge carriers. Improvements in terms of contact metallization has provided a two times higher output power at similar bandwidth by using optimal Au-Ge stacks[32], instead of a simple Ti-Au metallization.

2.1.1 Generation mechanism

Photoconductive antenna (PCA) systems are robust, low input power, pulsed systems that have been extensively used for TDS. The technology relies on a biased semiconductor substrate that undergoes rapid changes in conductivity, driven by a femtosecond (fs) laser pulse. The laser pulse has an energy higher than the bandgap of the semiconductor substrate, and thus generates charge carriers.

The charge carriers are accelerated by the bias field, and the resulting oscillation of charges radiates in the THz region of frequencies.

In a 1-dimensional model of the emission[33], the THz field radiated from a Hertzian dipole can be written in relation to the photocurrent $I_{PC}(t)$:

$$E_{THz}(t) = \frac{\mu_0 w_0}{4\pi} \frac{\sin\theta}{r} \frac{d}{dt}[I_{PC}(t_r)\hat{\theta}] \propto \frac{dI_{PC}(t)}{dt} \tag{1}$$

where μ_0 is the permeability (assumed 1 for the semiconductors in question), w_0 is the laser beam width in the interaction site, θ is the spatial angle from the interface, r is the distance from the interaction point and t_r is retarded (sampled) time instance. The time derivative relation was shown by[34].

Duvillaret et al.[35] reports an analytical description of the photocurrent, starting from a convolution of the optical pulse, and the conduction response function of the material:

$$I_{PC}(t) = P_{opt}(t) * [n_{em}(t) q v_{em}(t)] \tag{2}$$

where P_{opt} is the optical power, n_{em}, q, v_{em} is the density, the charge and the velocity of the generated photo-carriers, respectively. The last term is the conduction response function of the material, and is essentially the cumulated effect of the velocity of the charges, as a function of time.

The optical power is described by a gaussian pulse:

$$P_{opt}(t) = \frac{P_{avg}}{\tau_{laser}} \, \mathrm{e}^{-\frac{4\ln 2 (t-t')^2}{\tau_{laser}^2}} \tag{3}$$

where P_{avg} is the average laser power, τ_{laser} is the FWHM pulse width of the laser. Note that the primed time is introduced to define the laser pulse arrival time.

The charge carrier density can be modelled as a single decaying exponential function, for times $t > 0$ (after the comparatively zero-length pulse has arrived);

$$\frac{dn_{em}}{dt} = -\frac{n_{em}(t)}{\tau_{em}} \rightarrow n_{em}(t) \propto \, \mathrm{e}^{-\frac{t}{\tau_{em}}} \tag{4}$$

where τ_{em} is the charge carrier recombination time [35], colloquially known as the charge carrier lifetime [33]. Finally, the velocity of the charge carriers can be described by a Drude-Lorentz model;

$$\frac{dv(t)}{dt} = -\frac{v(t)}{\tau_s} + \frac{q}{m_{eff}} E(t) \tag{5}$$

Where τ_s is the momentum relaxation time, and m_{eff} is the effective mass. The Drude model contains two terms; a decelerating term due to collisions, and the accelerating term from the bias. Duvillaret et al. assumes a DC bias field $E(t)$.

The entire model, convolution included, results in the following expression for the current[35]:

$$I_{PC} \propto \int_0^\infty \frac{P_{avg}}{\tau_{laser}}\, \mathrm{e}^{-\frac{4\ln 2(t-t')^2}{\tau_{laser}^2}} \times \mathrm{e}^{-\frac{t'}{\tau_{em}}}\, \frac{\delta\tau}{m} \left(1-\mathrm{e}^{-\frac{t'}{\delta\tau}}\right) E_{DC}\, dt' \tag{6}$$

The model indicates a very important result, as a dominant part of the temporal performance of a photoconductive emitter is driven by the laser risetime, whereas the decay is described by the material parameters.

The amplitude is dependent on the effective mass of the charge carriers (lower is better), the charge carrier lifetime (shorter is better), the bias field (higher is better), optical power (higher is better) and the optical pulse length (shorter is better).

Note that the model neglects the dispersion of the rest of the optical system for detection, as well as all interfaces between the semiconductor substrate and the surrounding air.

2.2 Detection with photoconductive antennas

The principle for time domain detection of THz waves relies on similar physics as the emission. A probe beam from a femtosecond laser source excites charge carriers. Instead of an external bias field supplied from a voltage source, a current is driven by an incoming THz electric field. By incurring different delays between the incoming THz driving pulse and the probe beam generating the photocarriers, the THz pulse is mapped out in time. The current is measured with a high gain current amplifier, as usual magnitudes are on nano-ampere scale.

It follows from the phenomenological description that the decay of photoexcited charge carriers limits the temporal resolution, as a long lifetime will average the THz field. The current is the convolution of the transient surface conductivity ($\sigma_{surf}(t)$) and the incoming electric field ($E_{THz}(t)$)[33]:

$$J(t) = \int_{-\infty}^{t} \sigma_{surf}(t-t')E_{THz}(t')\, dt' \tag{7}$$

The frequency-domain equivalence of the convolution is a multiplication, and this formalizes that the sampled THz signal is bandwidth limited by the frequency response of the surface conductivity. A geometric term should be included in the convolution, as the diffraction limited spotsize is larger for low frequencies[18]. The THz power per active detector volume will be smaller, and the detector response function will tend to zero at low frequencies.

The resulting convolution can be rewritten to a convolution of an impulse response function for the material and geometry, and a probe laser response function[36]:

$$J(t) = \int_{-\infty}^{t} \frac{\mu_{dc} e E_{THz} \eta \phi}{\phi - 1/\tau_c} \left(e^{-t^*/\tau_c} - e^{-t^*\phi} \right) \quad I_{opt}(t')\, dt' \tag{8}$$

where $t^* = t - t'$, $\phi = 1/\tau_s$, μ_{dc} is the dc mobility, η is an absorption efficiency of the material, and I_{opt} is the probe beam intensity.

2.3 Photomixers

Photomixer technology is complementary to the photoconductive emitters; by using the beat-note from two accurately tuned lasers, the difference frequency excites a biased semiconductor. The bias acts as the acceleration field, for the photo-generated charge carriers, and the time-derivative of the current radiates in the THz range.

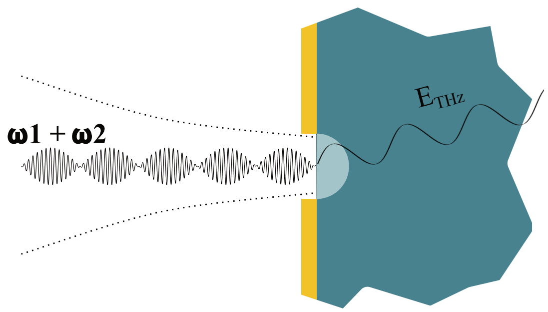

Fig. 1: Sketch of the photomixer principle. A mix of two beams ($\omega 1$ and $\omega 2$), excites a semiconductor slab (dark teal). A bias E_{DC} is provided by the two electrodes (yellow). The resulting oscillating field is emitted at the beat note frequency $\Omega_{THz} = \omega 1 - \omega 2$

Inherently similar to the PCA emitters, the emitted electric field is proportional to the first time-derivative of the photocurrent. As with the PCAs, the Drude-Lorentz model describes the key properties, and the photocurrent is still the convolution of the optical excitation (the difference frequency effective electric field) and the decay/generation mechanism described in eq. 2 and eq. 5. Here, however, the optical power is power of the beat frequency.

The key difference is in the continuous-wave (CW) nature of the excitation. As the rate of change of the charge carrier density does not have the rising edge of the femtosecond pulse to rely on, the efficiency of the emitter is much more tightly bound to the recombination rate in the semiconductor.

With the presumption that the collision lifetime is significantly shorter than the lifetime, the convolution may be simplified[33] to get the photomixer current:

$$I_{pm}(t) = \tau_c \mu E_{dc} I_0 + \frac{\tau_c \mu E_{dc} I_{beat}}{\sqrt{1 + \Omega_{THz}^2 \tau_c^2}} \cos(\Omega_{THz} t + \Phi) \tag{9}$$

where the first term describes a DC current with I_0 is the average optical intensity, and the second term describes the AC part modulating the DC signal. Here I_{beat} is the beat intensity and $\Phi = \tan^{-1} \Omega_{THz}\tau_c$ is a phase delay from the finite carrier lifetime. The emitted power per frequency is the square of the time derivative;

$$P_{THz}(\Omega_{THz}) = \frac{1}{2} R_A \, E_{dc}^2 I_{beat}^2 \frac{\tau_c^2 \mu^2}{1 + \Omega_{THz}^2 \tau_c^2} \tag{10}$$

This introduces a radiation resistance (R_A), that corresponds to the real part of the antenna impedance. It may be developed in terms of a lumped element of the antenna[37]:

$$P_{THz}(\Omega_{THz}) = \frac{1}{2} \frac{\tau_c \mu E_{dc} I_{beat}}{1 + \Omega_{THz}^2 \tau_c^2} \frac{R_A}{1 + \Omega_{THz}^2 R_A^2 C_A^2} \tag{11}$$

where the antenna capacitance is introduced as (C_A) for a dipole. It follows that a high radiation resistance is necessary for a large output power, but that it also defines the onset of the high frequency roll-off. The low-frequency approximation is that of a current source. Furthermore, the radiation resistance may be designed to be frequency dependent, as seen in[24], where it is argued that inductive elements compensate the capacitance. This increases the effective radiation resistance at resonance, consequently increasing the conversion efficiency by improving the impedance match.

2.4 Plasma sources

A relatively recent generation method is the two-color plasma generation technique. While the first generation of weak THz pulses with a gas medium was reported by Hamster et al. in 1993[38], subsequent developments have massively improved the generation efficiency. Cook and Hochstrasser showed that a high-intensity pump beam (800 nm, ω) from a regenerative amplifier and its second harmonic may be focused into air[39], to generate broad band THz pulses. This leaves the generation decoupled from material parameters and phase matching conditions, and very large pulse energies are possible - scaling towards mW average power pulsed terahertz emission has been shown[40], and the bandwidth is generally considered to be limited by the laser pulse duration, approaching 100 THz[41]. The initial description[39] of the physics of the generation mechanism pointed towards a four-wave mixing scheme, but later works have emphasized the photo current model[42].

The second harmonic (2ω) was generated through a β-barium borate (BBO) crystal, and it was shown[43] that the walk-off between the ω and 2ω in the air was essential to the generation efficiency. As the air exhibits a weak dispersion, the difference in refractive index between 800 nm and 400 nm corresponds to maxima in THz generation efficiencies every 25 mm of displacement between the plasma center and the BBO position. A sketch of the experimental setup is provided in fig. 2.

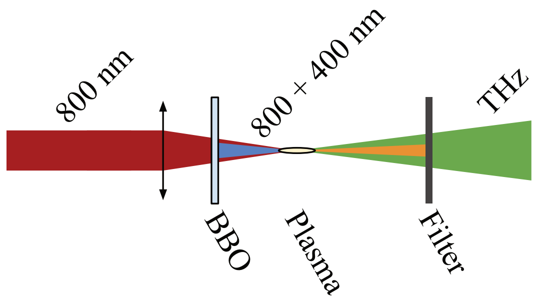

Fig. 2: Sketch of the two-color femtosecond plasma generation setup. The second harmonic is generated in the BBO crystal, and both wavelengths are propagated to the focal point. The generation occurs in the plasma. Both THz (green) and broadband light is generated in the plasma. Popularly, silicon filters are employed to remove the broad band light.

The generation mechanism was described as a transient photocurrent[44], which is driven by the asymmetrical electrical fields from the sum of the two pump beam components. Figure 3 illustrates the temporal evolution that lead to the generation. Three cases are shown in fig. 3 a); only the ω field (green traces), the two-color electric field with a walk-off between the components of $\pi/2$ (orange trace), and the two-color field with zero walk-off at the plasma center (blue).

The generation scheme reported by Kim et al.[44] utilized the Ammosov-Delone-Krainov (ADK) model of tunnel ionization[45], to estimate the photo-generation rate of the free electron density in the generated plasma. This was summed (disregarding decay in a first-order approach) to an electron density [see fig. 3 b) and c)]. As the ADK generation rate relies on the exponential of the already huge intensity, it introduces high frequency content.

The available electron density is accelerated [fig. 3 d)] by the electric field, and it is observed that the timing between generation and the driving field introduces asymmetry in the transverse current. The orange trace will display a DC offset, which in its Fourier transform [fig. 3 e)] introduce higher intensities of low-frequency contents. In this regard, low-frequency contents is understood to be in THz, and not in PHz ranges.

As indicated in the model by Kim et al., the generated plasma will propagate and produce light at several wavelengths. Figure 4 show a picture of

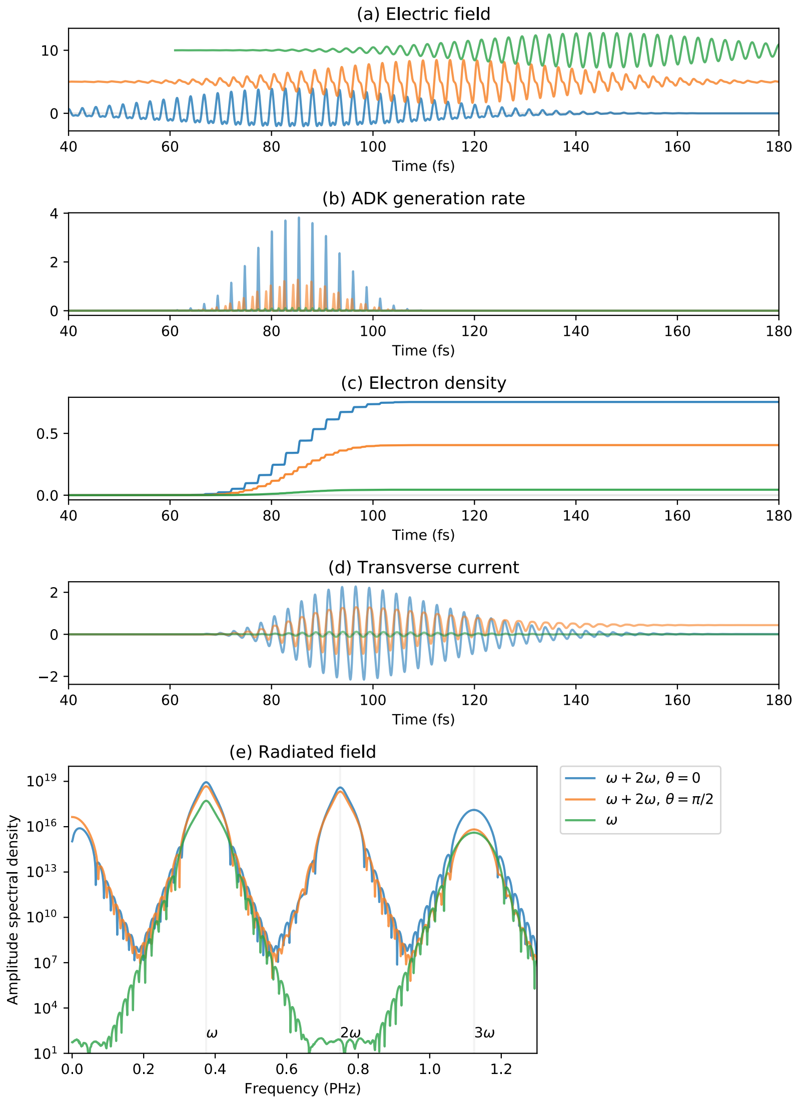

Fig. 3: The two-color plasma generation principle as described by[44]. The five parts show the combined electric field, the ADK electron generation rate[45], the free electron density, the transverse current and finally the Fourier transform of the transverse current. The waveforms have been calculated for three cases; 0 walk-off between ω and 2ω, optimal walk-off, and only the fundamental beam.

the forward propagated light from a two-color plasma source. Filters are employed in THz experiments, to remove the high-frequency visible light. High-resistivity float zone silicon filters are used in the majority of the available references. As the bandgap of silicon is around 1.1 eV, light with wavelengths below 1.1 µm will be absorbed or reflected.

Fig. 4: The plasma (out of focus blue/white spot in the left aperture) generates a broad selection of wavelengths that propagates beyond the plasma source.

2.5 Electro-optic sampling

Free space electro-optic sampling (EO-sampling) is performed by overlapping a pulsed THz field with a much shorter linearly polarized optical pulse in a field-dependent birefringent crystal material. The technique was reported by Wu in 1995[46] using a $LiTaO_3$ crystal. A sketch of the principle is shown in fig. 5.

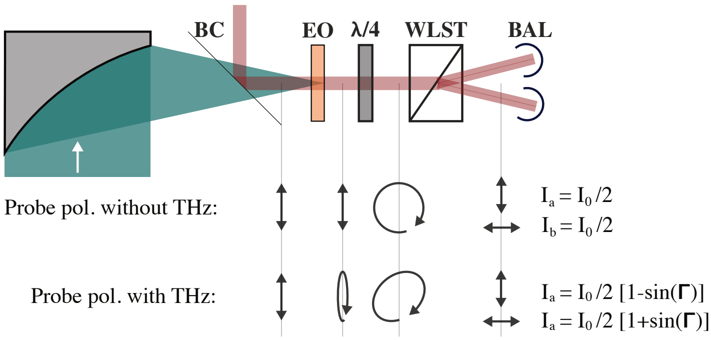

Fig. 5: The schematic for the electro-optic detection. Abbreviations: BC; Beam combiner, EO; Electro-optic crystal, $\lambda/4$; Quarter wave plate (QWP), WLST; Wollaston prism, BAL; Balanced photodiode pair.

Without any incident THz field, the linear polarization of the visible probe beam will pass through the electro-optic crystal unchanged, if intrinsic birefringence is disregarded. The quarter wave plate (QWP) retards one polarization to generate circularly polarized light. A polarizing beam element such as a Wollaston prism (WLST) is used to separate the two components of polarization, and direct the beams to two photodiode detectors in a balanced configuration. The absence of THz field gives identical intensity on both detectors with a net current of zero from the detectors.

An incident terahertz field will induce birefringence[33], according to:

$$\Gamma = \frac{\omega n_\omega^3 r_{41} L}{c} E_{THz} \tag{12}$$

where Γ is the phase retardation between the polarizations of the probe beam, ω is the frequency of the probe beam, n_ω is the refractive index at the probe wavelength, r_{41} is the electro-optic coefficient for the EO crystal, L is the thickness of the crystal, c is the speed of light and E_{THz} is the THz electric field.

The electro-optic coefficient is a material specific constant that describes the sensitivity of the bi-refringence. Table 1 show electro-optic constants for the most popular materials, zinc-telluride (ZnTe), gallium phosphide (GaP) and Gallium Arsenide (GaAs). While it may look beneficial to increase the thickness of the crystal, the dispersion between the probe beam and the THz beam will limit the bandwidth of a measurement in a thick crystal. The group velocity matched wavelength at 2 THz is also shown in tab. 1. For very thin EO crystals, the phase matching condition and the crystals phonon losses in the THz region are surpassed, and very high bandwidths are possible with this method[47].

Material	ZnTe	GaP	GaAs
$r_{41}\left[\frac{pV}{m}\right]$	4.8[48]	0.79[49]	1.5[48]
$\lambda_\omega[\mu m]$[50]	0.8	1.0	1.35

Table 1: Relevant material parameters for electro-optic crystals. r_{41} is the electro-optic coefficient and λ_ω is the group velocity matched wavelength for 2 THz.

The difference current is proportional to the intensity difference for reverse biased balanced photodiodes, and the intensity for the balanced setup is proportional to the sine of the phase retardation:

$$i_\Delta \propto I_\Delta = I_0 \sin\Gamma \tag{13}$$

For small intensities, where the observed modulation depth of the signal is small ($I_\Delta/I_0 \ll 1$), the small angle approximation is in effect, and the differential current i_Δ is proportional to the phase retardation Γ, and further proportional to E_{THz}.

Several methods for beam combination (BC, fig. 5) is available. Here, a pellicle beam splitter is shown, but the THz radiation may be reflected on a indium-tin-oxide mirror while the probe beam is propagated through. For point-wise spectroscopic systems, an off-axis parabolic mirror (OAPM) with a pre-drilled hole in the probe direction is also commonly used.

Part II

Arrayed photoconductive emitters

3 Introduction

This chapter describes the work done on arrayed photoconductive emitters.

Three facets of the development has been investigated; the development of efficient, resonant single emitter antennas, and the development of their integration in a large scale array system. Finally, the integration of deep etched substrate lenses with the developed antenna substrates is demonstrated.

3.1 Array integration of terahertz emitters

Array integration of radio-frequency emitters have been applied and developed to a very mature stage, but the array implementation of terahertz emitters is still in the research stage. Generally, two approaches may be taken. The present industrialization of the terahertz emitters, both pulsed and CW, enables easy alignment of optical systems of several discrete emitter components in relative vicinity of each other. As can be seen in e.g.[51–53], the large diameter of the emitter packaging and outcoupling lenses limit the density of emitters and impose significant grating lobes.

The other branch of research is the integrated single-die approach, where several photoconductive antennas or photomixers are placed on the same substrate, and illuminated with structured light. These include large-area emitters (LAEs)[54] and discrete antenna emitter arrays (AEAs). Dohler et al.[55] developed a methodology to compare the two integrated approaches, and found that LAEs in their model had strong advantages in terms of side lobe suppression (due to the quasi-continuous nature of the array) and input power scaling.

The potential for optimization of the single emitter antennas for e.g. resonant responses has ensured that the ongoing development in the discrete antenna branch has been relevant. Previous work on single-die, discrete antenna arrays include early work[56], where a long linear array (64 emitters) of photoconductive emitters, operating at a frequency dependent on the pitch of the electrode array. It was tunable from 200 GHz up to 800 GHz, and emitted radiation in a four-clover pattern with lobe widths of 10°. A 3x3 array of dipole antennas with interdigitated excitation sites for continuous wave output, has also been presented[57]. At a target frequency of 400 GHz, the power emitted was increased by a factor of 1.75, from single antenna emission. Due to transverse inhomogeneity of the gaussian profile of the excitation beam, the estimated improvement was 2.35 times the single antenna power.

Array integration of more complex antenna geometries has been reported[58], where a 3x3 (pitch 500 µm) log-spiral emitter array, was fabricated and characterized with a hemispherical outcoupling lens. With a total delivered optical pump power of 320 mW into the array, a radiated power of 1.9 mW was reported within a frequency span of 0.1 THz to 2 THz. The impressively high optical to THz efficiency of the emitters is testament to the continuous development of emitters with plasmonic-effect excitation area geometries([31, 59, 60]).

Recently, the application of THz in communication technology motivated[61] the development of a robustly scalable chess-board array with higher density single emitters. The described topology was reported to allow generous scaling towards larger arrays with potentially very small array pitch, but experimental data has not been found.

3.2 Enabling technologies for discrete antenna arrays

While the LAEs excel in power scaling, the development of laser sources on photonic integrated circuits may provide groundbreaking advantages for full system miniaturization. The rapidly maturing technology of telecom wavelength, indium phosphide (InP) PICs was leveraged by Theurer et al.[62] to develop a laser source comprising of two distributed feedback lasers that would drive a CW system between 800 GHz and 1.4 THz, with a signal-to-noise ratio of more than 40 dB. The area of the developed laser source was 4 mm by 400 µm, including the necessary 3 dB coupler for mixing of the two laser sources.

The scaling in laser source volume holds promise for ultra-tightly integrated terahertz emitters and detectors. While the power output of the planar technology InP is rather limited for generic foundry services (3.5 mW[63]), there is a significant potential for scaling, with off-chip powers of 80 mW reported[64]. The lower available optical power is however well suited to the discrete antenna arrays. The first demonstration of PIC sources for terahertz emitters was shown in 2016[65], and data transmission at 100 and 113 GHz was verified.

While the array integration and decrease in size of the backend (the laser source and antenna arrays) has been ongoing, the frontend (outcoupling geometry) is ripe for further development. It was previously motivated[66] that the emitter front end should be comprised of several small lenses. The performance of the conventional single lens decays significantly for arrays larger than the THz wavelength in the substrate. However, the long wavelength of THz radiation permits relatively simple fabrication of deep etch structures which have an arbitrary effective index due to voids. This principle was explored in the simulations by Brincker et al.[1], where gradient index lenses were designed, that would be etched directly into the substrate of the antenna substrates. Contemporary tolerances in backside alignment of lithography masks would allow very large scale integration technologies to aid in fabrication and alignment of arrayed lenses. Gradient index lenses may also have applications as free space components, and can be fabricated by modern additive manufacturing methods[67].

4 Modeling using linear superposition of sources

The simplest model of antenna arrays is the linear superposition of identical sources where the electric field may be added from N monochromatic coherent sources, by simply taking the phase into account[68]. When adding isotropic point sources this sum results in what is widely referred to as the Array Factor (AF). The array factor is the sum of the electric field contributions from a specified array of N emitters in points on a sphere in the far field:

$$AF = \sum_{n=1}^{N} W_n e^{-j\mathbf{k}\mathbf{r_n}+\phi_n} \tag{14}$$

where W_n is the amplitude weight of each emitter, $\mathbf{k}$ is the wave vector and $\mathbf{r}_n$ is the euclidean distance between the sampling point on the sphere and the emitter position. A phase ϕ_n may be added for each emitter.

To provide a simple model of the advantages in a terahertz emitter array, calculations of the array factor map are shown in the following pages. The summation is done in a far field sphere, 1 m from the center of the array. A 5x5 rectilinear array of isotropic emitters is added, with a transverse pitch of 500 µm. The spherical maps are calculated for frequencies of 0.1 THz, 0.5 THz, and 1 THz, and are shown in fig. 7. Note that the model corresponds to the emission patterns for an array inside an infinite substrate. Severe grating lobes is observed for 500 GHz and 1 THz. These occur as the array pitch is greater than $\lambda/2$, where the wavelength inside the substrate is decreased by the refractive index ($n_{GaAs} = 3.4$).

As it will be demonstrated, the array factor will generally improve the forward directivity. Controlling the phase contribution to each element (ϕ_n) enables beam steering, where the forward beam will change direction. The constructive interference of the individual sources will be stronger at different angles to the array plane. This is used in e.g. tracking radars to monitor several targets at periodically. It would also have potential in a stand-off detection and tracking use case.

The polar plots of the elevation angle (identical to the azimuthal direction for rectilinear arrays) is shown in fig. 6 a). The grating lobes are visible here, while the low frequency (100 GHz) does not exhibit grating lobes.

The simplest model for propagation out of the substrate is to apply Snells law of refraction, mapping the angles from a high-index medium to air. The result is shown in fig. 6 b), where it is evident that radiation at angles larger than approximately 17 degrees from the forward direction is lost due to internal refraction. Radiation at 100 GHz will propagate into a large spatial volume, while the higher frequencies have better directivity. It is seen that the forward emitted amplitude is scaled linearly by the number of emitters.

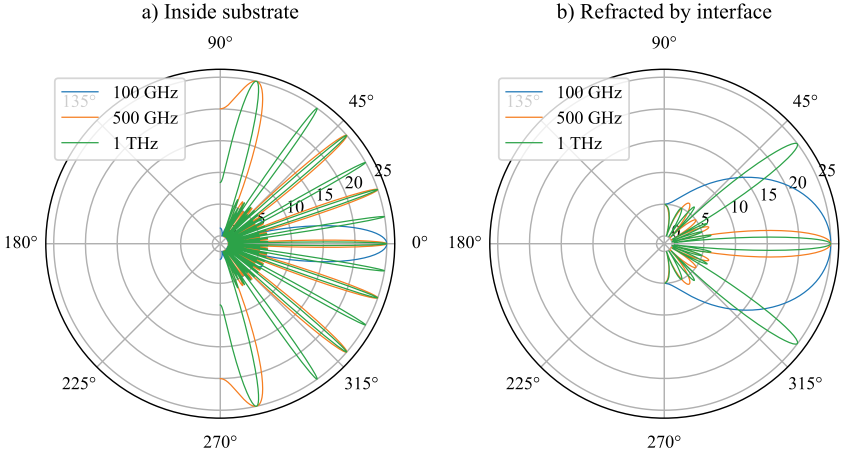

Fig. 6: a) Polar plot of electric field amplitude emitted by the array in the elevation angles from fig. 7. b) Polar plot of emission patterns for THz radiation from a 5x5 array, propagated out of the substrate by refraction.

The presented model may serve as a zero-order phenomenological motivation for implementing arrays. It is seen that the array will provide improved directivity at higher frequencies. It was also observed that the large-pitch array that was shown here will induce strong grating lobes. The model is limited, however; the assumption is that the far field radiation inside an infinite substrate is coupled out through a flat plane. What the model describes is the generation from isotropic point sources, summing in a far field sphere, and remapping this onto the internal surface of the antenna substrate. Here, the outpropagation is modelled by refraction.

The antenna will impose a radiation pattern and this will effectively be multiplied onto the array factor map. Finite element simulations may provide this map, and this could take the rear interface into account.

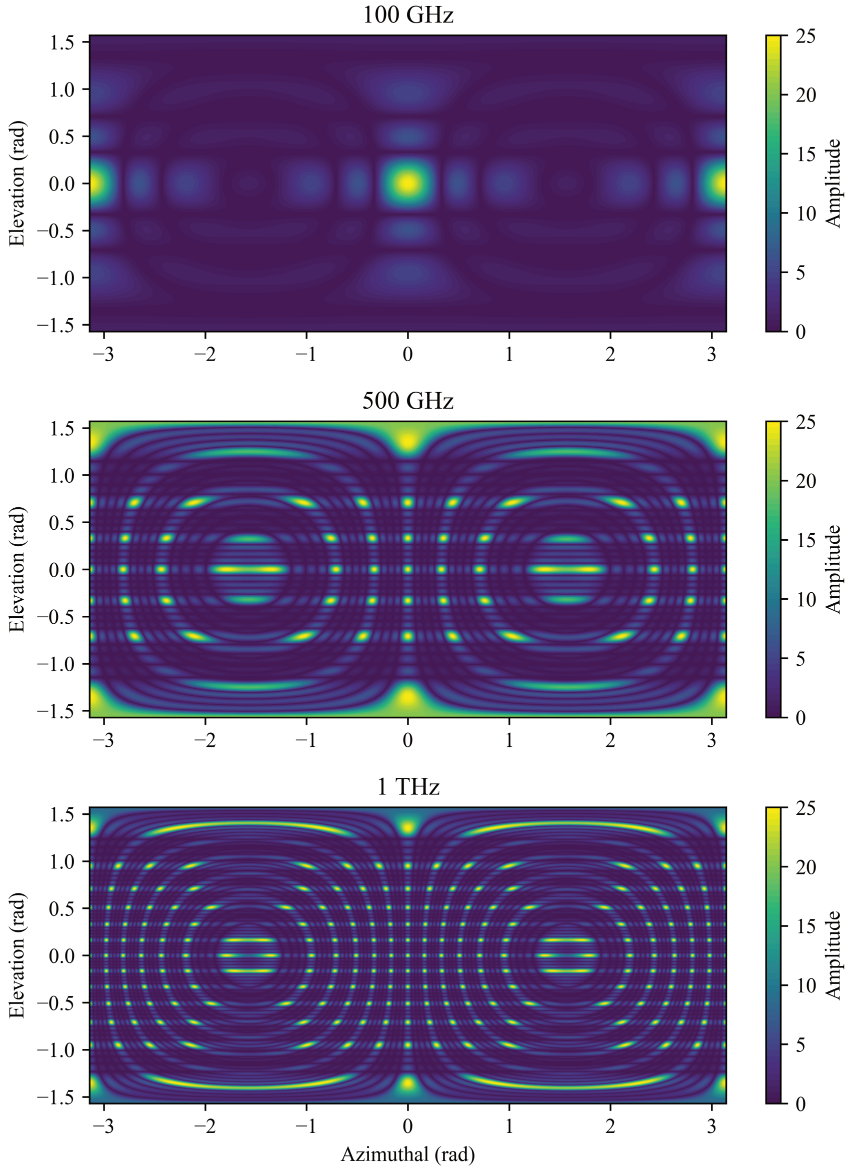

Fig. 7: Emission amplitude in an infinite substrate for three frequencies, from the 5x5 array of isotropic emitters with a pitch of 500 µm. The forward direction is in angles (0,0), and has a magnitude of 25 units.

5 Substrate lens fabrication

The requirement for outcoupling lenses has been identified as a limiting factor for array emitters. It has been noted previously (e.g.[69]) that the axial alignment should be within a few micrometers between the lens and emitter point. This alignment is intrinsically difficult if an array emitter is implemented, as a pitch larger than $\lambda_{THz}/2/n$ will enable unwanted grating lobes. As conventional hemispheric lenses are in the order of mm to cm in diameter, each emitter will not have its own lens. A breakthrough technology was published by Brincker et al.[1], where the idea of a effective refractive index lens etched into the backside of the emitter was presented.

Anisotropic etch technologies may be used to etch deep features in silicon, retaining almost completely vertical sidewalls. This is utilized to etch several deep grooves of varying transverse duty-cycle, mimicing the effective refractive index of a conventional lens.

Later work([70] and [71], manuscript submitted) has presented small cylindrical structures with similar performance to the grooved lens. The outcoupling efficiency is reported to improve by 3 times, and showing significantly improved emission patterns for the engineered structures.

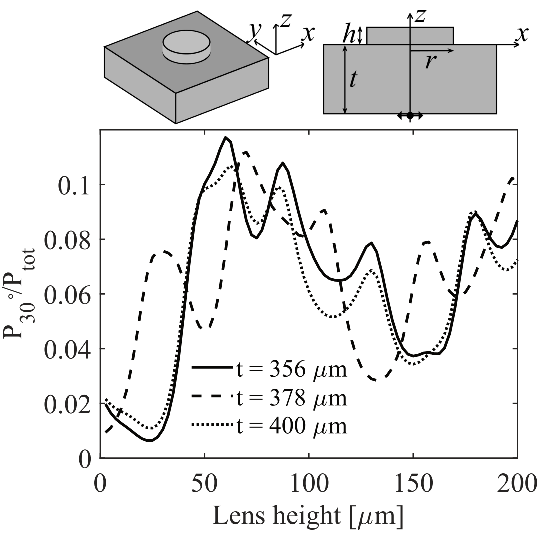

Fig. 8: The power emitted out of a substrate within an angle of 30°, relative to the total emitter power. Reproduced with permission from[71], manuscript submitted.

The geometry of lens arrays which have been fabricated is shown in fig. 9. Lenses with a diameter of 400 µm was designed to improve outcoupling at 1 THz, while lenses with a diameter of 450 µm was the choice for 0.5 THz. The target etch depth was 125 µm. A standing wave resonance inside the substrate makes this thickness critical. It was calculated that somewhere between 1 and 14% of the generated light would be coupled out, depending on the substrate thickness[71]. Time-multiplexed reactive ion etching (the Bosch process[72]) was used to fabricate the deep structures with near vertical sidewalls. Subsequent steps of etching with sulfur hexaflouride (SF_6) and passivation with octoflourocyclobutane (C_4F_8) result in vertical sidewalls.

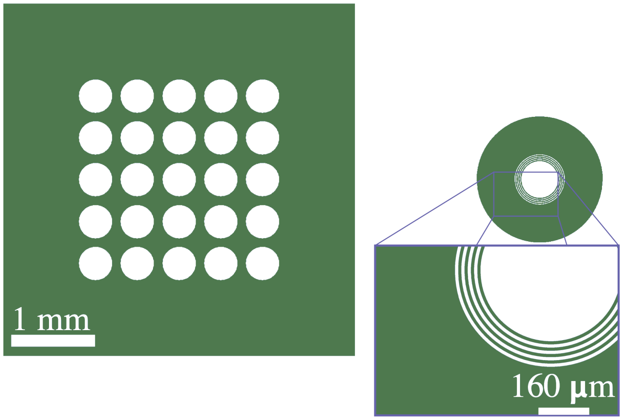

Fig. 9: The manufactured lens design etch masks. The green geometry is removed. The array has been produced with a cylinder diameter of 400 and 450 µm. The single central lens has a diameter of 440 µm, and four cycles of 10 µm ridges.

6 Fabrication of emitters

This section describes the design motivation and the fabrication of the emitter antennas characterized in this thesis. It is written close to chronological order to provide insight in the process and decisions that shaped the final design. At the end of the chapter, supporting material and relevant tertiary experiments are presented.

6.1 First light: single antennas

As the project began, some previous work had been performed by intermittent student projects. Poor reliability of interconnects had been identified as a primary problem. The antenna structure had previously been patterned in poly-methyl methacrylate (PMMA) with electron beam lithography (EBL) on 12x12 mm^2 semi-insulating (SI) GaAs. Electron beam evaporation of the chrome and gold metallization defined the antenna. The electrical contacts for the bias voltage were provided by conductive epoxy and electrical wires.

No THz light had been observed, and the reliability of electrical contact was severely limited. As the EBL process time scales with area, contact pads and feedlines were very small.

The aim of the preliminary work for the first antenna structures was to develop a reliable system for interfacing. This system had the following requirements:

- Reliable electrical contacts
- Reliability and efficiency of production
- Easy exchange of samples in the characterization setup
- Reliable interface to outcoupling lenses

To fulfill the requirements, the following strategy was chosen; 4" wafers of SI GaAs would be patterned with a feedline superstructure, using UV lithography. This would allow a comparatively thick metallization, in turn allowing wirebonding for electrical contacts from the die. The predefined superstructure features would ensure that the EBL would only be used to pattern the antennas and very short feedlines. Included in the features defined by the UV lithography step is on-die alignment markers that provide precise alignment between the feedline superstructure and the antenna connections.

Wirebonding to a thin printed circuit board (PCB) provided mechanical strength for mounting, as well as easily interfaced electric contact pads. This PCB was designed with a clearance hole that would allow optical excitation with a pump beam, as well as electrical contacts to the front side of the GaAs die. The PCB would be glued onto the frontside of the die, thus leaving the backside free and raised. This would enable a contact interface between the die and a lens. The size of the dies from the previous experiments carried into this project, permitted by the comparatively low price of the SI GaAs. Later work has die sizes of 6x12 mm^2 to allow for more devices on the same wafer.

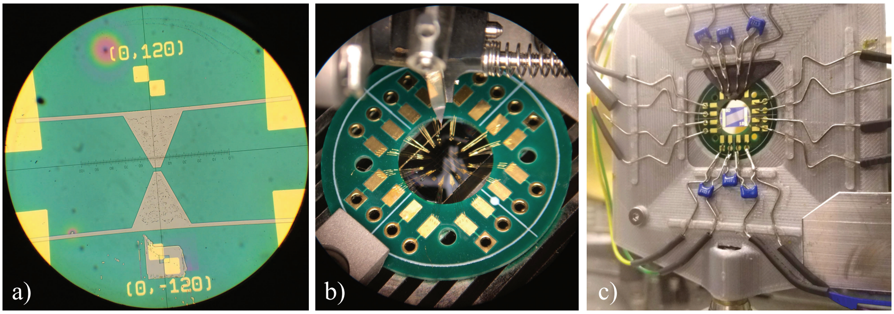

Fig. 10: a) A microphotography of the single antenna region before the antenna metallization step, but after development of the EBL resist. Note the previously defined metallic feedlines and the alignment markers. The field-of-view is 300 µm.
b) The wirebonding process, showing the green PCB and the die in the center.
c) The mounting jig. Nickel wires provide spring-loaded electrical contacts to the gold-plated PCB. Not shown: The backside includes a thorlabs SM1 tube system, that allows concentric mounting of outcoupling optics.

Figure 10 show the interface system. A patterned-but-not-yet-metallized test antenna is shown in 10 a), where the on-die alignment markers can also be seen. The developed image allows the antenna metallization to contact the coarse feedlines. Figure 10 a) show the very first antenna designs, i.e. a large bowtie structure with a gap of 10 µm. Fig. 10 b) show the wirebonding procedure, as well as the carrier PCB. The generously sized contact pads for the bias voltages also enable multiple wirebonds, further increasing the reliability of the electrical contact. Figure 10 c) show the mounting jig, where spring loaded nickel wires provide electrical contact between the bias line wires and the PCB contact pads. Outcoupling lenses may be mounted on the backside of the jig, as a Thorlabs SM1 tube is glued in place. The lockrings provide mechanical preload on a polymer spacer, in turn pushing the lens towards the backside of the die.

6.1.1 Fabrication and characterization of single antennas

The single antenna fabrication procedure is described in detail in appendix B and outlined here:

- UV lithography of coarse superstructures and alignment markers.
- Metallization of coarse superstructures, by sputter coating: 10 nm Ti, and 100 nm Au.
- EBL of antenna details.
- Metallization of fine structures, by e-beam evaporation: 2 nm Cr, and 70 nm Au.
- Glue-in to PCB carrier and wirebonding.

6.1.2 Setup for characterization

A femtosecond Ti-Sapphire laser (Spectra Physics Tsunami 3960) produces the excitation pulses. About 200 mW is delivered at the experiment input, with a pulse length of about 70 fs and a center wavelength of 800 nm. The optical system shown in fig. 11 splits the laser pulse in the beam splitter (BS), and individually attenuates and delivers 10mW to both the photoconductive emitter and detector.

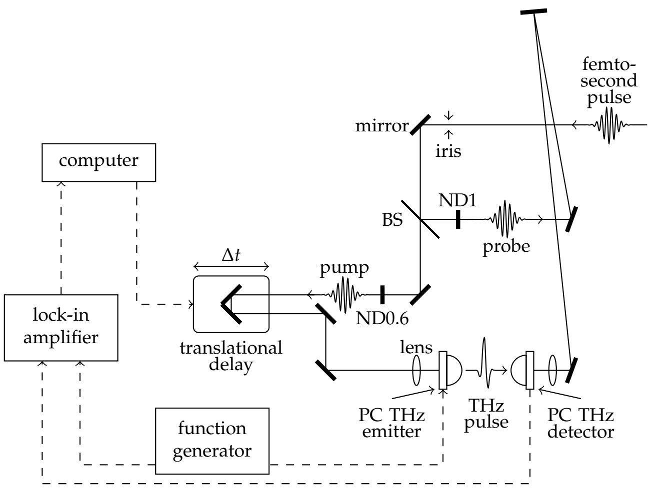

Fig. 11: Schematic representation of setup for characterization of photoconductive antenna emitters. A terahertz emitter and detector is placed 10 cm from each other, and the generated THz radiation is sampled in the detector, using the delay line. Reproduced with permission from [73]

A computer controlled the experiment, and communicated with a lock-in amplifer (Stanford Research SR530)(abbr. LIA) and a delay line stage controller via RS-232. The internal analog to digital converter (ADC) of the LIA was used to sample the output. The detector was a bowtie detector (Batop bPCA-100-05-10-800). It was coupled directly to the LIA current input (gain: $1\,\mathrm{MV\,A^{-1}}$). The LIA parameters were: 100 ms timeconstant, bandpass and line filters engaged, and the input range was set to avoid clipping.

A function generator (TTI TG330) provided the 12 kHz reference to the LIA and an AC bias voltage (bipolar sinusoid, 20 V peak-peak) for the emitter. As the pump pulse was displaced in time with reference to the probe pulse, the electric field of the terahertz emission was measured. The Fourier transform of the time-trace provided the frequency content.

6.1.3 Results of single antenna tests

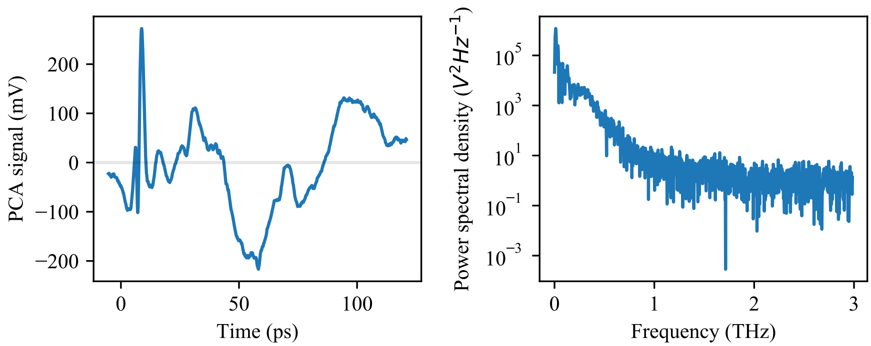

Fig. 12: The first recorded light from antennas fabricated at Aalborg university. The main THz pulse arrives at t=10 ps. The bandwidth of the emission is about 500 GHz. The origin of the large variations after the main pulse was not found.

Figure 13 show a sketch of the first generation UV lithography patterns (superstructure in metal; orange). A sketch of the antenna is shown in the nominal position.

The results of the first antennas can be seen in fig. 12. A frequency content of about 0.5 THz is visually approximated. The raw data suffers from large-scale variations in the signal after the main pulse (near t=10 ps). The origin of these large variations was never established.

Naturally, the alignment of the laser beam had a naturally large influence on the output. However, despite attempts to align to any central part of the antenna, the THz signal was observed near the edges of the antennas. By imaging the reflection from the die onto a screen, it was possible to get a rough idea of the position of the focused pump laser spot. The THz elec-

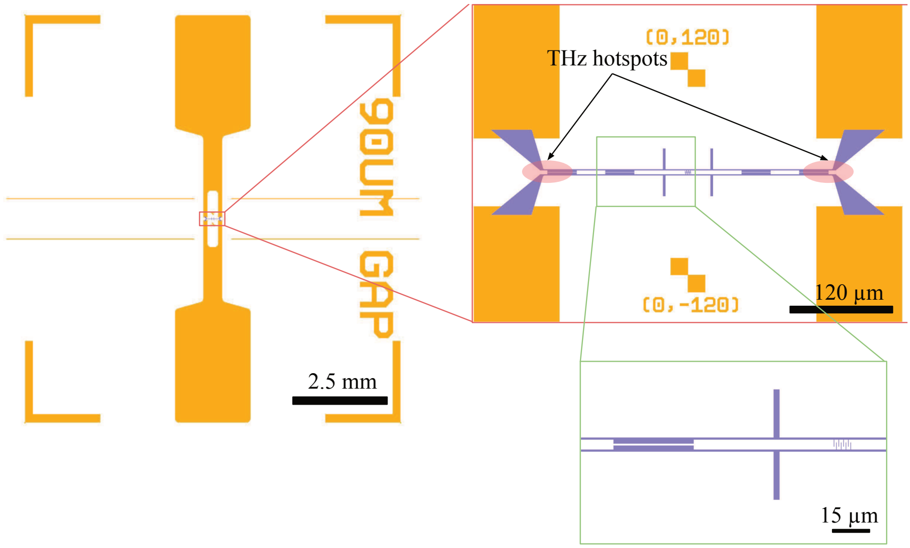

Fig. 13: The first generation antenna design. The design from[24](purple) is overlaid and contacted to a superstructure (orange) providing contact pads. Note specifically the location of the terahertz emission hot-spots.

tric field output showed hotspots, in the positions indicated in figure 13. It was hypothesized that a leak current through the substrate would severely limit the available electrical field at the designed excitation point between the dipoles. A steady state finite element model was used to verify this problem.

6.1.4 Current propagation through substrate

The result from the initial measurements indicated that the THz radiation was only produced near the lateral antenna edges. The hypothesis was that the bias voltage would drive a current that would leak between the antenna structures, and diminish the effective available electric field at the excitation center. Photogenerated charge carriers would not be accelerated, and no THz field would be generated.

During the writing of the thesis manuscript, it was discovered that a severe error was made in these simulations. The conductivity was misscaled by 8 orders of magnitude, leaving the potential issue with leakage current vastly exaggerated. The simulation suggested that a dielectric spacer was critical, and this was therefore consistently implemented in the following work.

The simulation was performed in 3D, for two configurations;

- Where the substrate is GaAs with a bulk conductivity of $1000\,\mathrm{S\,m^{-1}}$ (wrongly corresponding to a resistivity of $0.001\,\Omega\,\mathrm{m}$, and not $1 \times 10^5\,\Omega\,\mathrm{m}$ as specified by the supplier, University Wafers)
- Where a dielectric spacer is included below the feedline structure. A window is opened by etching in the antenna center (see the central square in e.g. fig. 14), but to keep the simulation simple, this was modelled as a filled region of GaAs. The antenna thus lies on top of a flat plane of dielectric, with a region of semiconductor in the antenna excitation region.

As the frequency for the bias voltage is comparatively low (few KHz), a steady state model can be used to evaluate the leak current between the antenna structures. The simulated domain is cropped to only include the antenna structure (purple solid in fig. 13), and a 10 V potential is applied to the contact pad overlap surface.

Two plots are shown; figure 14 show the surface current through the substrate (500nm below the GaAs/Metal interface). Figure 15 show the electric field in the substrate. The simulation shows that the driving bias field does not propagate to the excitation center region, and THz generation is only expected at the edges, consistent with the observation.

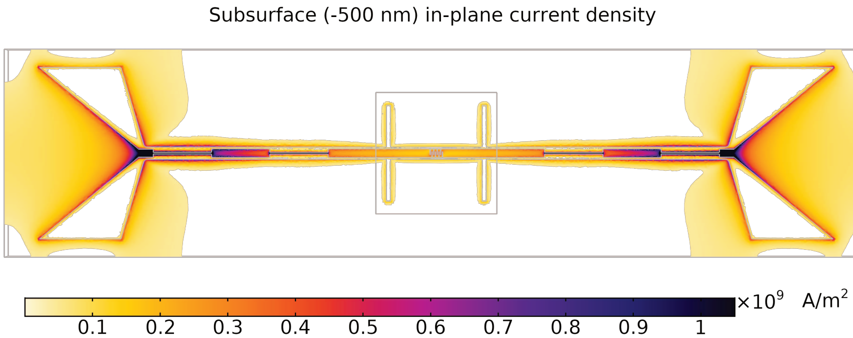

Fig. 14: Planar current 500 nm below the surface of the substrate. Note that the simulation show a significant amount of current flowing through the outside antenna geometry.

After including a SiO_2 spacer (thickness 100 nm, conductivity $1\,\mathrm{M\Omega\,m}$) between the gold structure and the GaAs substrate, it was observed that there was significantly less leakage current (see fig. 16) and sufficiently high available electric field (fig. 17) in the excitation center.

Postscript: The results of this *flawed* simulation is included to motivate the design choice of the dielectric spacer. Subsequent simulations with relevant

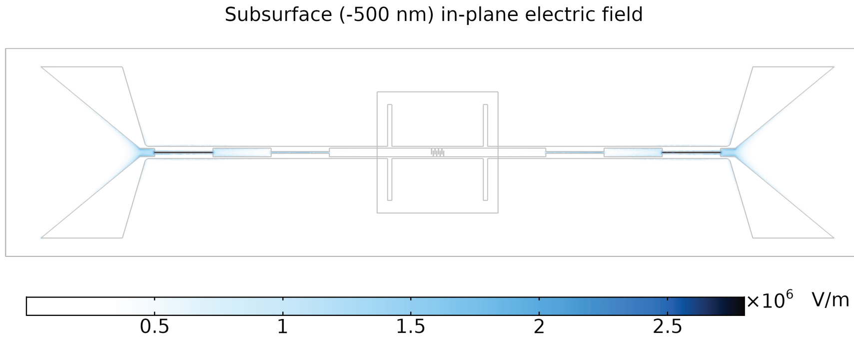

Fig. 15: Electric field in the subsurface of the GaAs substrate, without a dielectric spacer. Note that the simulation show that the dominant electric field available for driving excited charge carriers only existed on the lateral edges of the antenna.

values of GaAs conductivity indicated no challenges with leakage current in the substrate.

6.2 Testing antenna types in the rectilinear array

As a reliable interconnect system had been established, and the first THz radiation generated, the work progressed towards optimization of antenna geometry and their integration into a rectilinear array. As mentioned in the introduction, recent work has focused on carrier dynamics of the substrate, but the specific use-case for this project allowed optimization towards narrowband, resonant antenna structures. Furthermore the integration into array could in theory provide significant improvements of directivity. A design wavelength of 1 THz was used.

6.2.1 Design of array superstructure

The following requirements were identified for the array superstructure design:

- Scalability to larger arrays.
- Low resistivity feedline connections.
- Same direction of antenna bias across the array.
- Allowance for EBL alignment tolerances.
- Low crosstalk to adjacent antennas.

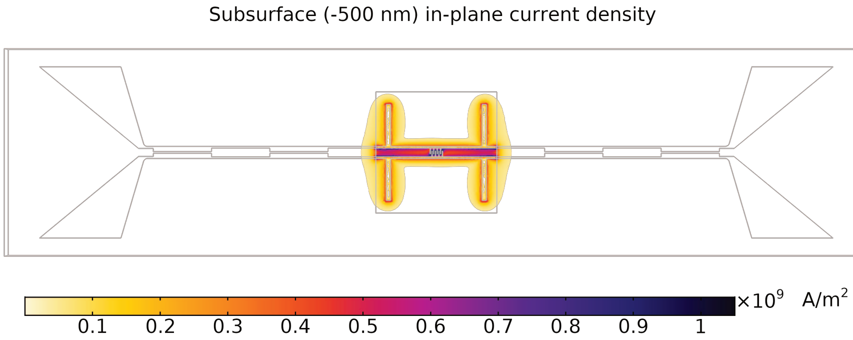

Fig. 16: Planar current below the substrate/SiO_2 spacer interface without a dielectric spacer. Note that the simulation show that the current does not leak through outside of the antenna excitation center structure. The square near the antennas is the simulated hole in the dielectric spacer.

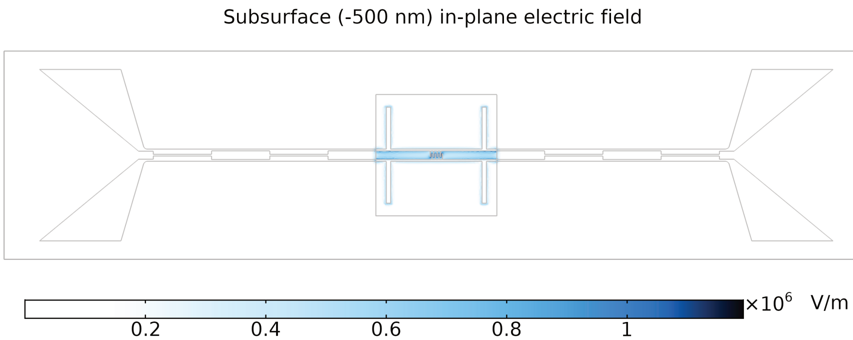

Fig. 17: The electric field in the subsurface below an added dielectric spacer is restored.

The initial mask design is shown in fig. 18. The 6 mm by 12 mm substrate size contained a 5 by 5 antenna array, to place one antenna in the center of the die. This was implemented, to allow outcoupling with conventional large diameter semiconductor lenses. The superstructure allowed for electrical characterization of single antennas, depending on the choice of contact pads. The geometry allowed an alignment tolerance of 15 µm by 15 µm with the dielectric spacer window. The wafer scale fabrication of the superstructure was comparatively fast, as only the EBL structure was bespoke for each antenna.

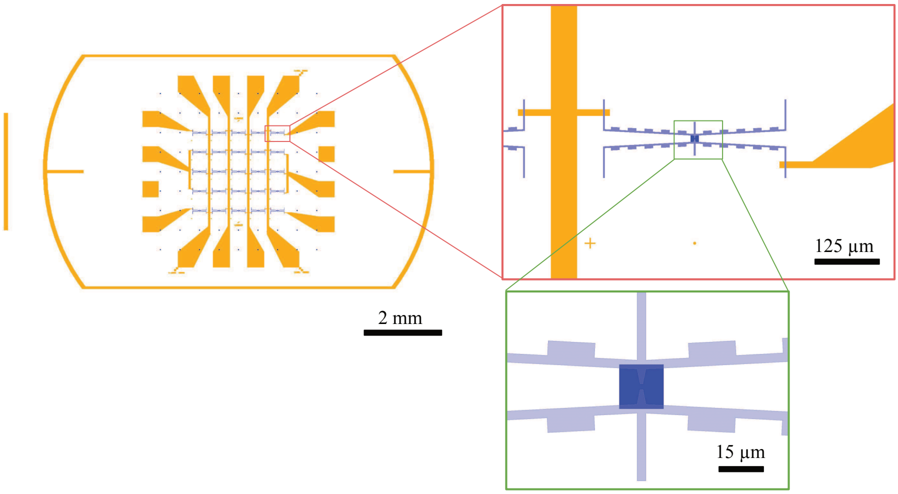

Fig. 18: Overview of the details in the initial mask design for arrayed antennas. The orange patterns in Ti/Au provides electrical feedlines from the bonding pads to the antennae. A test-design antenna is shown in purple, and the window definition in the dielectric spacer is shown in blue. Note the view outlined in red; the upper half of the antenna is always on the same polarity.

6.2.2 Antenna design

The idea presented in this subsection was published by the author in[74], along with a written description of the fabrication procedure. A selection of geometric primitives for the antenna structure were identified. The aim was to characterize antennas with various combinations of these primitives experimentally, to identify the effect from each of them. The chosen primitives were:

- Chokes
- Number of dipoles
- Single sided or double sided feedlines
- Current vs voltage excitation of dipole antennas
- Length of dipoles

The selection of designed antennas is shown in schematic in fig. 19. The reference dipole wavelength is 55 µm, corresponding to a propagating frequency of 0.8 THz in the GaAs substrate, assuming that a $\lambda/2$ mode is excited.

The reference antenna was a single dipole, double sided feedline antenna with a full dipole length of 55 µm. The dipole length was varied from 44 µm

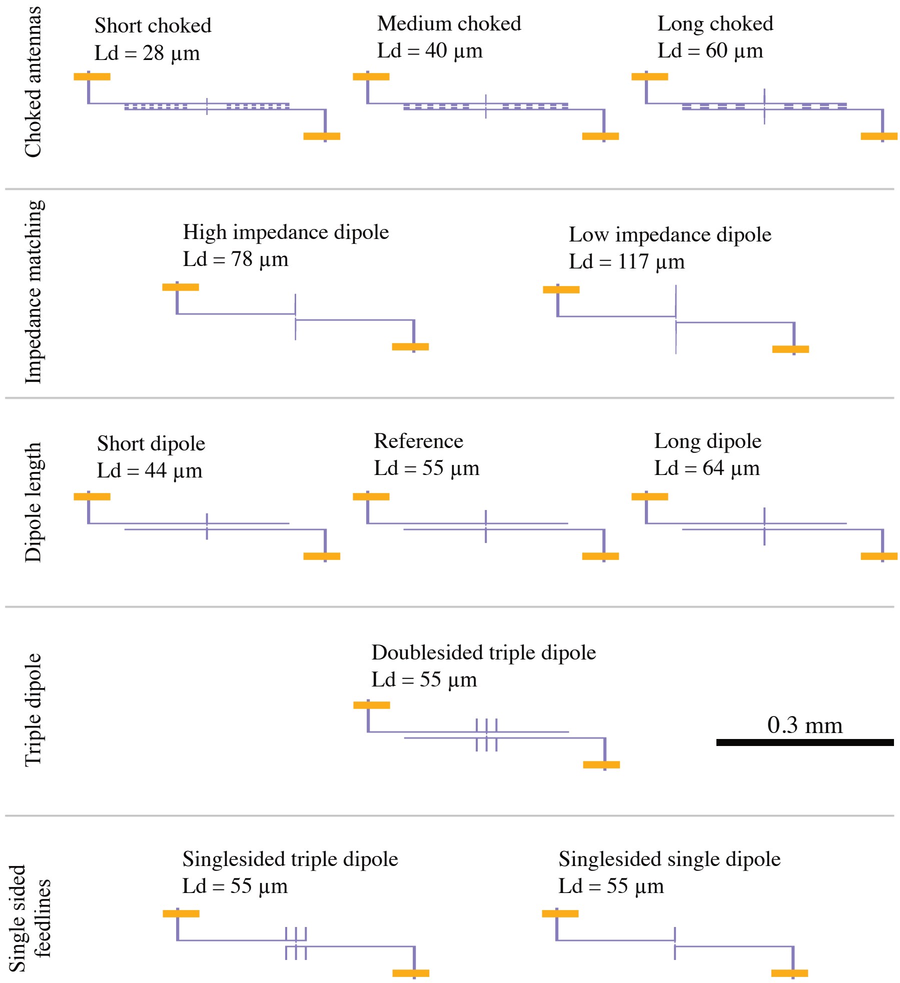

Fig. 19: The selection of photoconductive antennas that were to be characterized. Note the various combinations of dipoles, chokes and feedlines. The reference antenna is sketched in the center. The dipole length is 55 µm, and the other antennas are permutations hereof. Ld is the full dipole length, across both halves of the antenna.

to 64 µm in the short and long dipole design respectively. The number of dipoles was varied, as simulations show a better directivity for more dipoles - a feature that was previously discussed in[24]. Note that all antenna designs had the same 5 µmx5 µm antenna gap. The investigation was to characterize the exterior structure of the antennae.

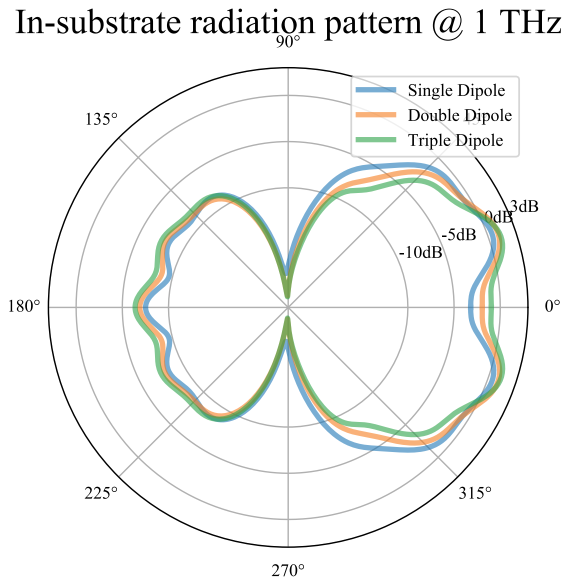

Fig. 20: The azimuthal far field emission pattern from a set of dipoles radiating into a hemisphere of GaAs. Note that the forward-emitted power and the directivity is increased the number of dipoles.

The azimuthal far field emission is calculated with COMSOL Multiphysics. An electric point-like dipole positioned 1 µm below the air/GaAs interface drove the frequency input of the antenna simulation. Due to computational economy, the antenna structure was modelled as flat perfect electric conductors in the interface plane.

Fig. 20 show that while one dipole had good coupling to the driving electric dipole, two antennas provided better directivity (also claimed in[24]). The combination of good coupling to the dipole and the double dipole's directivity was seen to combine, yielding even higher directivity.

6.2.3 Fabrication of arrayed antennas

A standard operating procedure (SOP) was defined for antenna fabrication, to enhance the comparative power of the various antennas. The SOP is found in the appendix (B), but the general fabrication procedure is outlined here. See fig. 21, for complementing sketches of the layout and fabrication procedure.

The silicon dioxide dielectric spacer (motivated in section 6.1.4) is deposited with plasma-enhanced chemical vapor deposition (PE-CVD) at a nominal thickness of 100 nm. PE-CVD was used, as the GaAs substrate does not readily provide native oxides. Secondly, alignment markers for the following masks was patterned. This was done with negative UV-lithography, and metallized with Ti/Au, before liftoff.

The windows in the isolation oxide was defined and etched using a standard buffered oxide etch (BOE etch, Sigma-Aldrich Buffered oxide etchant (BOE) 6:1 with surfactant). The windows were purposefully defined with a negative lithography step with significant resist under-cut, to motivate a window with soft edges.

The fourth step in fig. 21 shows the feedline superstructure pattern definition. The alignment of the isolation oxide windows was maintained to the same alignment markers that is used to align the superstructure. The superstructure provides contact pads and feedlines for the antennas. The robust negative resist used, allowed for 150 nm of Au, with 3 nm Ti as adhesion promoter on the oxide surface. An electron-beam sensitive positive resist stack is spun onto the fabricated wafer. It consisted of 140nm of co-polymer MMA (methyl-methacrylate) 8.5 in ethyl lactate solvent, with an added layer of C2 PMMA 950K (poly-methyl-methacrylate in 2% chlorobenzene), also at 140nm. The higher sensitivity of the copolymer gave a characteristic undercut that aided liftoff after deposition. The last wafer-scale fabrication step was manual dicing with a diamond tip and a single edge contact ruler.

Finally, the antenna was patterned onto the die with electron beam lithography (Antenna feature definition in fig. 21). To ensure liftoff, the metallization was performed in a e-beam evaporation coater with a long crucible to sample distance. 2 nm Ti was deposited as adhesion promoter followed by 70 nm Au. Lift-off was generally only reliable after 30 mins in warm acetone.

The carrier PCBs were glued onto the dies with cyano-acrylate (CA) glue, under a stereo-loupe. An alignment accuracy of about 100 μm was achieved. The circular arcs (see the superstructure sketch in fig. 18) on the exterior superstructure and the horizontal lines aided in alignment to similar structures on the PCB. 3-4 wirebonds were made between each contact pad to increase reliability.

6.2.4 Reproducibility of antenna performance

4 antennas of each design were planned, yielding a total of 44 antennas. 26 antennas were damaged during fabrication, and two antennas yielded illuminated resistances above 2 MΩ. 19 antenna sets were left for characterization. The following designs were never characterized: Short dipole, long dipole

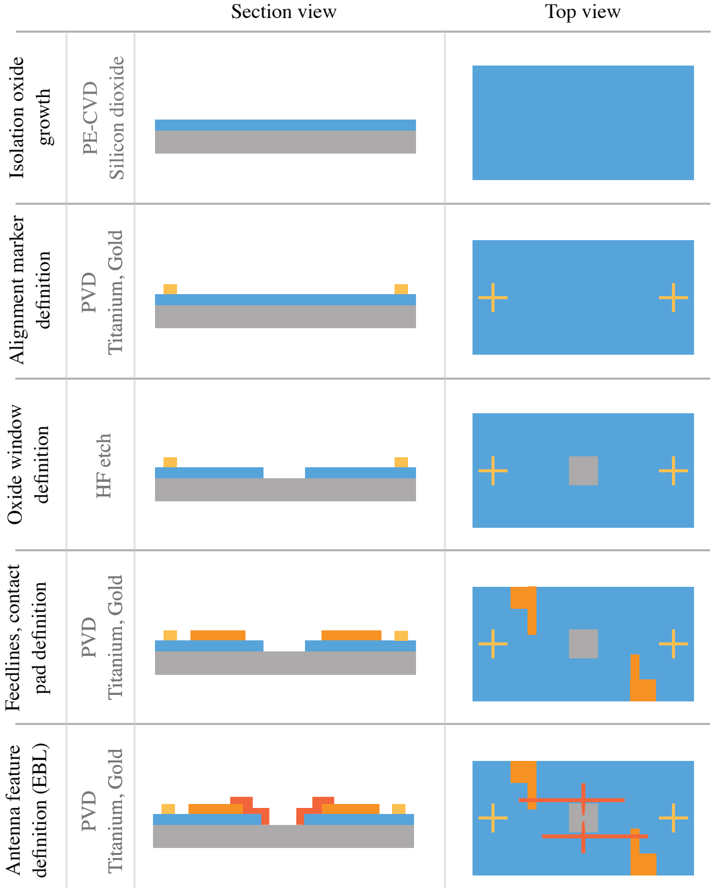

Fig. 21: Sketch of fabrication stack and definition of features. The first four steps are on wafer scale, while the EBL step was performed on each die individually.

and the singlesided triple dipole.

Characterization of the selection of designs was done in the setup shown in fig. 11, with the exception of an amplifier, to provide a sinusoidal bias voltage swing of 40 V peak-peak.

10 mW excitation power was provided and focused onto the central antenna gap with an aspheric f=15 mm lens. A collimating lens was fabricated from a stack of four 12x12 mm SI GaAs wafer samples and a Ø20 mm hemispherical Ge lens, that was used to out-couple the light from the dies. An accurate pico-ampere meter (Keithley 6485) was used to measure the antenna resistance during alignment of the excitation light. Usual values of dark resistance (R_{dark}, unlit lab-environment without windows) were hundreds of

mega-ohm, to few giga-ohm. By careful alignment, illuminated resistances (R_{illum}, 10mW of input power) could be optimized to <3 kΩ in some cases.

After alignment of the pump focusing geometry to minimize the illuminated resistance, the antenna connections were switched to the bias voltage amplifier (Linear Technology demonstration circuit DC1979A, based on the LTC6090 high voltage CMOS operational amplifier). A preliminary fast scan of the delay line was performed to acquire the pulse, and the amplitude of the pulse was optimized in a position corresponding to the rising edge near the maximum field. It was observed that RG-59 and RG-58 type coaxial cable would couple a large amount of microphonic noise into the current amplifier. A section of problematic cable was replaced with RG-316 type, and significantly less issues were seen.

Generally, a full temporal scan was acquired (maximum pulse displacement 2×90 mm) to increase the resolution. A delay stepsize of 15 µm gave a sampling frequency of 19 THz.

The comparative data analysis was performed by calculating various metrics for the antennas performance, and displaying their metric on a number of scatter plots. Conclusions and discussion would be pending the degree of clustering of the various antennas.

Two relevant terms is introduced; the intra-design variations describe the difference in performance, between the different samples, within a group of identical design. Conversely, the inter-design variations describe any differences between the different designs. Again, to conclude an influence of various antenna primitives, the inter-design scattering in the metrics would have be greater than the intra-design scattering.

The metrics that were investigated were:

Peak power: Described in dB, as the dynamic range above the noise floor. The dynamic range is defined as the signal power density, referenced to the RMS noise density of the upper half frequency span (4 THz to 8 THz). See fig. 22 for a sketch of the noise level estimation.

99% bandwidth: The bandwidth in THz, that contains 99% of the signal power. The frequency response is calculated with a Welch frequency estimator, that provides significant smoothing.

95% bandwidth: The bandwidth in THz, that contains 95% of the signal power. A simple fourier transform is applied for the domain-change.

15 dB bandwidth estimator: The bandwidth is considered the highest frequency bin with dynamic range 15 dB higher than the noise floor. 15 dB is chosen as it provides a very robust estimate.

Peak power at 1 THz: The dynamic range in the frequency span closest to 1 THz.

Peak power at 0.5 THz: Similar to above, but at 0.5 THz.

Illuminated resistance R_{illum}: Units of kΩ, measured at 5 V dc bias voltage with 10 mW laser input.

Dark resistance R_{dark}: Units of MΩ, measured at 5 V dc bias voltage in dark laboratory environment.

Resistance ratio R_{dark}/R_{illum}: Describes the potential for rate of change of current density, and thus the emitted field strength.

The python code that describe the estimators is included in appendix C.

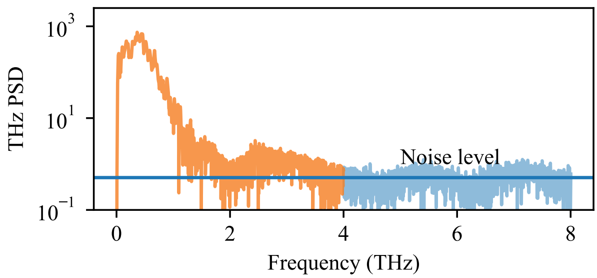

Fig. 22: Sketch of the noise floor estimation. The assumption is that the noise density is evenly distributed in all frequencies.

6.2.5 Results of antenna characterization

Large intra-design variations was observed in the data. The following section contains a variety of scatter plots, but it is illuminating to compare the best performing antenna (#74) with the second best (#66) of the same design.

Figure 23 shows antenna #74 with a relatively flat frequency response which tapers off in a monotonous behaviour. Die #66 show significant absorption in two bands around 0.5 THz and 1.2 THz. Note however that antenna #66 show a higher peak value in the time trace, corresponding to a higher peak value around 0.25 THz.

Figures 24 and 25 show the signal time traces and the signal frequency responses respectively. They are categorized by antenna types, and the figures are included to compare the raw data from the antennae. The scatter plots show various relevant correlations, with the estimated Pearsons correlation coefficient[75] ($\rho_P = 1$ describes a perfect positive linear correlation, $\rho_P = 0$ describe no correlation) and and its associated p-vale cropped to three significant digits. The data points that lie inside the red box are considered outliers.

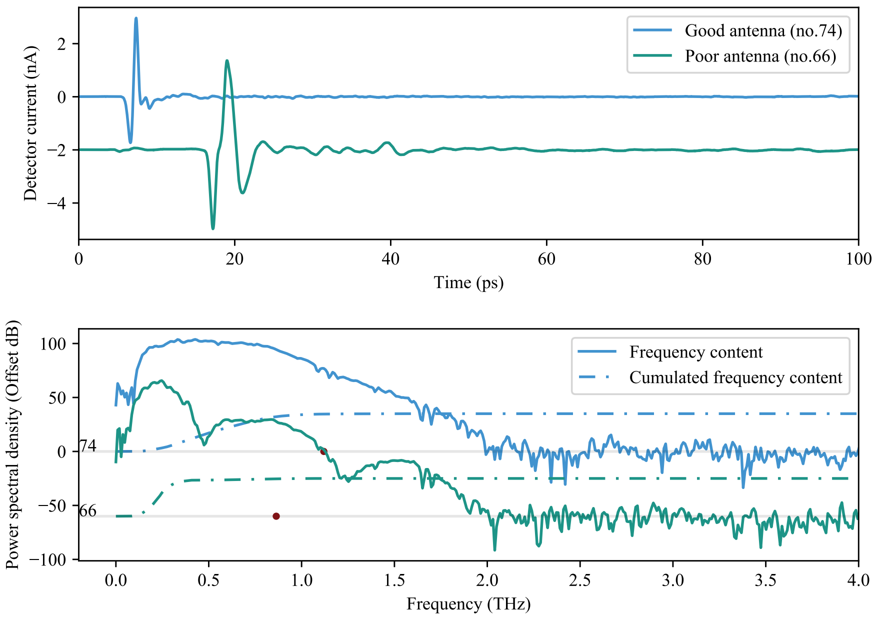

Fig. 23: The best and second best antenna of the same design (short choked). The time trace is shown in the upper pane, while the dynamic range and the cumulated power spectral density is shown in the lower pane. Note the red dot, signifying the 99% bandwidth for both plots.

6.2.6 Preliminary conclusions on antenna primitives

The figs. 26 to 29 lead to a number of conclusions. Generally, they are rather weak and the sample size is not deemed big enough to ensue a discussion in statistical terms.

- There are no clear conclusions to be made on the antenna primitives, due to the large intra-design variations in figures 26 to 29..
- The reproducibility in the time traces was poor, leading to low trust in results. The reproducibility is generally low in all other metrics, showing large intra-design variations in figures 26 to 29.
- Short antennas generally provide smoother and larger bandwidths. This can be observed in fig. 25, and it is especially noteworthy for the high-z and short choked designs.
- R_{illum} shows some prediction power on the bandwidth. This may be observed in fig. 26, with a correlation coefficient of 0.6.

- R_{dark}/R_{illum} shows very little negative prediction power to the bandwidth. A larger ratio is weakly indicative of a low bandwidth. This observation (fig. 29) is contrary to the initial hypothesis.
- The dynamic range at 1 THz has prediction power on the dynamic range at 0.5 THz. This can be observed in fig. 28, where a Pearsons correlation coefficient of 0.74 is shown.
- The bandwidth has little to no prediction power on the dynamic range. This can be observed in fig. 27.

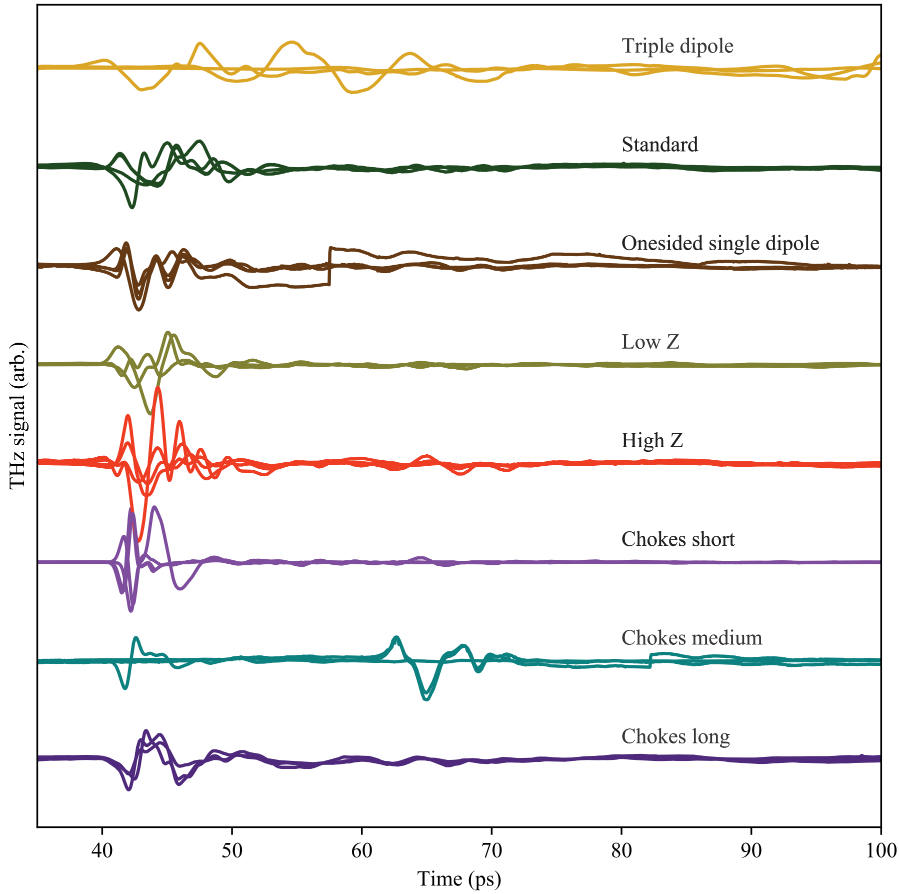

Fig. 24: All antenna time traces, segmented by antenna types. The rapid steps in e.g. the brown time trace is due to microphonic noise in a RG-59 segment of the detector cable.

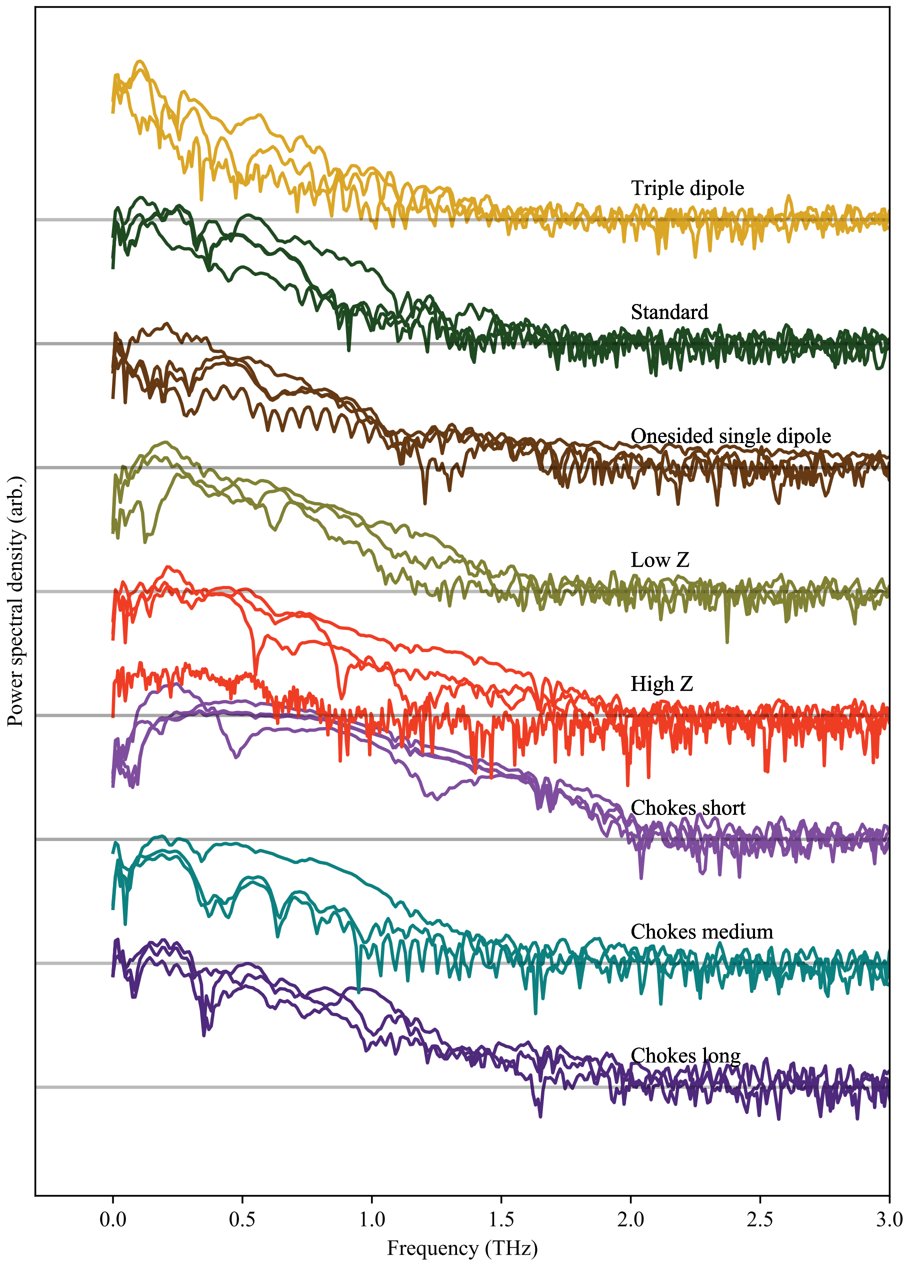

Fig. 25: All antenna frequency responses, segmented by antenna types.

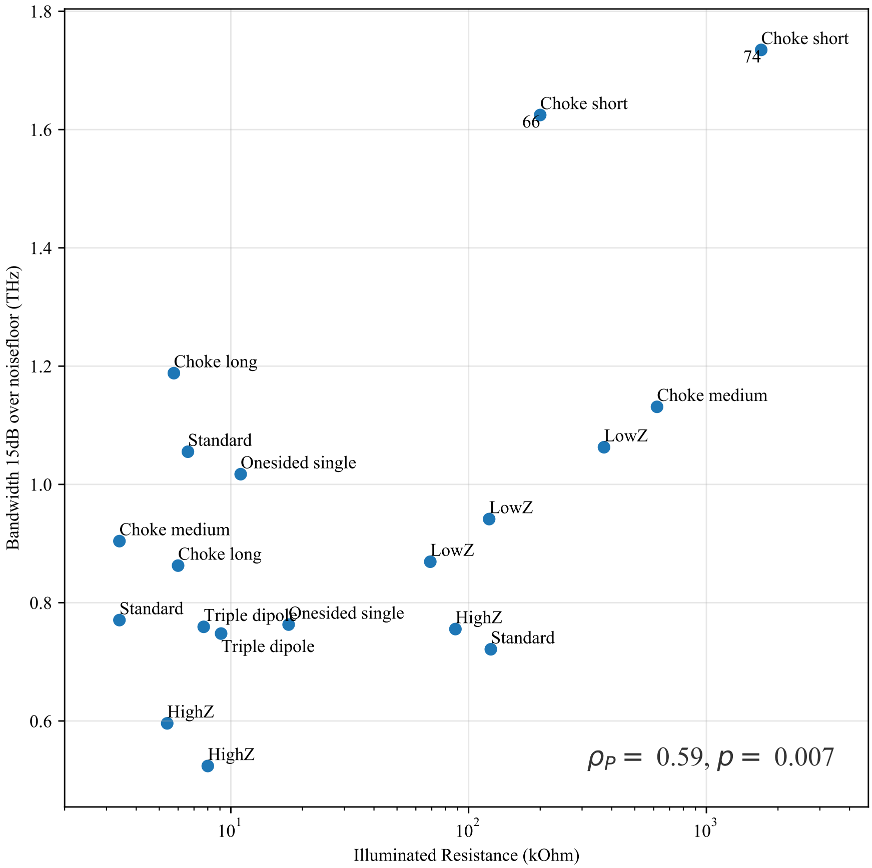

Fig. 26: Correlation between bandwidth vs illuminated resistance (R_{illum}). A positive correlation is observed.

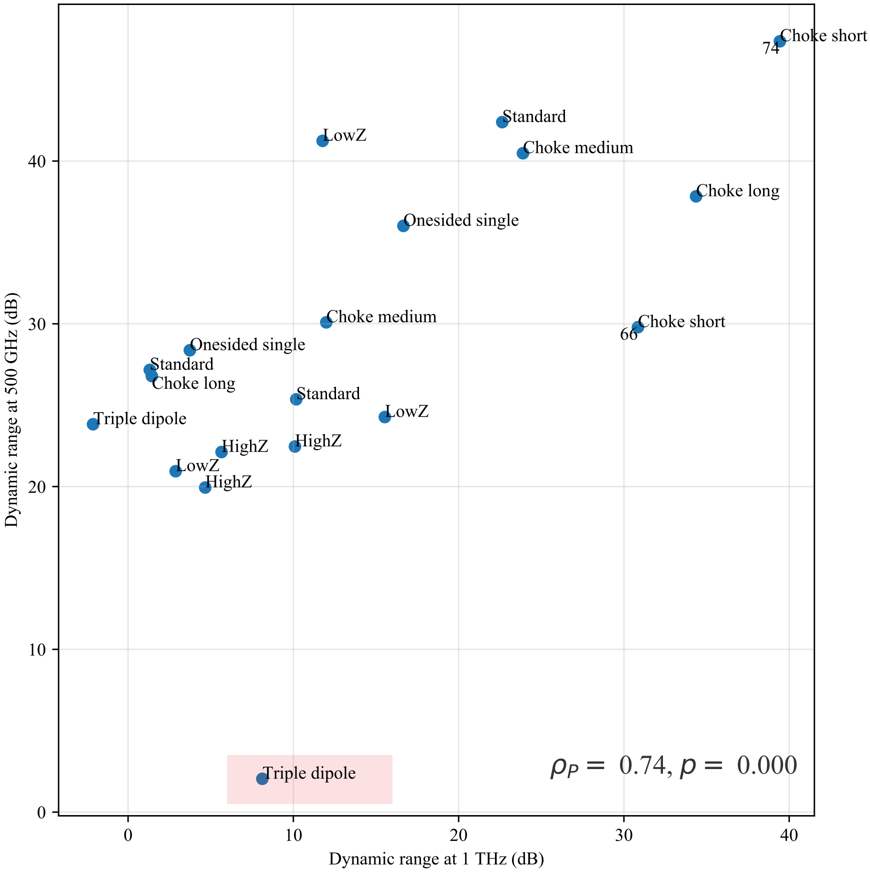

Fig. 27: Correlation between dynamic range at 0.5 THz and 1.0 THz. A positive correlation is seen. The data point in red is considered an outlier.

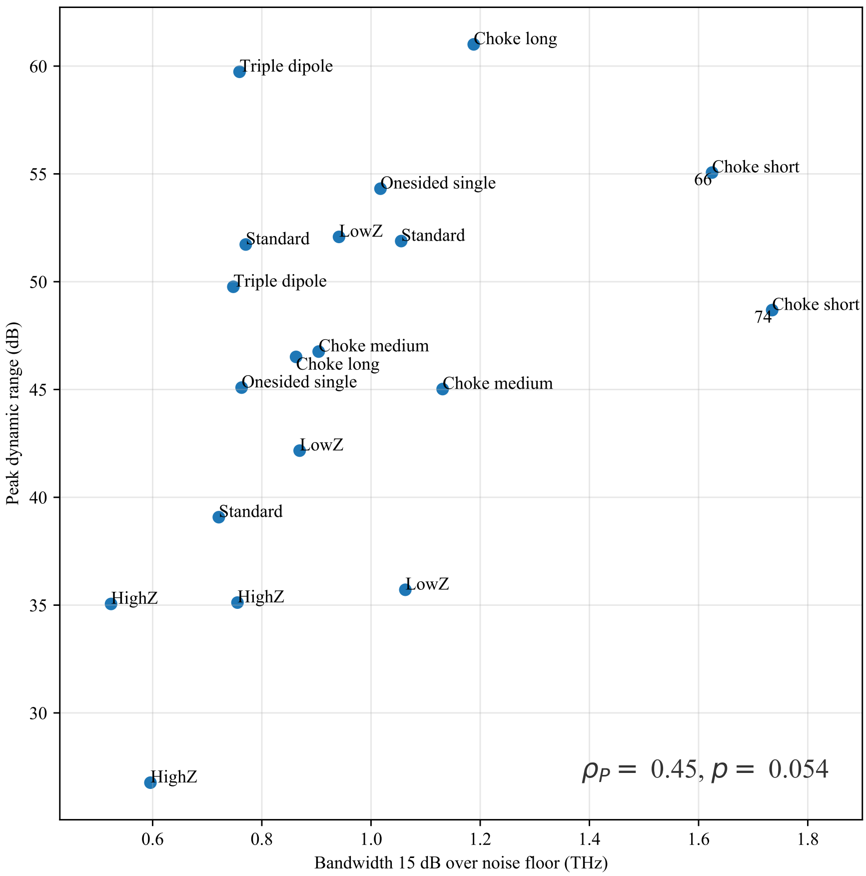

Fig. 28: Correlation between bandwidth and peak dynamic range. A weak but insignificant positive correlation is found.

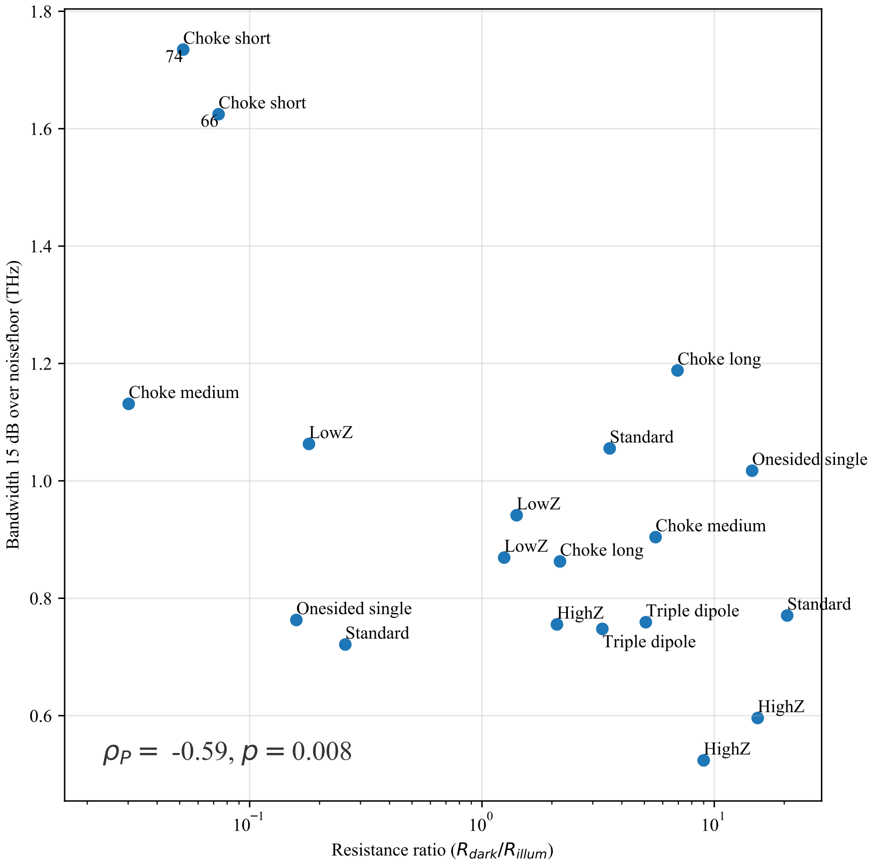

Fig. 29: Correlation between the resistance ratio (R_{dark}/R_{illum}) and the bandwidth. An indistinct negative correlation is found.

6.2.7 Improving reproducibility of antennas

As the performance metric reproducibility was unsatisfactory (intra-design scattering similar to inter-design scattering) in the previous set of antennas, two main issues with the general design and fabrication were identified in the process of the second arrayed design.

It was desireable to remove the EBL-step entirely, to allow for full wafer scale fabrication. It was also hypothesized that the end of the feedlines (see e.g. the standard design in fig. 19) would provide a very abrupt change in the feedline impedance. This would lead to reflections of a propagating copy of the THz pulse, that would re-interfere when it interacted with the dipoles. As the feedlines are very short (300 µm roundtrip), and despite that the substrate has a high weighted refractive index ($\sqrt{3.6 * 1.0} = 1.9$), the reflections would arrive within a few cycles of the THz electric field.

Two approaches are available regarding the reflection; either the design attenuates the effect of the reflection, or the feedlines are tuned to provide a resonant effect. The reflection from the open ended feedline imposes a π phase shift, so a constructive resonant effect is achieved by a roundtrip distance that is an odd number of half-integer wavelengths long ($d_{roundtrip} = N + \lambda/2$, where $N = 0, 1, 2...$). This is similar to the principle of the choked antennas.

6.3 Slanted feedline arrays

To support the most general case of use, the design strategy was aimed to attenuate the reflections from the array structure. Fundamentally, two approaches are available to attenuate reflections on impedance changes; either the impedance is changed slowly (e.g. megaphones and vivaldi horn antennas), or it is not changed at all. By increasing the length of the feedlines, the reflections would attenuate along the feedline, and arrive later.

A design was made, that provided 6 times longer distance between impedance changes. This can be seen in figure 30. By slanting the feedlines to the array, the antennas can be placed with a longer un-interrupted feedline.

Three different antennas are designed. Note that they are all larger in dimensions, to minimize the chance of interruptions in the feedlines, due to fabrication flaws. A dipole length of 140 µm is used. A single dipole, a bowtie and the triple dipole is implemented on the wafer mask. Each die contains an array of 25 antennas of the same type. The interaction area of 5 µm x 5 µm is still kept, and the same mask is used for the isolation oxide window definition.

The fabrication of the array is identical to that of the rectilinear array, shown in fig. 21. The only exception is that the entire antenna super- and fine structure is patterned in the third lithography step.

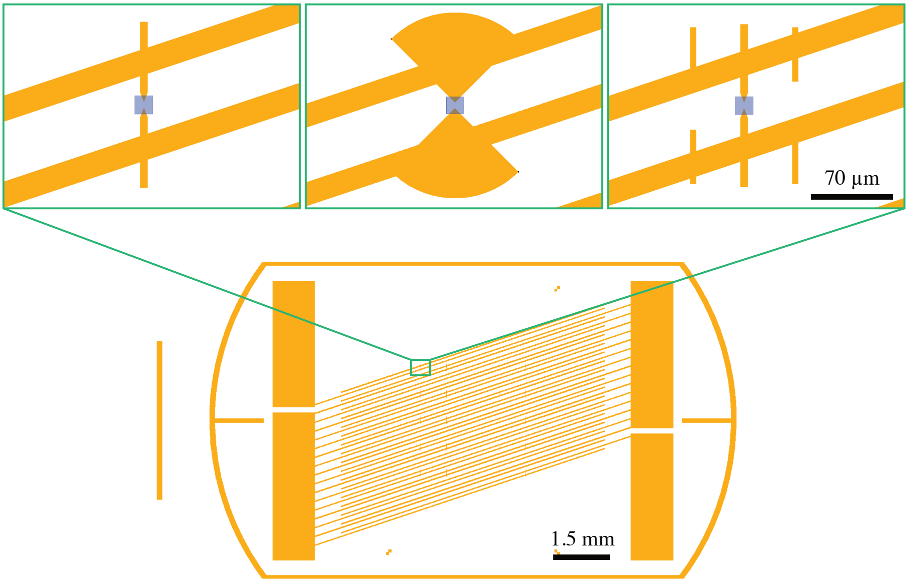

Fig. 30: An overview of the geometry of the die-scale structure of the slanted arrays. The contact pads allow for electrical contact to the single antenna in the upper left or lower right corners. Three designs are implemented on separate dies on the wafer. Shown in green outline, from left to right: The single dipole, the bowtie and the triple dipole. The dipole length is 140 µm.

6.3.1 Results and improvements

The characterization of the slanted antenna array was performed on the setup shown in fig. 11. The initial comparison is in the time traces and the frequency responses, which can be seen in fig. 31 and 32 respectively.

Furthermore, comparative scatter plots are shown, containing both the data from the rectilinear array and the data from the slanted arrays. These can be found in figures 33 to 35. The conclusions from section 6.2.6 indicate that the illuminated resistance is a relevant parameter, and this motivates the selection of scatter plot correlations.

Fig. 33 show the correlation between the resistance ratio, and the bandwidth. Fig. 34 show the correlation between peak dynamic range and bandwidth. Fig. 35 show the correlation between the illuminated resistance and the dynamic range at 1 THz. Finally, fig. 36 shows the correlation between the illuminated resistance and the bandwidth.

6.3.2 Conclusion on excitation of the slanted array

Generally, the time traces and the frequency responses show better reproducibility. Higher bandwidth is generally observed, along with a smaller scattering of the illuminated resistances.

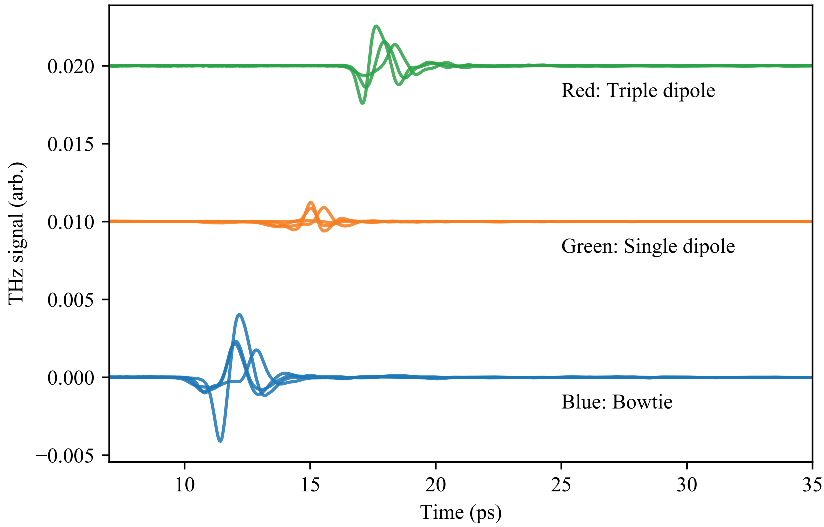

Fig. 31: The time traces for the three designs. The single dipole antenna shows generally lower amplitudes.

- Crucially, the new fabrication procedure is slightly more reproducible than the previous.
- The experiment is not optimally designed, in that it does not directly indicate whether it is the fabrication procedure or the antenna geometry, but the previous conclusion can be induced.
- Large variations in design (from the rectilinear array to the slanted array) has not provided clearly different responses in antennas. This indicates that the meso-scale antenna structure is not very critical at the frequency range of 0 THz to 2 THz.
- Significant clustering is seen in fig. 34, separating the single dipole antennas from the bowtie and triple dipole design.
- Figure 36 show significantly poorer correlation between the illuminated resistance and the bandwidth.
- The dipole lengths were significantly longer than previous antennas.

This concludes the work on the antenna geometry optimization. Up until now, only the central emitter has been characterized. Further work follows, aiming to excite the entire 5 by 5 array of photoconductive antennas.

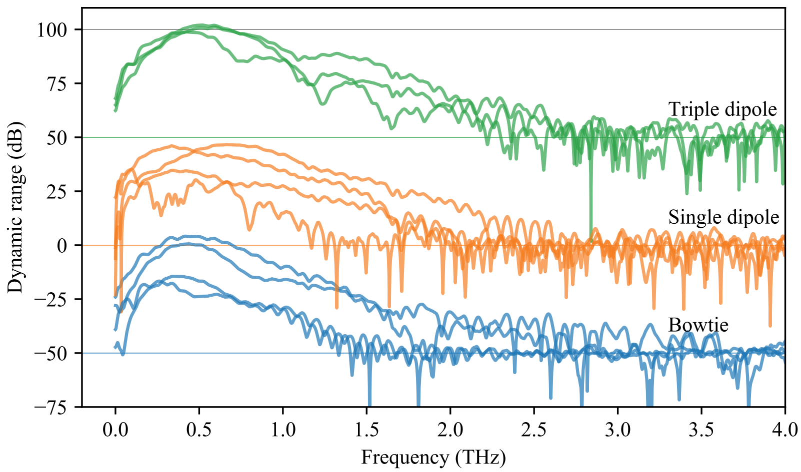

Fig. 32: The frequency responses of the three antenna designs. The y-scale has an offset of 50dB. The generally lower amplitudes for the single dipole is reflected in the response.

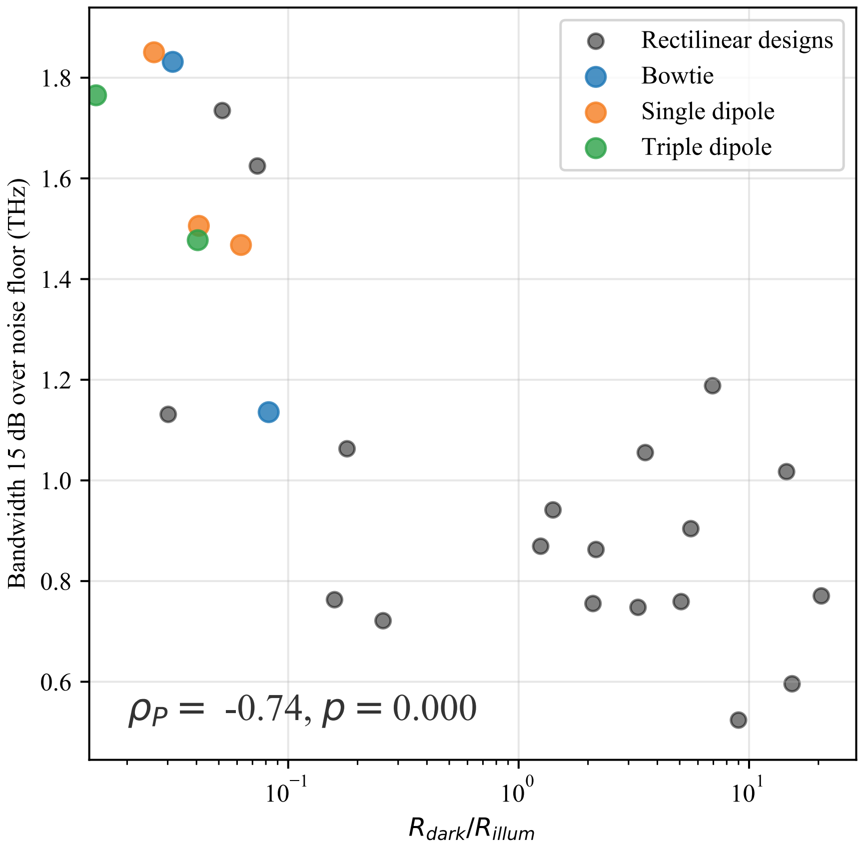

Fig. 33: The correlation between the resistance ratio and the bandwidth improves with the addition of the new data. Note the significant smaller scattering for the resistance ratio.

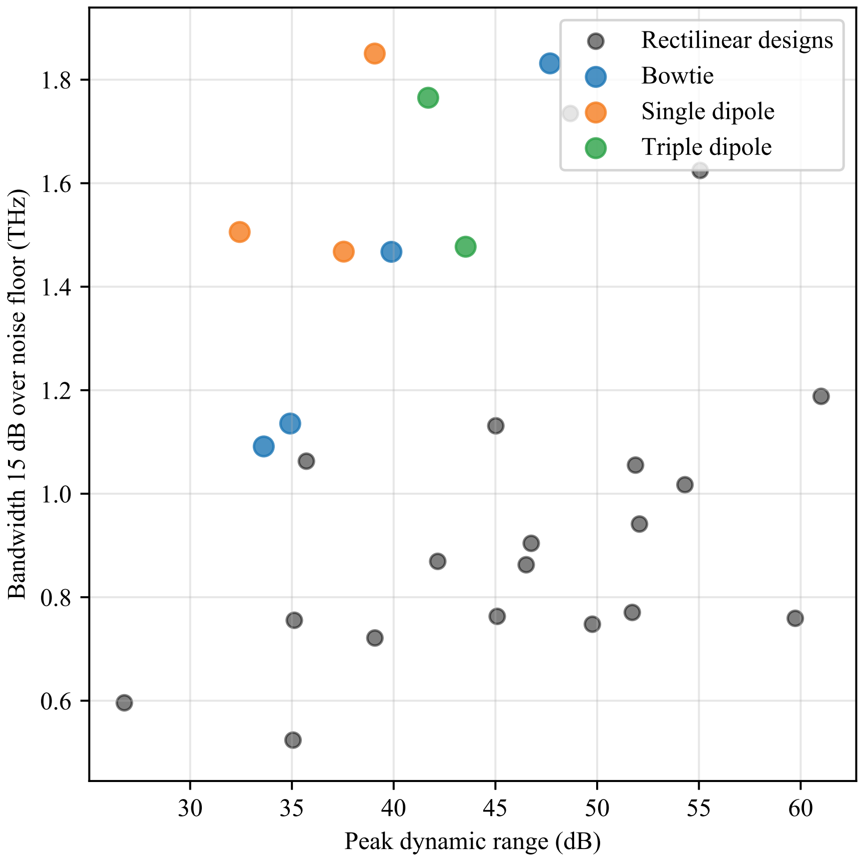

Fig. 34: Significantly improved bandwidth is observed for the new antenna design. The dynamic range is not improved.

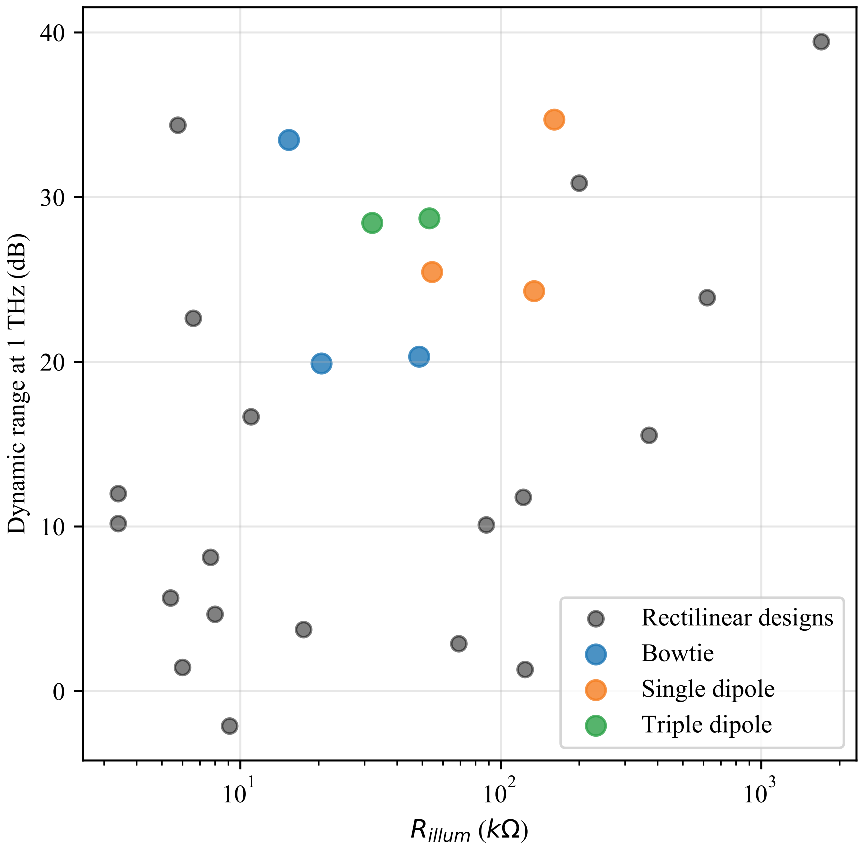

Fig. 35: The new devices show generally better performance at 1 THz. The clustering is slightly more pronounced with respect to the illuminated resistance.

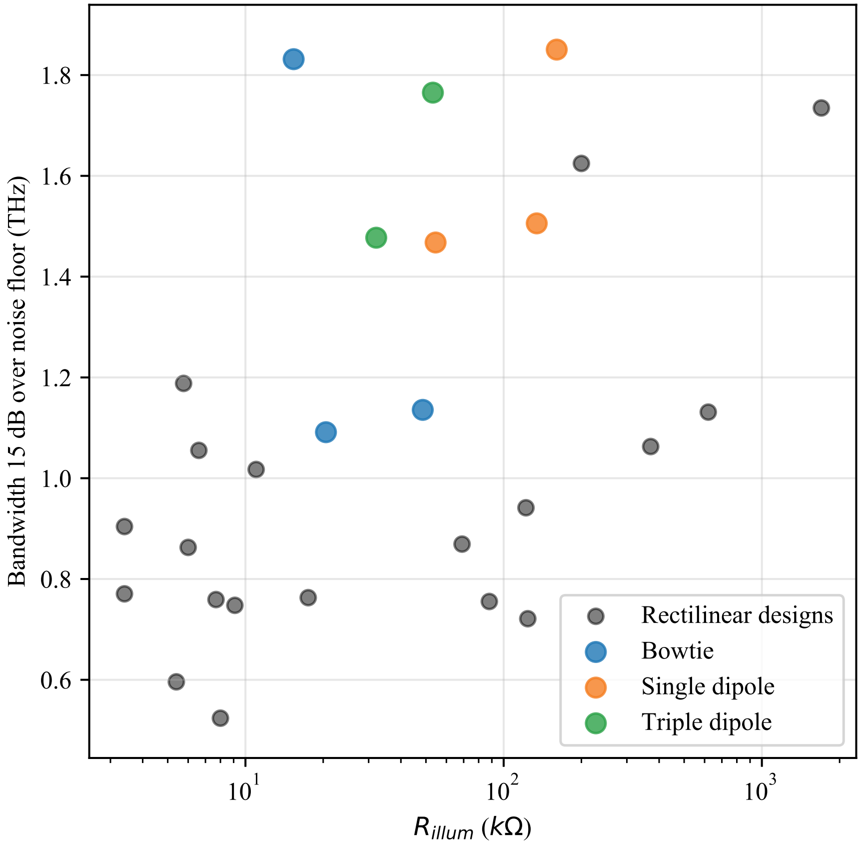

Fig. 36: The new data does not improve the weak correlation from figure 26

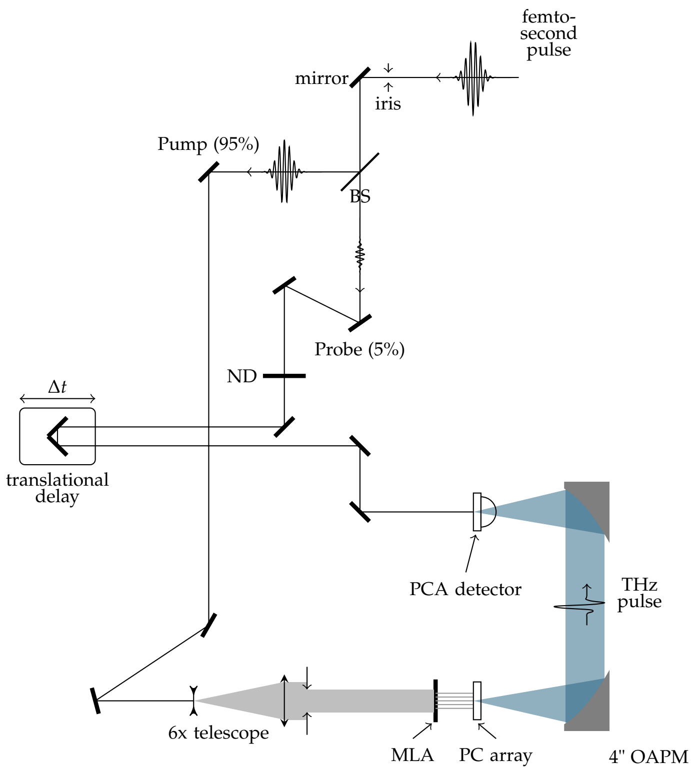

Fig. 37: The setup for excitation of the entire emitter array. The changes from fig. 11 include significant changes to the excitation focusing geometry, and the general delivery beampath. Furthermore, an un-attenuated beam is coupled in from the Tsunami, delivering 1 W at the experiment entrance aperture. Note that the PCA detector includes an aspheric lens for diffraction-limited focusing of the probe beam onto the gap of the PCA detector.

6.4 Excitation of entire slanted antenna array

The exciting pump pulse is provided via a microlens array (abbreviated MLA, Edmund optics #64-479), that focuses a collimated light source onto a rectangular grid of points. It has an effective focal length of 13.8 mm, and a pitch of 500 µm with a fill factor near unity, resulting in very little loss. The pitch of the MLA has driven the pitch of the designed antenna arrays.

By alignment of the micro lens array in the lateral dimensions along the beam, and ensuring correct rotation around the beam axis, the array of focal spots is aligned on the array of photoactive sites. The setup can be seen in fig. 37.

6.4.1 Distribution of pump power on array

To achiece a predictable output from the array, it should be assumed that the individual antennas are illuminated evenly. Knife-edge measurements of the output beam from the fs oscillator showed a beam profile which is wider in the vertical direction (see fig. 38), but with full width half maxima (FWHM) of 1.3 mm and 2.2 mm.

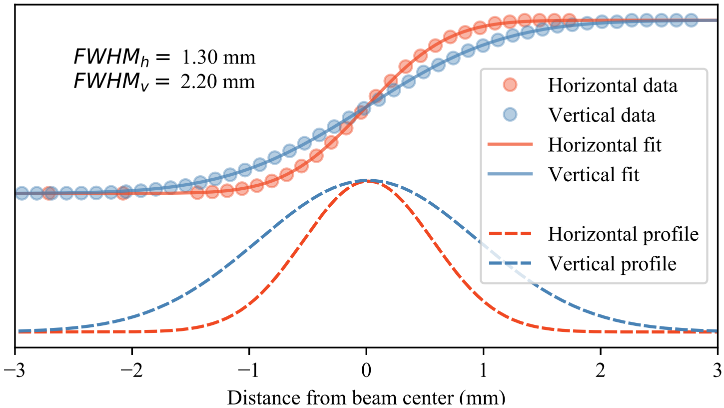

Fig. 38: Results of the knife-edge measurements of the fs laser output near the beginning of the telescope in fig. 37. The power as a function of knife edge position is fitted to a gaussian cumulative distribution to provide the FWHM in the vertical and horizontal direction.

Taking the measured beam profile into account, and assuming a MLA fill factor of 1, the power delivered per site can be calculated. Figure 39 a) show the optimal distribution of power on the MLA sites. Figure 39 b) show the delivered power in % of the total input power, per antenna excitation site.

The simulation shows that a power variation of 75% would be seen from the central emitter to the corner emitters. The delivered power to the telescope was 645 mW, so the pump light would deposit 34 mW on the central emitter and 8.4 mW on the corner.

To minimize the difference in deposited power between the corner and the central emitter, the beam was to be expanded using a telescope. The decision on the beam magnification factor was based on results in fig. 40, where the variation from corner to central element, and their powers in percent, was shown as a function of beam expansion. With an input power of 645 mW, 1.5% would correspond to 10 mW, and higher power would require attenuation with ND filters.

Figure 40 showed a threshold of 20% difference between the corner and central emitter would be achieved at an expansion of 6 times. 10% difference would require a 13 times expansion.

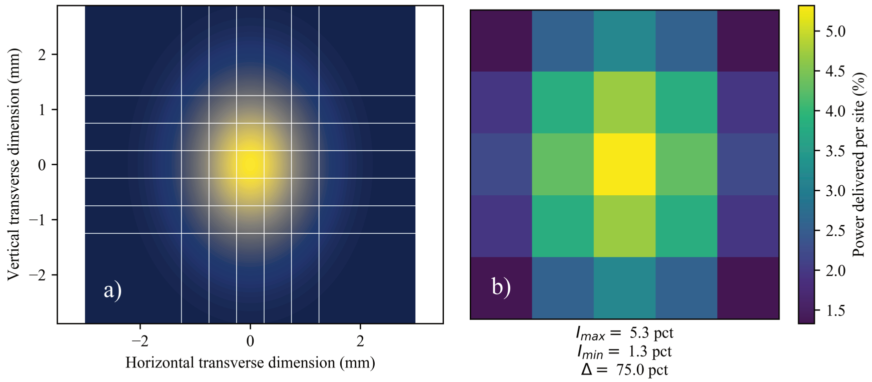

Fig. 39: a) show the distribution of laser power into the MLA. b) show the power delivered per site in % of the total input beam power. Note the large variation between the center and the corner site.

At a 6 times expansion of the probe beam, similar integrations was performed: In units of deposited power per site, the central site would receive 6.1 mW, while the corner emitter receives 4.9 mW. The expanded laser light distribution may be seen in fig. 41 a), while the integrated power per site is seen in fig. 41 b).

It was concluded that 20.6% was a functional tradeoff to the power - if the beam was expanded any further, even less pump power would be available per emitter site. The telescope was set up as a Galilean telescope due to the limited space in the setup. A plano-concave lens with a focal length of −25 mm diverged the beam, while a plano-convex lens with a focal length of 150 mm collimated the beam.

As the power per device would be lower than the reference 10 mW, there was a motivation to characterize the power scaling of the emitters. The dependency of the peak-peak current from the input power to a single emitter is measured. The data is acquired in the setup shown in fig. 37, except that the telescope is removed and a single aspheric lens is used instead of the MLA. No outcoupling lens is used. Only one device has been characterized, the triple dipole TD21. The results indicate a saturation at higher optical power than 10 mW. Fig. 42 shows the time traces and the power scaling in terms of peak-peak current.

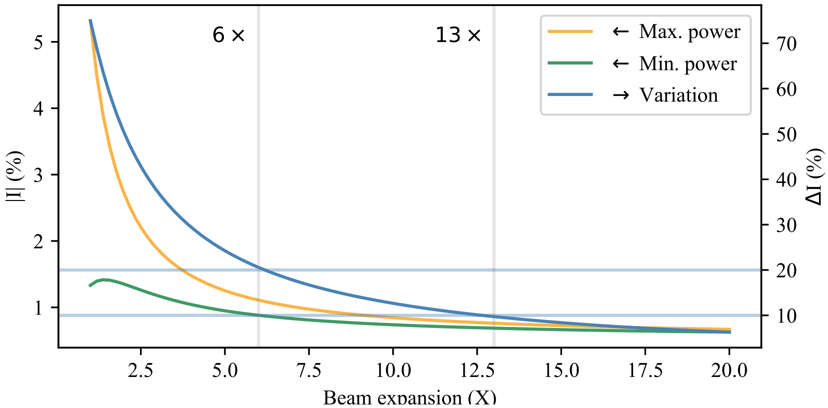

Fig. 40: The tradeoff in the beam expansion decision. The left vertical scale (green and yellow lines) show the minimum and maximum absolute power per site in percent of the input power. The right vertical scale (blue line) show the variation from the central to the corner emitter in percent of delivered power.

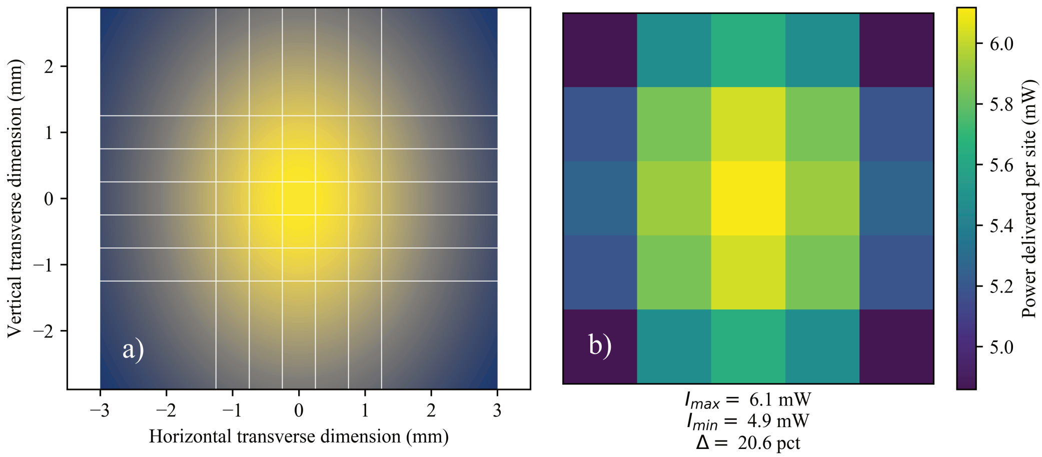

Fig. 41: a) show the expanded beam onto the simulated MLA (white lines). b) show the power delivered per site, assuming an input to the telescope of 645 mW.

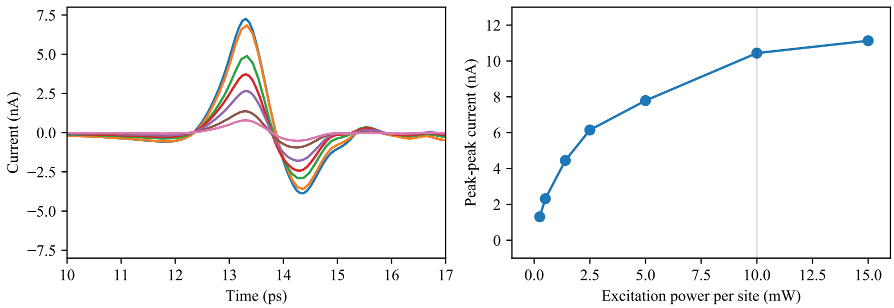

Fig. 42: Left: The main pulse, for a optical excitation powers between 0.25 mW to 15 mW. Right: The peak-peak current as a function of input power, proportional to the electric field.

6.4.2 Results with PCA detection

Arrayed antennas should scale the forward emitted intensity with the number of active emitters. However, when comparing the measured THz signal when exciting a single central emitter with 10 mW, and the array with a total pump power of 125 mW delivered to the 25 antennas, only a very small difference is seen. Figure 43 show the time traces and the power spectral density of the signals. As the data is acquired without an outcoupling lens, reflections corresponding to the roundtrip time in the substrate were visible. These were cropped with a gaussian window function, centered on the main pulse.

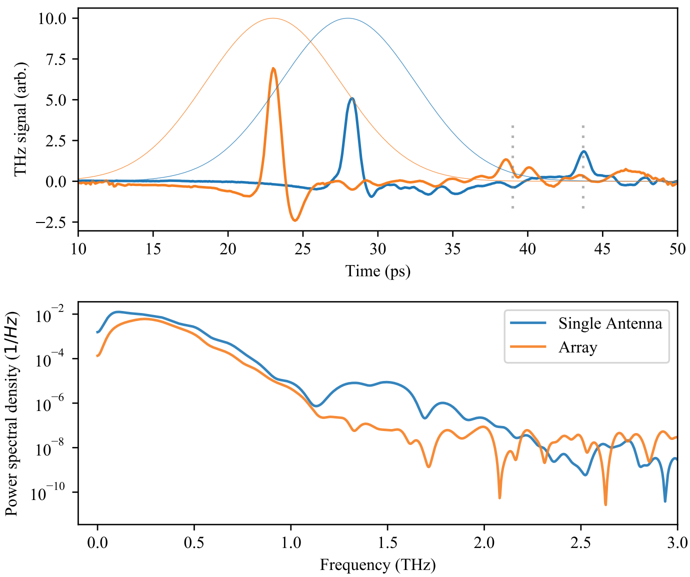

Fig. 43: The acquired signal from the bowtie #14 sample. The blue traces are for the single antenna, and the orange traces is for the array. The data indicates that no gain in power or bandwidth is achieved by exciting the array. A slightly higher signal is seen for the array in the time trace, but this does not carry into the frequency response. The reflections inside the substrate can be seen by the vertical grey dashed lines. A gaussian window function is used to crop the reflections.

The antennas were only provided with 5-6 mW, and while this contributes to the lower intensity measured from the array, further explanations must be made. It should be noted that the long feedlines with up to 3 antennas in the slanted array may provide a too high impedance for the necessary restorative current.

Another contributing factor is the large extent of the emitter: As the emitter radiate from a pattern of point sources with a pitch of 500 µm, the image on the PCA detector will have a similar pattern. The extent of the image of the source is sketched simplistically in fig. 44, where it is shown how an off-center emitter is focused onto the detector outside of the interaction region of the PCA detector. The PCA detector in the detection setup was attached to a spherical lens for in-coupling, but the issue remains.

The interaction region is limited by the smallest spot size - defined by the focusing geometry of the input probe beam. An aspheric lens (Thorlabs A260TM-B) is used, effectively providing a diffraction limited spot size. Thus a larger area detector could be a solution to the scaling problem.

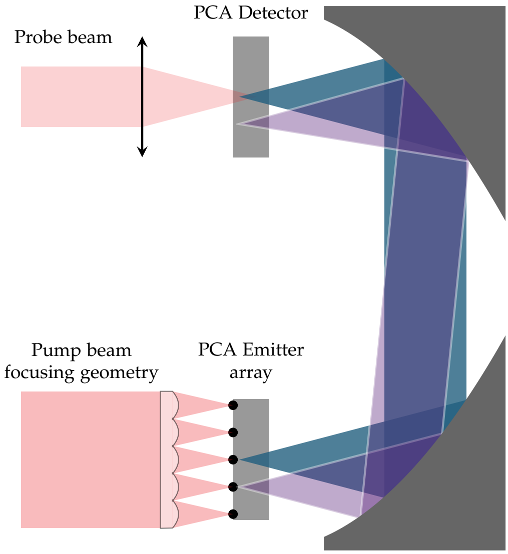

Fig. 44: Sketch of the OAPM imaging into the detector. The PCA detector is poorly suited to measurements of extended sources like the 2.5 mm by 2.5 mm emitter array. The figure shows a very simplified view of the geometry - the coupling lens for the detector is not shown.

6.4.3 Results with electro-optic detection

Electro-optic detection has been tried, to provide a detection volume that is bigger than the focus spot size on the PCA. The polarization of a collimated probe beam is rotated slightly by birefringence induced by the THz field. The rotation of polarization is measured using a quarter waveplate (QWP), a Wollaston prism and a balanced photodiode amplifier. The setup is shown in fig. 45, and a 1 mm thick ZnTe crystal from Eksma optics was used. The probe beam passes through a small hole in the off-axis mirror. The pump focusing geometry is similar to previously explained.

The balanced photodiodes is amplified immediately in a lab-built circuit, presented in appendix D. Bipolar voltage excitation of the emitter antenna was used, at 40 V peak-peak.

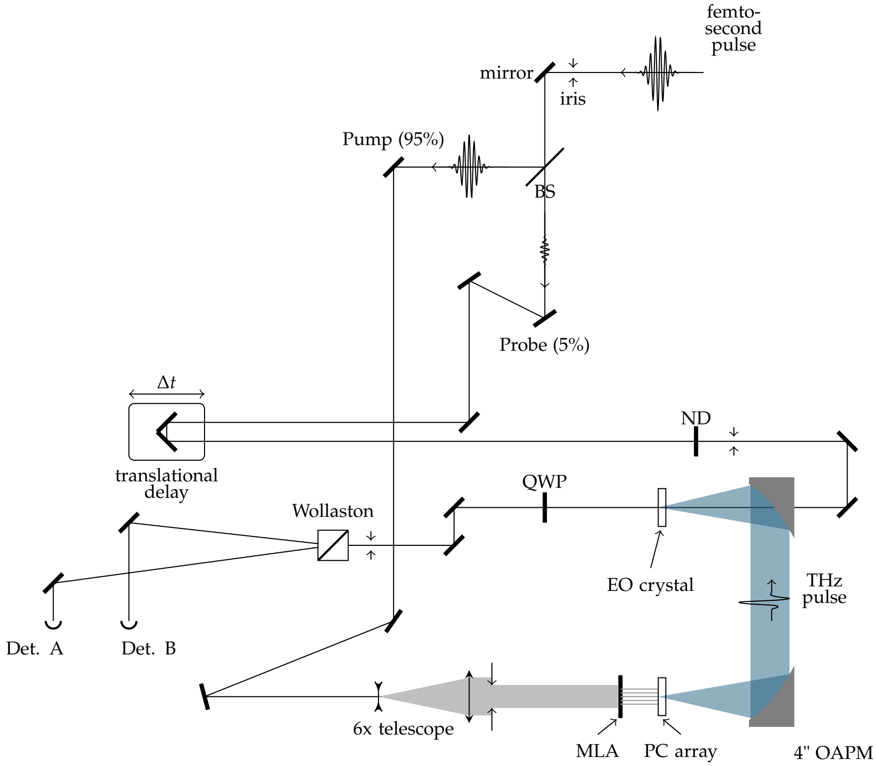

Fig. 45: The setup for electro-optic detection of the antenna output. The probe beam is passed through a 4 mm hole in the OAPM. The THz-induced birefringence changes the polarization of the probe beam, and this is measured with the balanced detection setup, consisting of the quarter wave plate (QWP), the Wollaston prism and the balanced photodiodes. The difference signal (Det. A - Det. B) is amplified and fed to the LIA.

The signal was very minute and would not be optimized further. The output of the emitters was not large enough to provide a signal from a single emitter for reference. Figure 46 show the time trace and the frequency content of both the raw signal from a bow-tie array, as well as the signal with a gaussian window function.

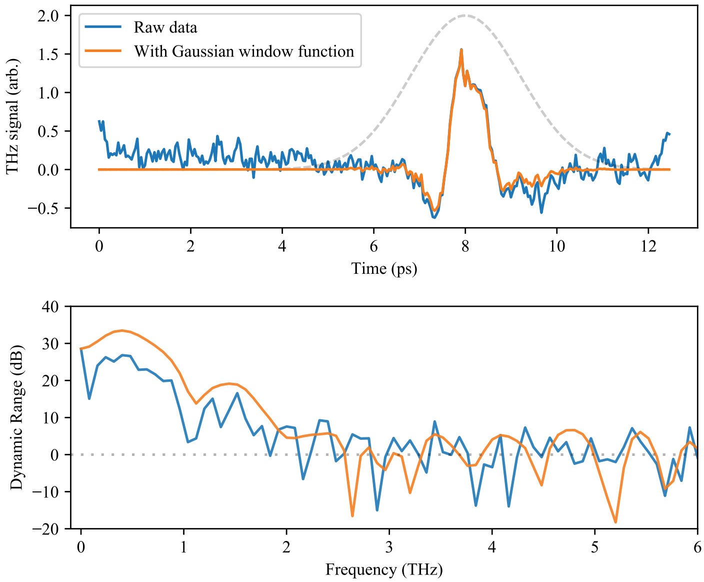

Fig. 46: The results from the electro-optic detection of the output, with the setup shown in fig. 45. The blue line describe the raw data from the #14 bowtie array, and the orange line is with the Gaussian window function applied. An estimated bandwidth of 2 THz is seen. The increased dynamic range in the orange line is due to suppression of noise by the gaussian window function.

6.5 Substrate lens performance

This section describes the instrumentation, measurements, analysis and results for the characterization of the optimized lens designs in combination with the slanted feedline antenna array.

To characterize the lenses, some instrumentation was necessary. The lens arrays and the antenna substrate must be ground down to a total thickness of 500 µm, per the design specifications. Furthermore, due to a resonance in the combined substrate, the tolerance for the thickness is set to a be within 1/5th of a wavelength from the optimum; 482 µm to 518 µm. The abrasive process must be designed to allow for a perpendicular change in substrate thickness.

Furthermore, the lens and antenna arrays must be aligned in front of each other, with their respective polished surface in contact. This requires a jig that will absorb small errors in alignment, without applying significant mechanical stress to either substrate.

Finally, a method to align the lens and antenna arrays must be developed. A double camera setup has been developed along with a software tool to overlay the image of two viewports in one image, and providing a live feedback of the alignment.

6.5.1 Single substrate grinding

To grind the Si lenses and the GaAs antenna substrates to the specified thickness, a concentric grinding jig was designed. The substrate to be ground was mounted on the end of a stainless steel cylinder (Ø20 mm / 70 mm). This cylinder will be referred to as the grinding core. The core had a precise sliding fit in a larger block (Ø 60 mm / L 60 mm), also made from stainless steel. Several Ø 13 mm holes were drilled in a circumference outside of the central bore, to decrease the mass of the grinding jig. Note that due to the precise fit between the core and the jig, a ventilation hole was drilled at the bottom of the jig, to allow free longitudinal and rotational movement of the core inside the jig.

Struers silicon carbide (SiC) grinding foil was clamped to a ground cast iron flat plane, to ensure flatness. WD-40 was used as grinding lubricant and to keep the swarf in suspension.

To monitor the grind progression, a measuring mount was fabricated. This measured the length of the grinding core plus the substrate thickness, using a linear variable differential transformer gauge (LVDT) that provided an accurate readout of a linear probe. The read out instrument was the TESATRONIC TTA 20 analog meter. The instruments lowest range was a full-scale measurement of 6 µm. The reading resolution and accuracy can extended to a few nanometers, by reading the analog voltage from the meter, on a 6-digit voltmeter.

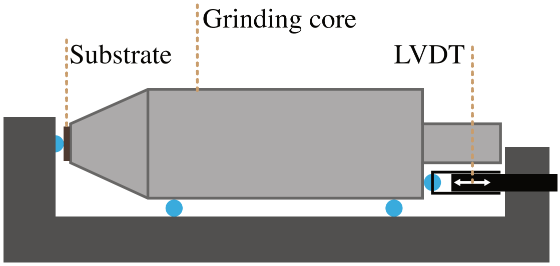

Fig. 47: Sketch of the measurement jig. The total length of substrate, wax and grinding core was measured in the frame.

Figure 47 show a sketch of the measurement mount. As the substrate was ground towards the goal thickness, it could be removed from the grinding jig and placed in the measurement mount. Four hardened steel balls provided the positional alignment (only 2 is shown in fig 47). One hardened ball contacted the substrate in a point and provided mechanical adjustment to zero the indicator coarsely.

Grinding the silicon was started at grit #320. This was a tradeoff between material removal rate and corner stress. Lower grits would provide faster grinding, but the edges had a tendency to chip, catch and break the substrate. 320 µm was to be removed, as the wafer started at 520 µm. 200 µm was ground off in the first iteration, and the core was moved to the LVDT readout mount. The change in thickness was noted and the meter was nulled again. Secondly, 100 µm was ground off, and the abrasive paper was changed to #800 grit. The remaining 20 µm was removed, and the substrate was removed with hot air, releasing the wax. The substrates were sonicated with acetone to remove the remainder of the wax, and finally cleaned in isopropyl alcohol.

The method was essentially the same for the GaAs antenna substrates, but as it was significantly softer, the grind was performed only on abrasive paper #1000. The material removal rate of GaAs was very sensitive to axial pressure on the core.

The read out error and repeatability of the measurements from the LVDT + voltmeter was in the order of $\pm$ 100 nm. The thermal expansion from a 60 mm long core, raised by 5 K, corresponded to 3.5 µm.

6.5.2 Antenna to lens positioning

A system was needed that would provide alignment between the antenna substrate back side and the silicon lens backside.

This was realized in two components; a camera-system to overlay two live image feeds, and a manipulator to displace the lens in front of the fixed antenna setup.

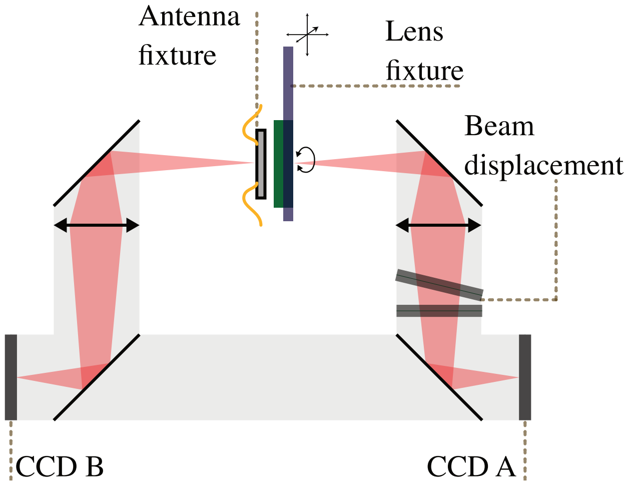

Fig. 48: The system for camera aided alignment. The images made on two CCDs are mixed in software. A beam displacement element allows for fine calibration to an external target. The lens fixture allows for the necessary four degrees of motion

The camera system is shown in fig. 48, where two CCDs image either side of the geometry. External illumination with red LEDs are not shown, but illuminates the antenna and lens arrays obliquely. A beam displacement element is provided in arm A, where two slabs of glass may be rotated on the optical axis, to displace the image. This allows for a pre-adjusted alignment of the camera system, with a patterned microscope slide as target. Note that the image of CCD A is mirrored in the software on its vertical axis, to match the image from CCD B.

As the beam displacement element provides 6 mm more high-refractive index in one of the arms, it introduces a scaling between the two images; the antenna array pitch stretches over more pixels than the lens array pitch. This has been found helpful in alignment. The antenna fixture is identical to the one presented in fig. 10 c), but without the lens tube on the backside due to geometric constraints.

Figure 49 show the output image from the camera system software. The software does not overlay any aids, these are all added for this visualization. The antennas are shown in green. A selection is outlined with green circles, and the insert show the position of the antenna with a dashed box. A green cross is drawn, passing through the central vertical and horizontal antennas.

Similarly, the lenses are outlined in red, but their large-scale geometry yields better contrast in the off-axis illumination. A similar cross is drawn, showing the difference in alignment.

The lens fixture is designed to provide fine adjustment of the beam-

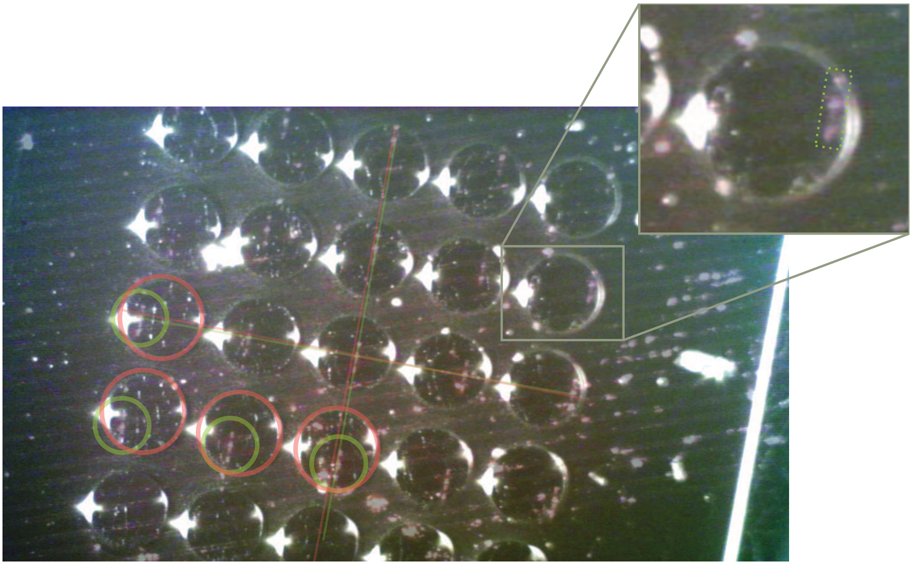

Fig. 49: Screen capture from the camera alignment system. The green overlays belong to the antenna structures. The insert show a dashed outline around a single dipole antenna, and the main image has 4 antennas outlined with circles.
Similarly, the red overlay identifies the lenses. Crosses for each element are drawn, to show the overlap. The antenna pitch is imaged larger than the lens pitch due to the beam displacement element in the lens arm.

transverse directions and rotation around the beam direction, for alignment with the camera system. The fixture must also allow movement along the beam direction to move the lens substrate into contact with the antenna substrate. It follows that a high lateral and rotational stiffness is required to enable reliable adjustments.

Conversely, the fixture must also provide significant low-force compliance in the beam direction, as well as angular compliance around the two beam-transverse directions. This compliance is critical for achieving a contact-interface between the substrates. Small errors in alignment will be absorbed in this mechanism.

Figure 50 show the designed mechanism; two beryllium-copper discs embody the compliant elements. The lens is mounted on a stiff aluminium bracket with cyano-acrylate glue. The bracket is fixed on the first disc, on the horizontal axis. The first disc is fixed on the second disc on the vertical axis. The second disc is mounted on the mounting ring on the horizontal axis. This set of connections provide the necessary compliance and stiffness.

The adjustment of movements are provided by a three-axis linear stage with micrometers (Newport M-461-XYZ-M) and a Ø 2" precision rotational stage (Thorlabs PRM2/M).

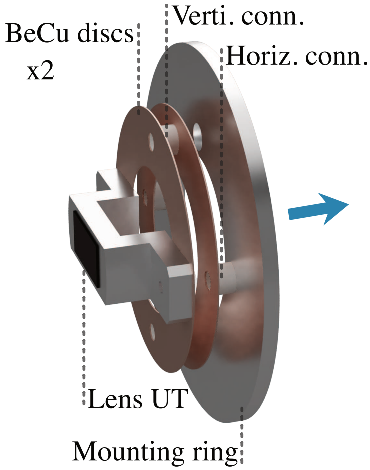

Fig. 50: The compliant mechanism that helps the interface between the lens and antenna substrates. Note that the screw connections are not shown to simplify the image. the Lens under test (lens UT) is mounted on a bracket with CA glue. The two beryllium-copper discs absorb angular misalignment in both directions, while providing a stiff connection in rotation and translation. The blue arrow indicate the THz beam propagation direction.

The procedure for alignment of a set of lenses to is as follows, starting from a mounted antenna fixture and micro-lens array:

- Mount a substrate lens for test on the aluminium bracket with CA glue, and mount the antenna substrate PCB.
- Remove the micro-lens array.
- Place the substrate lens alignment jig coarsely, aim for 1-2mm alignment accuracy in the transverse directions, good visible angular approximation and 5 mm beam-direction separation between the substrates.
- Displace the substrate lens fixture along the beam direction to achieve contact, and move in the opposite direction about 0.2 mm to just break contact.
- Place and align the camera alignment system manually. Due to the difference in imaging pitch, the central antenna must be centered in the image.
- Align the substrate lens to the antenna in non-contact mode.
- Move the substrate lens into contact. A small horizontal displacement was generally observed when contact was achieved due to initial angular misalignment between lens and antenna mounts.

- Repair alignment error from contact. Note that imperfect lateral stiffness requires gentle percussive excitation to break stiction between adjustments.
- Remove camera alignment jig and replace the micro-lens array and align for measurements.
- After measurement, the lens substrate is removed from contact along the beam direction. The entire fixture is removed, and a hot air gun is used to break the CA bond.

6.5.3 Characterization of etched lenses

A wafer of with deep etched lens geometries was fabricated by Jacek Fiutowski (University of Southern Denmark) and Arkadiuz Goszczak (Institute of Science and Technology, Austria).

A Bosch process was used to etch deep geometries with vertical sidewalls into a silicon wafer.

The fabricated wafer was diced, and the etch depth was measured in a scanning electron microscope (SEM) (see fig. 51). The measured etch depth was 101.9 µm, where the target depth was 125 µm.

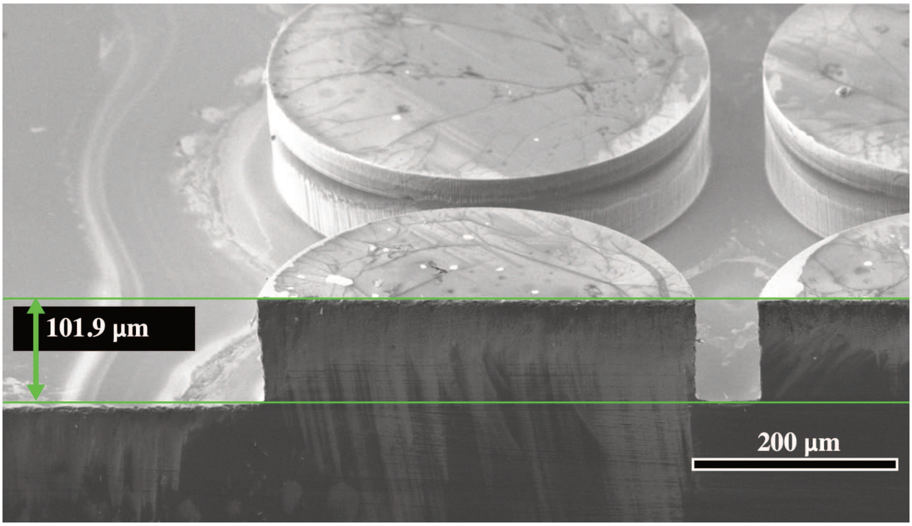

Fig. 51: SEM secondary electron micrograph of array lenses at 63° from vertical, 128x magnification and 10 keV beam energy. The image is taken from the edge of a lens array, cut through with the dicing saw. The succesful Bosch process has left vertical sidewalls, and flat etch bottom surface.

6.5.4 TDS measurements of the substrate lenses

The setup is essentially similar to that of fig. 37, with the exception of the substrate lenses in contact with the backside-thinned photoconductor array. For the single antenna characterization, an aspheric lens was used to focus 10mW of the pump beam intensity onto the antenna.

The lock-in amplifier was set at 50 nA full scale, at 100 ms time constant. The current input was used. The reference frequency was set to 35.42 kHz, with a peak-peak voltage on the emitter of 40 V.

The best performing antenna was a bow-tie antenna (BT28), and all the presented data is from that device. This subsection will contain the results from the measurements, and is arranged in three parts; the arrayed antennas with a selection of lenses, the central antenna only with the single lens, and finally a comparison between arrayed and non-arrayed lensed antenna emitters.

Nine configurations were tested:

- Thinned array excitation (TAE), no backside substrate.
- TAE, 450 μm flat silicon substrate.
- TAE, array lens, radius 200 μm, substrate thickness 190 μm.
- TAE, array lens, radius 200 μm, substrate thickness 205 μm.
- TAE, array lens, radius 225 μm, substrate thickness 215 μm.
- TAE, array lens, radius 225 μm, substrate thickness 205 μm.
- Thinned single excitation (TSE), no backside substrate.
- TSE, 450 μm flat silicon substrate.
- TSE, optimal single lens, substrate thickness 205 μm.

The following three subsections show the data analysis of the emitter configurations. Three different visualizations are reported;

The time trace show the peak-peak current which is measured, and indicate the strength of the internal echo.

The autocorrelation of the time trace is used as a first order measure of the echo from the substrate impedance mismatch to the air.

The frequency content , scaled linearly for the arrayed emitters, and on a log scale for the single emitter due to the higher bandwidth.

The estimation of the echo strength is interesting, as it describes an aspect of performance of the substrate lenses. Aiming towards full out-coupling of the generated THz radiation implies no internal reflection on the output interface.

Two echo positions have been indicated in the autocorrelation plots. The temporal position of the echo from within the antenna substrate is indicated with a solid vertical line, and the position of the echo from the entire substrate stack is indicated with a dashed line. Figure 52 sketches the two first reflections in the time trace.

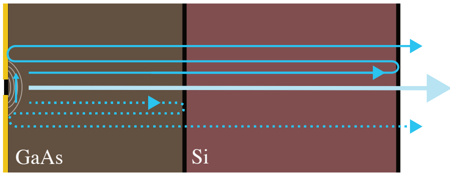

Fig. 52: Sketch of the reflections inside the substrates. The thick bright blue line indicate the direct propagation of the primary pulse. The thinner blue line indicate the propagation of the reflection for the full substrate stack. The dashed thin line indicate the propagation for the reflection occuring for a poor substrate impedance match.

6.5.5 Arrayed emitters

The timetrace of the arrayed emitters is shown in fig. 53. The peak-peak current that was measured is overlaid with the respective time-traces. It can be observed that the echo is supressed when adding the lenses. The displacement of the various traces in time is due to substrate thickness variations.

The autocorrelation (shown in fig. 54) is used as an estimator for the echo position. The figure show the autocorrelation for the six traces, and especially the blue line (only the antenna substrate) show a peak around the expected temporal position (the vertical lines) of the echo. Note that only the reflections for the full substrate stack is shown in fig. 54

To identify the echoes with the autocorrelations for the traces with a lens, a cropped version is shown in fig. 55. Here, the antenna substrate reflections are also shown to point out eventual mismatches in impedance, with dashed vertical lines.

It is observed that the green trace (etch depth 190 µm, radius 200 µm) seem to have a lower antenna substrate echo than the other measurements with lenses. In comparison with the peak of the antenna substrate (blue trace), the autocorrelations for the lensed antenna array show significantly lower reflections; for the purple trace (etch depth 215 µm, radius 225 µm) the peak is estimated to be 1/8th of the signal intensity, while the largest

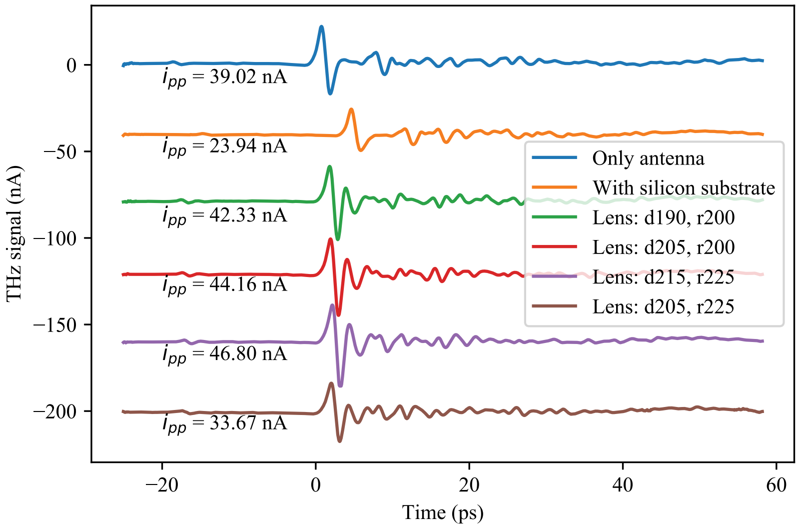

Fig. 53: The time traces for the emitter BT28 with various outcoupling geometries. The peak-peak detector current generally increases with an added lens. The characteristic of a single cycle pulse plus an echo is also suppressed with the substrate lenses.

full-stack echo is the red trace (etch depth 205 µm, radius 200 µm) is slightly better than 50% of the amplitude.

The linear scale frequency response of the time traces show a significant improvement with the lenses - see fig. 56. The purple trace is 30% higher in peak power spectral density than the reference without any outcoupling substrate. The log scale response highlighting differences at higher frequencies is shown in fig. 57. The variation in performance is large. While the two lenses designed for 1 THz (red and green traces) perform similarly, the purple and brown traces (designed for 0.5 THz) does not. The difference in performance between the two lenses does not reflect the anticipated difference in design.

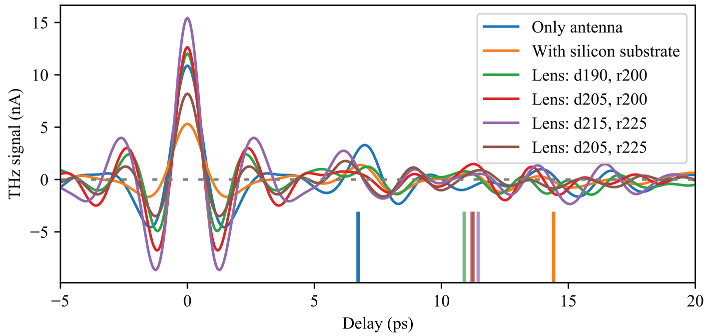

Fig. 54: The autocorrelation trace for the time traces with different lens geometries. The full vertical lines indicate the expected position for the echo from the full substrate stack.

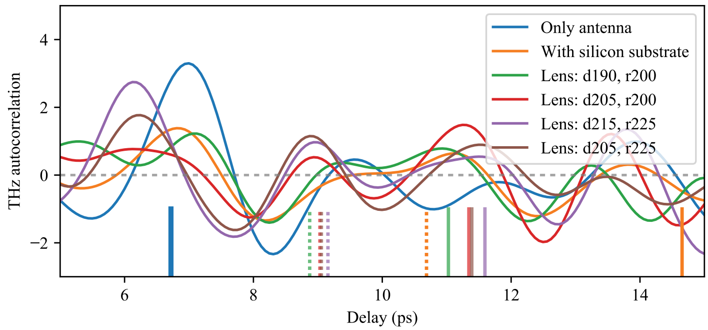

Fig. 55: A closer crop of the autocorrelations of the timetraces with different lens geometries. Compared with the full stack echo around 6.8 ps, there is a significant suppression with the lenses.

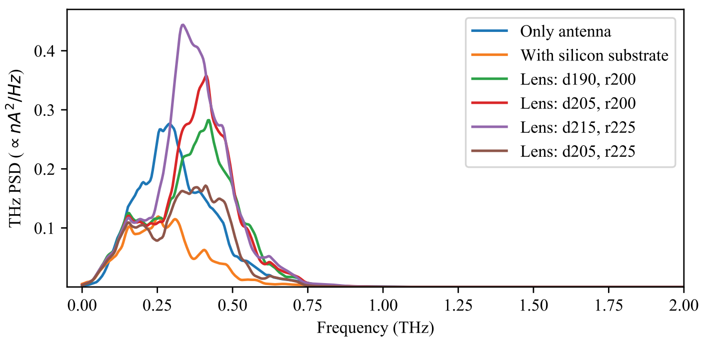

Fig. 56: The linear scale frequency responses of the arrayed emitter with different lens geometries. The r200 design is optimized for 1 THz, while the r225 design is optimized for 0.5 THz.

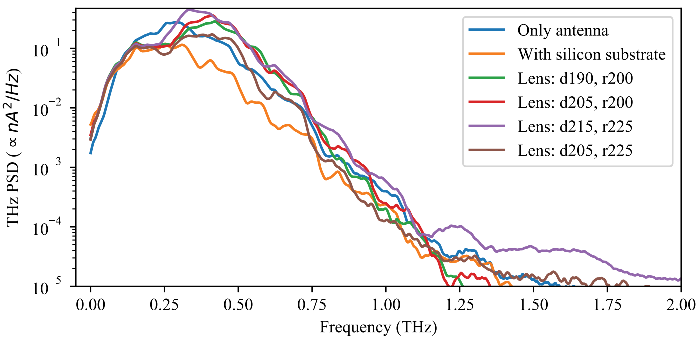

Fig. 57: The log scale frequency responses of the arrayed emitter with different lens geometries. The r200 design is optimized for 1 THz, while the r225 design is optimized for 0.5 THz.

6.5.6 Single emitters

The time trace of the single emitters is shown in fig. 58. The echo is difficult to identify for the lensed timetrace, while the peak-peak current is 20% smaller. The timetraces for the flat silicon substrate is very similar to that of only the antenna substrate.

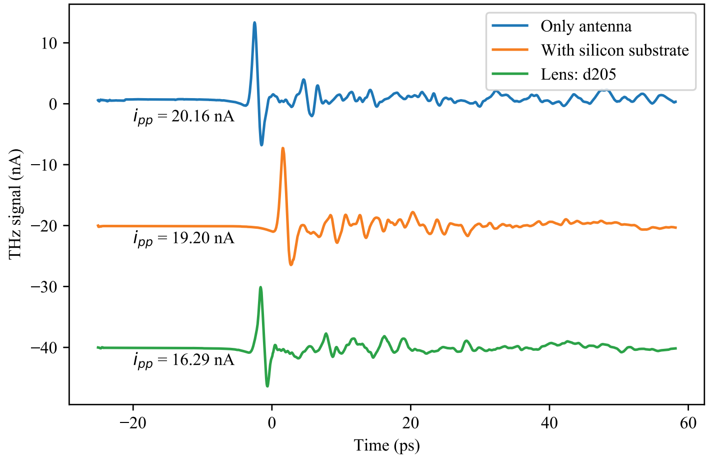

Fig. 58: The time traces of the single emitters. The peak-peak current is significantly smaller, but the echo is not as evident.

The autocorrelation in fig. 59 confirm the suggestions from the timetraces; an unidentifiable peak position for the lensed full stack echo indicates full suppression. The strong echo at delay position 5.5 ps for the flat silicon substrate indicate a poor contact interface between the lens and the antenna.

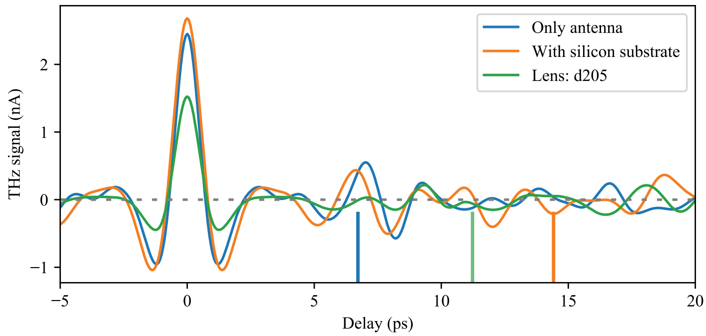

Fig. 59: The autocorrelations of the time traces of the single emitters show significant suppression of echos, outlined at the green vertical line.

6.5.7 Comparison between arrayed and single emitters

The comparison is done based on three characteristics; the time traces, the frequency response of the time traces in linear scale, and the frequency response in dynamic range. As only one array lens and one single lens substrate matched in grind thickness within a 10 µm tolerance, they have been compared here. The array lens with a radius of 200 µm and a substrate thickness of 205 µm and the single lens with a substrate thickness of 205 µm are used.

The array lens was traced in red in the previous plots, and will now be traced in full green. The comparison of the time traces show the improvement in performance from the array excitation. A 100% increase in peak-peak current is seen for the bare antenna substrate, while this does not hold for the lensed antenna. In any case, the echos are suppressed with the lenses, while this is not the case for the flat substrate traces.

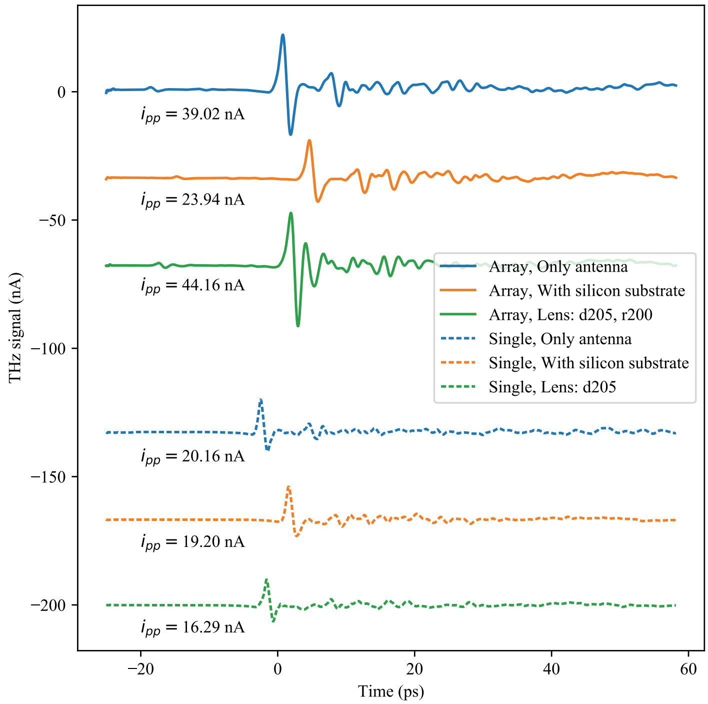

Fig. 60: The time traces of the six configurations. Note the increase in peak-peak current when going from a single emitter to the array.

The comparison in dynamic range (fig. 61) point out three significant things. Firstly, The logarithmic scaling highlights the larger bandwidth of the single antenna excitation. An extra increase around 1.5 THz is observed.

Secondly, the performance of the lensed array show a 10 dB higher dynamic range at 0.5 THz than compared to the bare antenna substrate. It is a few dB further improved with respect to the flat silicon sample. An improvement of the dynamic range is seen in the entire frequency range from 0 to 1.75 THz for the lensed emitter.

Thirdly, it is observed that the dynamic range does not show any benefit in using an arrayed emitter. While the signal peak-peak current was significantly higher, the noise intensity was also higher, and as this is the reference for the dynamic range, the dynamic range is not significantly different.

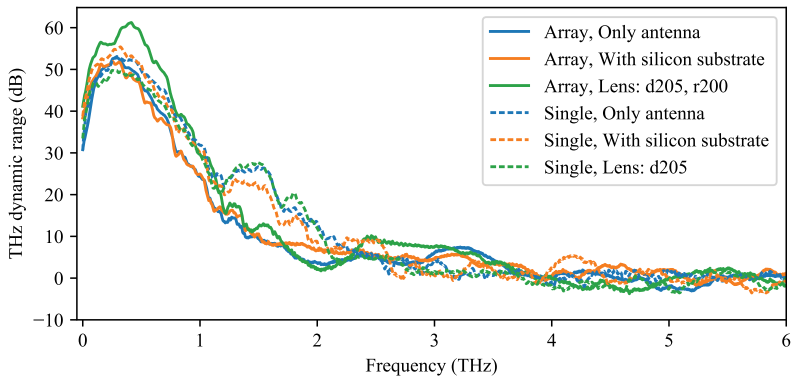

Fig. 61: The dynamic range of the six configurations of emitters. They are generally similar, but the lensed array stands out. An increase in 10 dB from the bare antenna substrate is observed at 0.5 THz, but the dynamic range is higher in the entire signal range. The single emitters and the arrayed emitters have similar dynamic ranges.

The absolute, linear scale power spectral density (fig. 62) does however show the tremendous improvement by changing from a single antenna to an array. A peak improvement for the bare antenna substrate of 557%, and a peak improvement of the lensed array substrate of 1290%.

The evolution in performance of the BT28 sample is interesting compared with the previous devices. BT28 was not one of the samples that were characterized in the previous comparative experiments, but fig. 63 show the comparison with four other bowtie-antennas from the same wafer.

The primary performance plot is shown in fig. 63. It is observed that the dynamic range is increased significantly compared to the other bowtie emitters. Applying the single lens also increases the bandwidth by almost 0.2 THz. It is not investigated whether the increase in performance from the population of bowtie emitters to the single, thinned lens is inherent in the emitter or it is due to the backside thinning process. The array emitter gains 3 dB in peak dynamic range, while the bandwidth is slightly decreased.

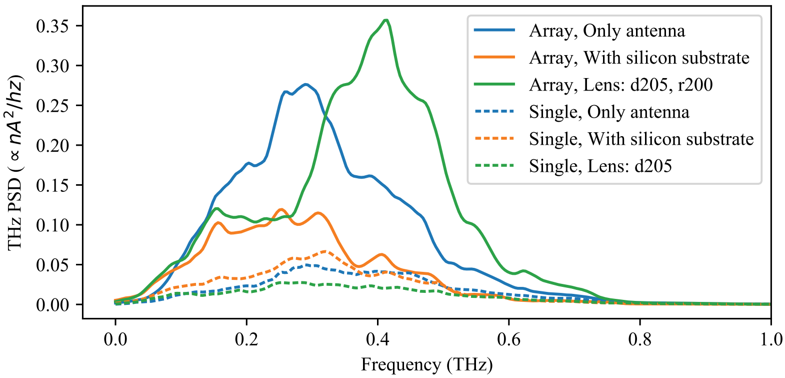

Fig. 62: The linear, absolute frequency response of the emitters. It is evident that the arrayed emitters (full lines) produce a significantly larger signal in terms of amplitude, than the single emitter (dashed lines)

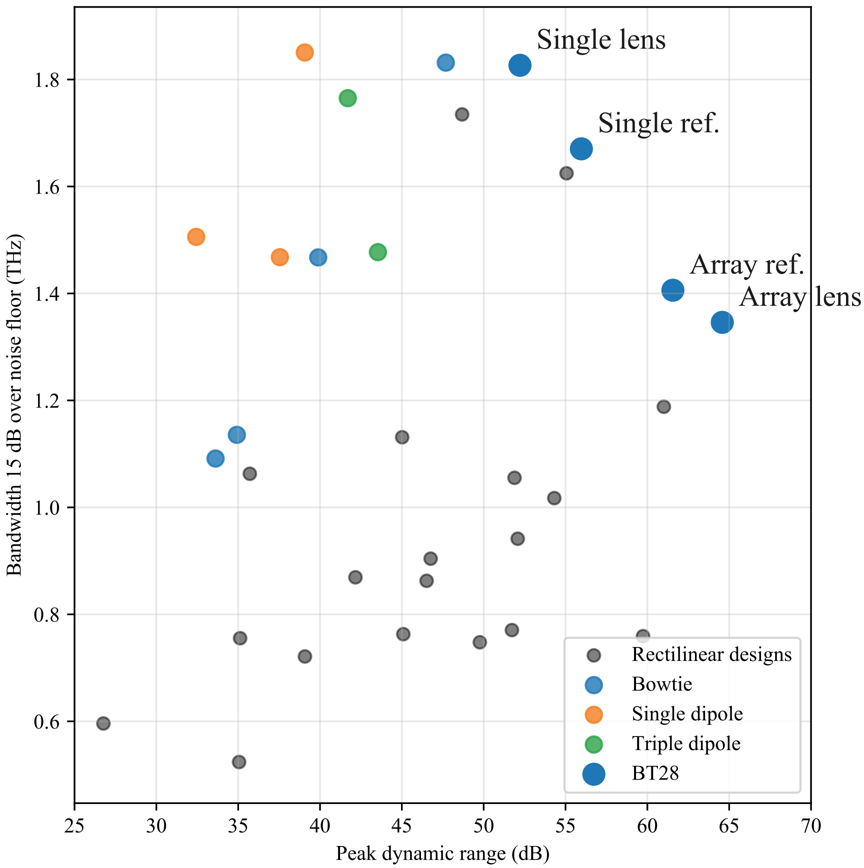

Fig. 63: The performance of the BT28 emitter, relative to the performance of the rectilinear designs and the slanted array antennas with large silicon outcoupling lens.

6.6 Additional experiments

Other relevant experiments have been performed. They motivate some of the design choices, and explore a sliver of the available parameter space in characterization and implementation of PCA emitters.

6.6.1 Thermal annealing of Ti/Au films on GaAs

It was relevant to investigate if there were any performance gain from annealing of devices, as other substrate/metallization combinations (e.g. Si/Al) require annealing to obtain ohmic contact.

Two samples (similar results, only one presented in this section) were prepared with one antenna centrally on a rectilinear array die. The procedure between the reference measurement and the comparison measurement was to remove the PCB, anneal and remount the sample. The CA bond to the PCB was broken by heating to 200°C for 2 minutes on a hotplate. This is similar in temperature to the solvent bakeout for the *mma polymers used as positive resist for EBL, so no further change in substrate performance is expected.

It was annealed in a rapid thermal annealer, in a nitrogen atmosphere with monitored oxygen content. Less than 10 ppm oxygen was measured. The samples were exposed to 320°C for 2 minutes, and cooled down. The samples were extracted when the temperature reached 125°C. TDS measurements were performed on the devices before and after annealing with identical stepsizes and LIA settings.

Figure 64 show the significant decline in performance when annealing Ti-Au metallization on GaAs substrates. 20 dB of dynamic range as well as a factor of 10 peak to peak current is lost. This practice has thus not been used in the project.

6.6.2 Bipolar or unipolar bias excitation

The bias voltage polarity was investigated, to show the difference between unipolar or bipolar excitation voltages. Furthermore the influence of waveform shape was also tested, as both sines and square waves were tested.

Five cases were tested, on the best performing antenna in the rectilinear arrays (Short choked, #74). The alignment was kept the same, so the only parameter which was changed was the bias voltage. The reference from the function generator to the LIA was provided through a TTL output, so the phase of the LIA was unchanged as well.

The following experimental cases were studied:

- Positive unipolar sine: ranging from 0 V to 20 V.
- Negative unipolar sine: ranging from -20 V to 0 V.

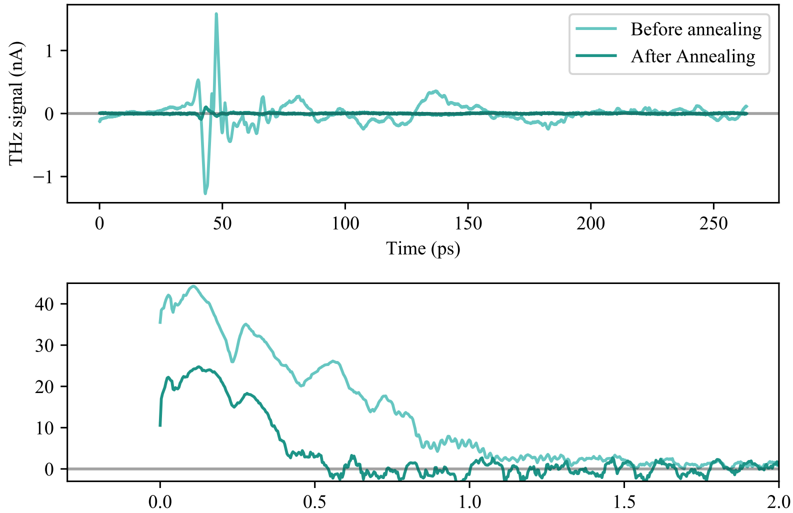

Fig. 64: It is observed that the annealing of devices with Ti/Au metallization attenuates the produced THz signal significantly. A decline in p-p current of more than 10 times is observed, as well as the loss of 20 dB dynamic range.

- Bipolar sine: ranging from $-20\,\mathrm{V}$ to $20\,\mathrm{V}$.
- Positive unipolar square: ranging from $0\,\mathrm{V}$ to $20\,\mathrm{V}$.
- Negative unipolar square: ranging from $-20\,\mathrm{V}$ to $0\,\mathrm{V}$.

Figure 65 a) outlines the tested waveforms and their polarities relative to the grey lines that indicate 0 V. The time traces are shown in fig. 65 b), where it is observed that the unipolar positive square waveform performs with the largest amplitude, positive unipolar sine next, and finally a slightly lower amplitude of the THz signal from the bipolar sine. The negative sine and square waveforms produce little to no THz signal. The observations from the time traces are not perfectly reflected in fig. 65; the highest dynamic range is measured by the positive sine, followed by the bipolar sine, and finally (about 10dB lower), the positive square.

As the dynamic range is in reference to the high-frequency noise, the signal scaling between the THz temporal amplitude and the dynamic range is not straight-forward.

Table 2 show the extracted data from the investigations. There is no significant increase in the dynamic range by using unipolar signals. Although the unipolar positive square show higher peak-peak signal in the time trace, this is negated by increased noise.

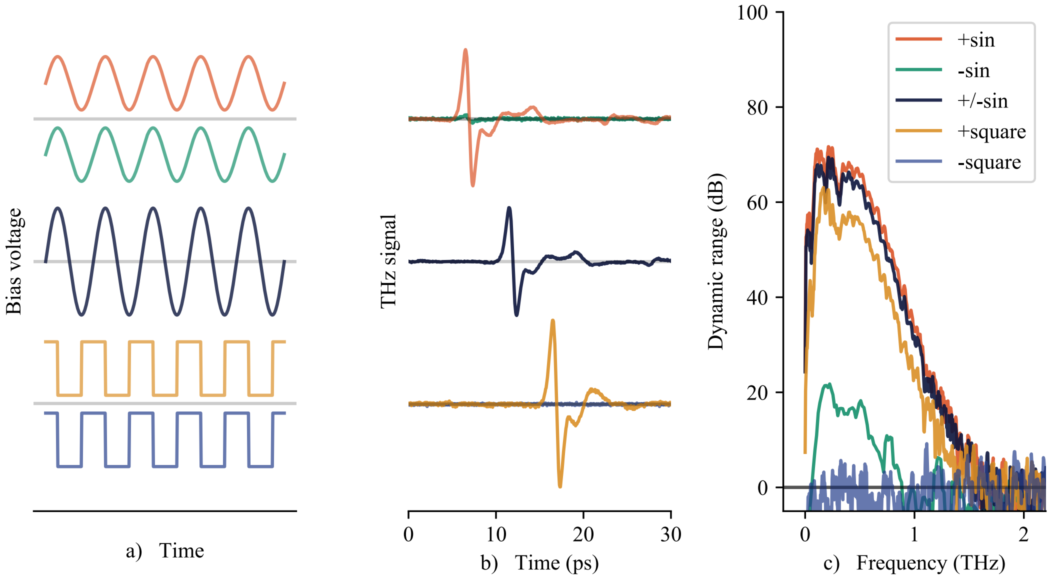

Fig. 65: a) show a schematic of the voltages. The grey line defines the 0-voltage for the various traces, and the colors remain the same across the three panes. b) show the time traces for the various bias voltages, with very little measured signal from the negative sine and square waveform. c) show the dynamic range of the THz signal at various bias waveforms. The dynamic range is with reference to the high-frequency noise.

A further benefit to the bipolar bias voltage is easier alignment. With the unipolar bias voltage, the user must align to a specific antenna half. This is also reflected in e.g. [23]. All the work in this thesis (except for the very first THz generation experiments) is done with a bipolar sine with an amplitude of 40 V peak-peak.

6.7 Failure modes for emitters

This section report the commonly observed failure mode for the antennas.

The failure mode has been observed only intermittently in this project. Antennas will perform reliably up until the point of full failure. No early warning parameters have been identified.

Figure 66 show a SEM micrograph of the observed failure mode for the antenna devices. The main image was acquired with an acceleration voltage of 30 kV, and shows the lower feedline that seems to bubble from surface. The image was sampled from secondary electrons, so some topographical information may be derived. It was observed that the bubbles underneath the metallization only occur under one polarity, but under the entire surface,

Bias type	Range (V)	RMS power (mW)	THz (nA p-p)	DR@0.5 THz (dB)
Uni. pos. sine	$[0;20]$	29.1	1.911	65.4
Uni. neg. sine	$[-20;0]$	29.1	0.119	17.2
Bi. sine	$[-20;20]$	20.0	1.512	63.0
Uni. pos. square	$[0;20]$	20.0	2.337	55.4
Uni. neg. square	$[-20;0]$	20.0	0.065	-1.0

Table 2: The extracted values from the bias polarity data. The RMS power is the effective power dissipated in a reference resistance of 10 kΩ. The peak to peak current measured in a time trace is given along with the dynamic range at 0.5 THz.

within 20 µm to 50 µm from the edge of the metallization. The bubbling forms under the contact pads. The delamination is also observed on the exterior side, where no current density is anticipated.

The insert of fig. 66 shows an image with 2 kV acceleration voltage. The low acceleration voltage provided less penetration, and the irregular end of the lower contact electrode was clear. It appeared to have been burned/melted away. The significantly lower acceleration voltage provides contrast between thinner layers due to the smaller penetration depth.

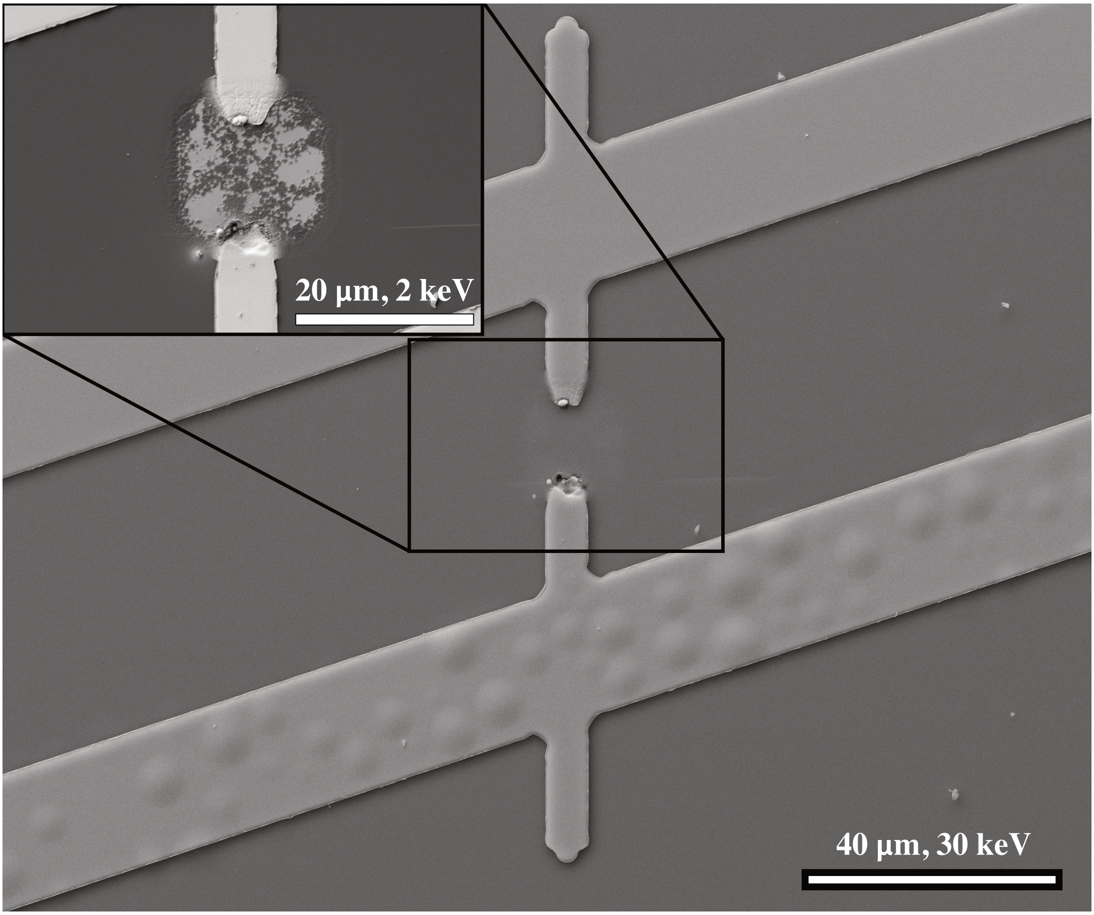

Fig. 66: Image of common failure mode. The main image and the insert is captured at different acceleration voltages, and the resulting penetration depths render significantly different contrasts. Note the bubbling under the metallization of the lower feedline, and the thermally damaged lower antenna contact in the insert.

7 Chapter summary

The previous section illustrates a continuous development in fabrication and time-domain characterization of photoconductive emitters. Some steps forward were made in terms of reproducibility, going from the EBL-defined antennas in the rectilinear array geometry into the slanted array emitters defined by a single lithography step. The used semi-insulating GaAs substrate is assumed to be the dominant limitation in terms of especially bandwidth. This was indicated in fig. 56, where the outer flanks are similar regardless of substrate-lens combinations. A higher bandwidth has been measured for single emitter excitation on slanted array feedlines, where spectroscopically useful bandwidth is estimated up to almost 2 THz.

A particular effort was made to improve reproducibility, as the rectilinear array results was so scattered that the spread of performance metrics was similar in size for both inter-design (between different designs) and intra-design (within the same design) measurements. This can be observed in figs. 26 to 29. The experiment was not void, though: Some meta-parameters were explored and it was found that there was a positive correlation between the illuminated resistance and the 15 dB power bandwidth - see fig. 26. This is contrary to the first-order perspective that the rate of change of photocurrent (proportional to emitted electric field strength) is dependent on a large dark resistance and a low illuminated resistance. A similar, but weaker correlation may be found in fig. 29, where the ratio R_{dark}/R_{illum} negatively correlated to the bandwidth. Two comments pertain to these results; it is the electric field and not directly the bandwidth that is correlated to the rate of change of the photocurrent. The second reservation is that the illuminated resistance was an average (sample time of several seconds) of the time-dependent resistance, that was dominated by the decay of the excited charge carriers. If it is assumed that the same amount of charge carriers is created by each consecutive laser pulse, the resistivity would drop and then increase as the charge carriers decayed. For long-lived charge carriers, the resistance would increase slowly and the time average (over $\approx 10^7$ pulses) would be lower. This argument indicates that a high illuminated resistance corresponds to lower life time carriers and subsequently higher bandwidth. A similar correlation is found in recent literature[76]. A positive correlation between the dynamic range at 500 GHz and 1 THz was also observed. A weak correlation between antenna designs was possible to identify from the frequency responses: The shortest antenna (in the short choked type) performed better than most other antennas. This indicate that the designed length of antennas was too long.

A slight improvement in clustering was observed for the slanted array antennas for all figures 33 to 36. Generally, the bandwidth was significantly increased for the population of tested antennas.

The array excitation of emitters provide roughly a 100% increase in the electrical field amplitude (proxy by peak-peak current), for the case of the best and only reported array (A bowtie structure). As the electric fields in the forward direction sum[68], it was expected to measure a 25 times higher amplitude. The performance was limited by two factors, however. Assuming that the BT emitter behaves similar to a TD emitter with respect to optical input power scaling (see fig. 84), a peak-peak current decrease of 25% is estimated. However, the dominant loss effect is assumed to be the mismatch of the detector volume to the transverse emission pattern. The interaction volume of the detector is the shared volume between the probe beam absorption region and the terahertz radiation. See fig. 44 for a sketch. An electro-optic detection setup (fig. 45) where the interaction volume is defined by the beam size of the probe beam. The signal to noise ratio for the measurement even with the full array excitation was very low (see fig. 46) and other work was prioritized due to time constraints. The calculated models of the array effect were also limited in prediction strength as the propagation through the substrate was entirely disregarded.

Placing the substrate lenses into contact with the arrayed antennas significantly improved the emitted power. While the peak-peak current did not increase more than 12%, the signal power spectral density changed dramatically. Figure 56 shows the linear frequency distribution. A local gain of 130% was achieved at 375 GHz, with reference to the bare emitter substrate. Overall, the lensed antennas all skewed the emission profile towards higher frequencies. The log scale frequency distribution (fig. 57) shows generally improved performance. The reference sample with a flat silicon die showed remarkably poor emission characteristics. While it could indicate that the performance of the lenses was even better, the strong echo in the same position as the bare emitter substrate suggested poor contact between the samples.

The claim that the emitter echo was minimized derives from the fact that the full stack echo (see fig. 52 for sketch) in fig. 55 had a lower amplitude than only the antenna substrate. The validity of this metric is limited, as the GaAs echo for the silicon substrate configuration had a decrease in peak amplitude of 50%, similar or slightly less than the full stack echo of the lensed measurements. It is relevant to engage further time-domain modelling of the echoes in the substrate stack to provide a better estimate of echo suppression.

For the single emitter and lens combination, it was observed that the peak-peak current was 20% lower and the echo was suppressed very well. The dynamic range showed a decrease (2-5 dB) in signal-noise ratio below 1 THz, when using the lenses. The dynamic range was however similar or slightly higher for the lensed configuration for frequencies between 1 and 2 THz. This was noteworthy in itself, as the signal had a bandwidth that was significantly higher than the arrayed emitters.

For the arrayed emitter, the lens array made a significant difference. 10 dB of dynamic range was gained in most frequencies up to 1.1 THz and somewhat less gain was seen at higher frequencies. The dynamic range was generally lower for the bare arrayed emitter than the bare single emitter. This was assumed to be due to increased noise coupling to the detector. The emission of RF noise at the optical pulse repetition rate is also modulated by the AC bias frequency, so the lock-in amplifier will not easily remove any coupled noise from this source. As the rate of change in current is significantly higher for an arrayed emitter, this configuration will induce more noise and limit the dynamic range. During the entire project, the dynamic range was limited below approximately 65 dB, both for the single emitters and the arrays. It was assumed that this was due to noise coupling between the emitter and the detector. The coupling could be minimized by employing a chopper in a focal point in the THz beam path, but this would limit the modulation frequency from 37 KHz presently used to well below 1 KHz, in turn increasing $1/f$ noise.

Due to miscommunications, the lenses were fabricated on unspecified boron doped dummy wafers. Some DC conductivity is thus expected, leading to losses for the propagating THz field and the lens performance should be considered a low bound. While the previous publications ([70, 71]) indicate that a strong dependence between the geometry and performance is expected, this was not found in the limited range of samples that were tested. Figure 57 show a slight advantage of using the lens designed for 0.5 THz (purple trace) at frequencies between 250 GHz and 400 GHz. This does not relate into significantly worse high-frequency performance than the geometries designed for 1 THz (red and green traces). The dependency on the substrate stack thickness was not identifiable at all.

The distribution of power to the various antennas (as described in section 6.4.1) was designed to minimize the difference in illumination power to 20%. This was a trade-off to the power irradiated on the emitters, as they only saw between 6 and 4 mW per site.

Backside thinning of the substrate lenses was successful and the abrasive method and the instrumentation was qualified within the specified tolerances. The contact assumes two flat surfaces and this required care in machining, as well as in mounting. The alignment procedure was functional and the optimal transverse position was generally found very close to the as-aligned position.

The error in scaling of the substrate conductivity in the initial simulations motivated a complication in the fabrication procedure. A SiO_2 spacer was introduced to limit the quiescent current through the substrate. It remains to be tested what influence this extra element will have. While it is assumed that it has a detrimental influence on emission efficiency and source-antenna coupling, it also assisted in a very specific incoupling geometry. The electrical contact to the substrate has been unique to the excitation sites and experience shows that the alignment of the large arrays is very benign; the resistance under illumination is minimized from several hundred $\mathrm{M\Omega}$ to below $10\,\mathrm{k\Omega}$ in a few iterations.

Secondary experiments found, in concurrence with previous literature[32], that the Ti-Au metallization was functional and did not tolerate or improve with thermal annealing. Furthermore, it was shown that the most efficient bias voltage scheme was a bi-polar sinusoidal excitation. A positive square wave voltage did show higher peak-peak current, but this was hampered by increased noise density, leading to a lower system dynamic range.

Sampling the generated THz field with an electro-optic crystal was done to provide a better spatial overlap between the detection volume and the spatially extended source. A weak signal was found, but the signal to noise ratio limits the conclusive power. It is observed that the temporal trace and frequency spectrum is not inconsistent with that detected with the photoconductive antenna. The experiment further precipitate a significant limitation to conclusions on the absolute magnitude of the bandwidth and emission power: All time-domain data in this section has been acquired with the same detector and only fig. 46 provide a cross validation with another sampling method. Any changes in response of the detector antenna has blindly been absorbed into the data. In reverse, as only one detector has been used, all time-domain results in this section are comparable in magnitude.

The results reported here are also subject to the robustness of the employed performance estimators. The 99% bandwidth was developed[74] as the conventional 3 dB bandwidth did not provide results that could be compared with results reported in the literature. A significant improvement was to estimate the bandwidth of a system as the highest frequency component with signal power that lies 15 dB above the high-frequency noise floor.

For the signal amplitude, two metrics were commonly used; the power spectral density and the dynamic range. The dynamic range is more difficult to interpret, as it assumes a reference to the noisefloor. Specifically, this work has taken the noise power reference in the high frequency half-range below the Nyquist frequency and this implicitly assumes that the system noise is evenly distributed. As the dynamic range estimator relies on the noise floor, it is naturally sensitive to lock-in amplifier settings. It was observed late in the project that the noise density changes with lock-in preamplifier settings as well, so comparisons of magnitudes in the dynamic range metric should be made with caution between the rectilinear array results and the slanted array results. The method furter relies on a flat noise floor, and this is most likely not fulfilled.

The failure mode that was observed (see fig. 66), was identified by sudden failure of function and a bubbling below the metallization. The delamination between the substrate and the antennas was observed at the entire perimeter of one electrode. Delamination was observed up to $50\,\mu\mathrm{m}$ from the edges of the Ti-Au stack. Note that this was also the case "behind" the bondwires, e.g. a position where no current would flow. That it has only affected one electrode indicates an electrostatic mechanism. Damage consistent with a thermal origin was observed on the delaminating electrode. This indicates that the delaminating electrode was the one closest to position of laser excitation. The non-delaminating contact is speculated to act as a ground reference and connect to the substrate. The delaminating contact is then charged and discharged by the bias voltage and this imposes delaminating forces in the capacitor between the degrading contact and substrate. It is relevant to investigate if the position of the excitation laser correlates to the side of the delaminating contact.

The results concerning the array emitters and their lenses will be described in a future publication (manuscript in preparation).

Part III

Two-color plasma terahertz generation

8 Introduction

This section describes the work on high-intensity two-color plasma sources, performed during my four months in Bordeaux, with Professor Emmanuel Abraham. The work considers primarily two-color plasma generation, and electro-optic sampling (EOS) in field-dependent birefringent crystals. The main topic of work is the phenomenon of conical emission from longer filaments. Furthermore, experiments in THz vortex beam generation are also documented here and limitations of the applied 2D EOS system with large bandwidth systems.

The initial motivation for choosing University of Bordeaux for the research stay, was the possibility of characterization of the etched substrate lenses, with the 2D EOS system in their lab. The system allows sampling of the THz field at a resolution that is effectively defined by the pixel dimensions of the CCD camera and the acquisition framerate. While the lenses were delayed, time for more fundamental investigations and familiarization with the two-color plasma THz generation technique was open, and this led to interesting findings.

Previous literature on the emission characteristics of the two-color plasma generation has concluded that it is emitted in a conical fashion, with zero intensity in the center. This zero central intensity is a defining trait of the so-called vortex beams in general, and it would be trivial to measure the spatial phase dependency of the generated light. Conical emission had never previously been observed with the setup in Bordeaux, even if the previous literature indicated that it should exist.

The ideas, and the key results, are published in [77] and [78] (the latter in preparation)

8.1 Previous results

A significant body of previous work describes the emission profile from two-color plasma filaments, and report a conical shape with a round, symmetric beam that has a depression of intensity in the center, named a conical emission pattern.

The first measurements and indications of conical was provided by Zhong et al.[7], where an aperture was scanned in a transverse line to provide 1D emission patterns. A severe HDPE lens was used for imaging, and electro-optic detection was used to acquire the THz waveform, and the THz pulse energy as well as the intensity at a selection of frequencies were compared to a simple propagation and interference model. Note that this paper is the only resource that measure and predict a positive correlation between frequency and ring-maximum divergence.

Subsequent work has employed incoherent detection methods to characterize the conical emission. Klarskov et al.[79] reported the acquisition of the conical power distribution and its propagation through a focal point. Spectrally resolved FTIR imaging was shown by Blank et al.[80]. The latter paper pointed towards the critical aspect of photoexcitation in the commonly used silicon filters, but continued to employ them. Recently, Ushakov et al.[81] proposed that conical emission only develops for numerical apertures below 0.025, and a gaussian-like unimodal distribution is present for focusing geometries with higher NAs. However, The reported results do not show clear conical emission profiles.

The theoretical model for the emission patterns was established by Zhong et al.[7], expanded by You et al.[82], with subsequent improvements to details by Gorodetsky et al.[83].

In discussions with Prof. Abraham it was mentioned that the conical emission that was described in the literature was never observed with the 2DEOS system. This disparity between the literature and the local experience further motivated the characterization.

Table 3 show an overview of the primary findings for the discovered previous work, where it may be gathered that some differences are found. [7] disagrees on the relation between cone occurrence and NA with [81]. [7] further disagrees with both [82] and [80] on the relation between cone opening angle and frequency. The former reference observing a positive correlation between the two, and latter two references observe and model a negative correlation. General disagreements between the model prediction and the measured opening angles are found in [82] and [80].

In general, a very wide variety of parameters (NA, pump power) have been investigated, and a conical emission pattern has been observed. It must also be noted that most references (with only [7] and [81] exclusive) have employed silicon filters to separate the high-intensity optical waste light from the THz wavefront. Gorodetsky et al. specifies that the silicon filter is preceded by a high-density polyethylene plate, without specifying thickness or proximity to the silicon filter.

The silicon filter is of particular concern to the author, and it is hypothesized that charge carriers generated by the forward-propagating visible light from the plasma filament introduces local lossed in the center of the silicon wafers. The methodology that will be followed is coherent and incoherent detection of the THz wavefront, with further care towards the filtering.

Reference	Filament length	Laser NA	Pulse energy	Method	Cone observ.	Cone HOA	Si filter
Zhong et al. [7]	3.9 - 35 mm	C: 0.056, SC: 0.014, NC: 0.005, 0.01	200 - 400 µJ	EO sampling, slit scan.	Yes.	5°@1 THz, 8°@2 THz.	No.
Borodin et al. [84]	"several millimeters"	C: 0.017	200 - 800 µJ	Golay cell, aperture scan.	Yes.	9.5°.	Yes.
You et al. [82]	10 and 40 mm	C: 0.016 (f=150 mm and f=300 mm)	1.3 mJ and 5 mJ	Pyroelectric detector scan.	Yes.	Model: 9°@1 THz, 3°@5 THz. Meas.: 5°.	Yes.
Blank et al. [80]	2 mm	N/D, f=100 mm.	310 - 715 µJ	FTIR, Golay cell scan transverse scan, and DFG with variable aperture	Yes.	Incoherent: 7-9° Coherent: 4°@<10 THz, 2°@>60 THz.	Yes.
Klarskov et al. [79]	20 mm	N/D, f=300 mm.	2.9 mJ	THz camera, bolometer-type.	Yes	3.8° from fig. 3.	Yes
Gorodetsky et al.[83]	2-17 mm	N/D, f=200 mm.	<30 mJ	Pyroelectric detector, aperture scan.	Yes.	<5°.	Yes. HDPE before with unknown separation.
Andreeva et al. [41]	15 mm	C: 0.023	< 1.5 mJ	FTIR, bolometer, slit scan.	Yes, above 4 THz.	2-6 °.	Yes.
Ushakov et al. [81]	2-7 mm	C: 0.02-0.025, NC: >0.035	2.5 mJ	EO detection and Golay, angular scan.	No clear indication. Model show conicity above 3 THz.	Model: 6-7°@>3 THz.	No. Only PTFE (and HDPE in Golay cell).

Table 3: Summary of previous literature. Abbreviations used are C: Conical, SC: Some conical profile, NC: No conical, N/D: Not described.

9 2D sampling methods

This section contains a general discussion of methods and instruments for 2D imaging of THz signals. Fundamentally, they are split into coherent detection schemes where both the phase and the magnitude is acquired, and incoherent detection schemes, that only measure the power. A comprehensive review of THz imaging methods may be found in [85].

9.1 Incoherent detection methods

Incoherent detection schemes measure the input power in a volume. Three detector types are dominant, and they are outlined in fig. 67.

The bolometer has a resistive sensing element thermally linked to a heatsink. As the sensing element changes temperature, the resistivity changes.

A functional small-signal model for the thermal responsivity of a bolometer can be written in terms of its physical parameters[86]:

$$R_{bolometer} = \frac{\eta P_{opt}}{G_{th}(1 + j\omega C_{th}/G_{th})} \tag{15}$$

where η is the absorption efficiency, P_{opt} is the input optical power, G_{th} is the conductivity from the sensing element to the heatsink, and C_{th} is the heat capacity of the sensing element. The assumption for the small-signal model is that the heatsink can always absorb the incoming heat through the conductive link, and that no Joule heating is coming from the sensing current through the element. The temperature coefficient of resistance for the resistive element material is fundamental for the thermal-electric conversion.

Equation 15 indicate the design tradeoffs that exists between rapid response and high sensitivity. A short response time would imply a low thermal capacity, and a good thermal connection to the heatsink. Conversely, a high sensitivity would demand low thermal losses to the heatsink, to build up a measureable temperature in the sensing element.

The bolometer is inherently sensitive to temperature changes, and drift is counteracted through modulation and lock-in detection or gating. Any selectivity in frequency of the incoming light is provided from preceding optics or specific absorber materials. Very high responsivities are possible for liquid-helium cooled bolometers, reaching $\approx 10^7\,\mathrm{V\,W^{-1}}$, with low noise-equivalent power (NEP) of $\approx 10^{-14}\,\mathrm{WHz^{-1/2}}$[33]. For room temperature bolometers, these figures are significantly worse.

The pyroelectric detector relies on the spontaneous electric polarization of a crystal between two electrodes. This polarization is dependent on the temperature, and this change in voltage can be measured. As the change in surface charge is very small, the steady-state quickly dissipate into the measuring circuit. Due to the very large source resistance ($1 \times 10^{10}\,\Omega$ to

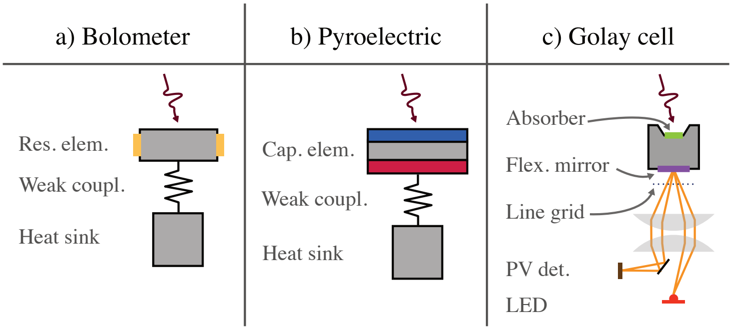

Fig. 67: The three dominant methods of incoherent THz detection. a) Bolometers functions by the temperature changing the conductivity of the resistive element (Res. elem.). b) The pyro-electric detector has a capacitive element (Cap. elem.) which changes polarization with temperature. This provides small changes in voltage on either side. c) The golay cell is a thermo-mechanical detector, where a gas in a small volume expands upon heating. The expansion is detected through movement of a flexible mirror membrane, that changes the transmission of light through a line pattern.

$1 \times 10^{12}\,\Omega$[33]), a very high impedance interfacing circuit is necessary. The small-signal responsivity of the pyro-electric detector is given by:

$$|R_{pyro}| = \frac{p\omega R_E A}{G_{th}\sqrt{1+\omega^2 C_{th}^2/G_{th}^2}\sqrt{1+\omega^2 C_E^2/R_E^2}} \tag{16}$$

The responsivity suffer from essentially the same drawbacks as the bolometer, with the same trade-off between responsivity and speed: p is the polarizations sensitivity to temperature, ω is the modulation frequency, R_E is the electrical resistance (acting as a gain in the transimpedance amplifier), A is the active area of the device, and C_E is the electric capacitance. Note that this also scales linearly with the area. High capacitances will also lead to challenging design issues with stability in the high gain current amplifier. Pyro-electric detectors also suffer from mechanical noise due to induced piezo-electricity. Typical values for responsivity and NEP are $\approx 1\,\mathrm{kV\,W^{-1}}$ and $\approx 10^{-9}\,\mathrm{WHz^{-1/2}}$, respectively, for room temperature devices.

The Golay cell is an opto-pneumatic device that relies on a change in gas pressure, due to expansion from heating. A gas volume is heated from the incoming radiation, and a flexible mirror on the backside of the cell moves. Optical pickup is done with a laserdiode or a LED, that has a particular focusing geometry onto a photodiode. In fig. 67 the Golay cell is shown with a line mask array. For 0 excursion, the flexible mirror will image the line grid back onto other periods, thus providing a change in transmission, dependent of the flexible mirror expansion.

A similar small signal responsivity may be outlined for the Golay detector:

$$R_{Golay} = \frac{\eta P_{opt} V}{G_V(1 + j\omega C_{th}/G_V)} \tag{17}$$

Equation 17 resembles equation 15, except an inclusion of the air volume V. Similar to the electrically coupled thermal detectors, a leak path G_V is also provided to prevent 'charge' build up. A vent hole allows slow exchange of air to the outside, negating atmospheric effects and drift with temperature. This dominates the leak path, and the thermal leak is not included in the above approximation.

Commercial devices show comparably good responsivities and NEP figures of $100\,\mathrm{kV\,W^{-1}}$ and $1.4 \times 10^{-10}\,\mathrm{WHz^{-1/2}}$, respectively (Tydex GC-1P). The main drawback is the large size due to the internal free-space optics, and the sensitivity scaling with volume. Due to the leak path, similarly to the other mentioned devices, a steady state signal cannot be measured. The wavelength response of the mentioned commercial device ranges from 15 µm to 8000 µm, limited by the HDPE window on the high-frequency side, and the aperture diameter on the low-frequency side.

9.1.1 Limitations of incoherent detection methods

The primary limitation is the absence of specificity, as exemplified by the vast Golay cell response region. They are inherently power detectors, and will measure any absorbed radiation. Secondarily, the detectors rely on comparatively large volumes/areas for detection, in turn decreasing sensitivity for focal plane arrays. While arrayed detectors are available, a significant amount of previous literature reports imaging with aperture scanning.

9.2 Coherent 2D acquisition methods

The 2D electro-optic sampling (2DEOS) system in the LOMA lab in Bordeaux is based on a system first described by Wu et al.,[87], and later Jiang et al.[88]. A sketch of the setup is shown in fig. 68, panel a). It is essentially similar to an ordinary EO setup, but a large diameter EO crystal allows simultaneous sampling of an entire THz wavefront. A collimated probe beam samples the induced birefringence, but instead of a differential measurement, a single crossed polarizer suppresses the significant intensity of light that has not been retarded. Further details may be found in [89].

Alternatively, a differential setup was developed[90], (see fig. 68, panel b)) where the linearly polarized light is retarded by a QWP, to give perfectly circularly polarized light for the case of no THz field. A polarization-sensitive beam splitter (figure show a Wollaston prism) delivers the orthogonal polarizations of probe light to different regions on an imaging sensor. The difference between the two regions is proportional to the electric field.

For both systems, a signal acquisition is a sequential process, where a delay line samples various temporal instances of the THz field with the probe beam. The data is a set of images one for each instance in time. This video of the THz wavefront may be pixel-wise Fourier transformed to provide a hyperspectral cube of the wavefront. It is a significant advantage to the method that it is inherently frequency sensitive, and that the phase of the frequency components is measured as well, contrary to the discussed incoherent methods.

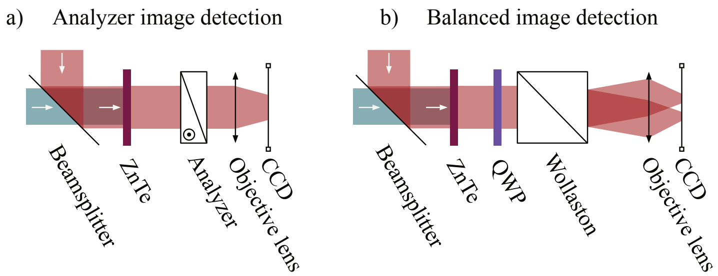

Fig. 68: Balanced vs single-ended systems for 2D THz detection. In pane a), the analyzer image detection system is shown. The THz induced birefringence is measured by blocking the input beam with a crossed polarizer, and quantifying the magnitude of the probe pulse which is rotated.
Pane b) show a complementary setup where a QWP is used to change the polarization from linear to circular, in the absence of THz signal. Any induced birefringence in the EO crystal gives elliptically polarized light, that is then split into vertical and horizontal polarizations by a Wollaston prism. The difference in intensity is then calculated by continuous subtraction of two image regions in software.

9.2.1 The triggering system

For the single-ended system, the SNR of the system is increased by the dynamic subtraction of sequential frames, timed by the chopper. The first reference of a similar system is reported by[88]. A fs pulse train with a repetition rate of 1 KHz is divided into the probe and pump part. The THz is generated by the pump beam, but a synchronized chopper picks off every second pulse, to provide a THz pulse train with a repetition frequency of 500 Hz. A very fast CCD is synchronized to and images each probe pulse, and a subtraction is made between the image of the probe pulse without THz signal, and the one with. A number of sequentially subtracted image pairs are averaged to further increase the SNR by a factor of $\sqrt{N}$. In contrary, the system reported by Blanchard et al.[90] (and in principle shown i fig. 68 b)) does not rely on the sample rate or synchronization of the imaging sensor.

9.3 Considerations for large bandwidth systems

This section describes the mentioned limitations of large bandwidth systems with only one analyzer. It applies to the Bordeaux system in particular, but as will be shown, it is primarily relevant at large bandwidths, using e.g. GaP crystals.

As the optics in the EO detection setup relies on polarization, Jones calculus is a helpful tool to develop models for the detector intensity in the case of single-ended or differential (balanced) optical sampling methods.

The result (as found in e.g.[91]), where the following detector intensity is derived for the single-ended measurement method, is:

$$I_{single} \propto I_0 \sin^2\left(\frac{\Gamma}{2}\right) \tag{18}$$

Where $\Gamma \propto E_{THz}$ is identical to the expression in eq. 12. As stated previously, the intensity difference in a differential measurement is given by

$$I_1 - I_2 \propto \sin\left(\Gamma\right). \tag{19}$$

Immediately, this indicates a problem; the square of the sine will introduce un-physical higher frequencies. This is sketched in fig. 69, where the sine and the sine squared of a fictive frequency response is shown. Note that the grey line of the true frequency response is completely overlaid by the blue line of the small angle approximation of the phase retardation.

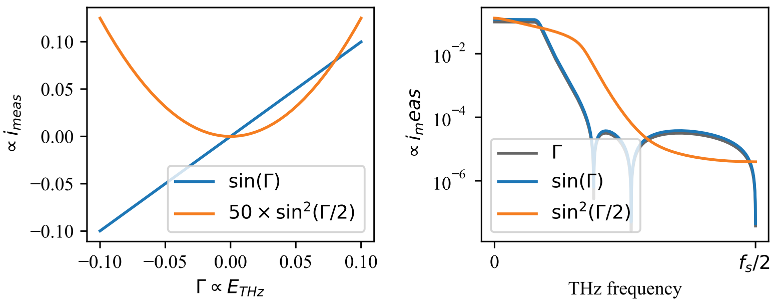

Fig. 69: Left panel; the response function of a sine and the sine square for small values. Right panel; The frequency response of a fictive signal (grey), with either the sine (blue) or the square sine (orange) applied. Scaling is done to normalize the two signals to each other. Note the high-frequency artefacts, and the decent low-frequency approximation to the true signal, for the sine squared detection method. The true frequency response is fully overlaid by the small angle approximation. The frequency response of the sine squared detection response is scaled vertically by 300, to roughly normalize the two detection methods.

Figure 69 show a frequency response for the differential detector which is practically identical to the true signal. The good approximation is also known as the small-angle approximation, where $\sin(x) \approx x$ for small x. Note that the low-frequency behaviour is approximated well, while the response function decay is significantly slower than the true signal and the differential method. During initial characterization of the 2DEOS system, this artefact was discovered in the data. Scans with differential measurements was significantly different from acquisitions with the single-ended measurements with the crossed polarizer before the camera.

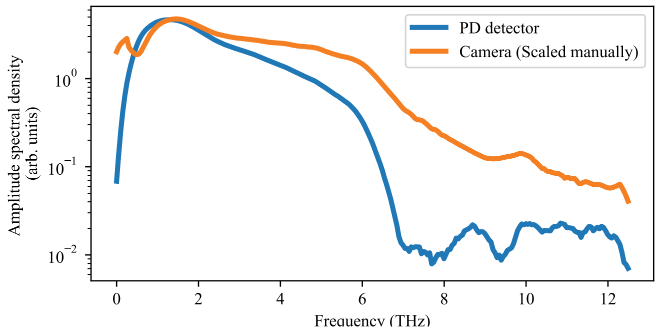

Fig. 70: Normalized measurements with both a differential photodetector system (PD), and the single ended, crossed polarizer camera system show significantly different response functions for the same EO crystal. The high-frequency artefacts are similar to the ones outlined in fig. 69, and vastly over-estimate the available signal bandwidth. Both signals have $f_s/2 = 37.5$ THz

Figure 70 show the frequency response of the same measurement geometry, a plasma source, collimated and focused into a GaP crystal by two off axis parabolic mirrors (OAPMs) with an EFL of 150 mm. The probe beam was passed through a small hole in the focusing OAPM, and sampled with the differential photodetector and the single-ended camera setup.

An artefact similar to that sketched in fig. 69 is visible in the data. Similar artefacts were also reproduced when sampling the electric field with a single photodiode, in a single-ended, cross-polarizer configuration (data not shown).

A solution to the artefacts seen with the single-ended measurements was described by Jian et al.[92]. By introducing a variable retarder (e.g. a Berek or Soleil-Babinet compensator) between the EO crystal and the crossed polarizer, another term may be added to the measured intensity:

$$I_{single} = I_0 \left[\eta_{scatter} + \sin^2\left(\Gamma_0 + \Gamma/2\right) \right] \tag{20}$$

where $\eta_{scatter}$ is light scattered by the crystal, Γ_0 is an induced bias from intrinsic bi-refringence in the EO crystal and added optical bias from the birefringence in the compensator.

By moving the effective bias point of the optical signal higher than $\Gamma = 0$, the sine square response function is used in a region that is more linear, and in any case does not square the output. Similar effects may be achieved by rotating the analyzer off the blocking axis slightly.

Guidelines are given[92] to optimize the trade-off between loss of dynamic range in the detector, and linearity; set the compensator to the minimum optical bias to measure the scattering and intrinsic birefringence. Adjust the compensator to provide twice the output intensity of the background, with zero THz input signal.

10 Conical emission of terahertz from long filaments

This section describes work aimed at characterizing and understanding the transverse emission profile of THz radiation, from two-color plasma filaments. As previously mentioned, the spatial transverse profile of the THz radiation is relevant to investigate, as the technique is very relevant in high-field THz science. Some non-linear spectroscopy methods like z-scans are based on the assumption of a Gaussian beam[93]. During the work towards creating THz vortex beams by introducing the optical vorticity into the pump light, the idea of the following work arose. The available detection instrumentation enabled phase and magnitude characterization of the previously reported conical emission patterns.

The core content of this section has been submitted for publication. The manuscript is provided in the appendix. The publication provides (to the best of the authors knowledge) the first report of a fully coherent measurement of the entire conical THz field emitted from a two-color plasma. The publication questions the present models of emission, while providing measurements showing a gaussian-like emission pattern, across a variety of numerical apertures and pump energies.

10.0.1 The You model

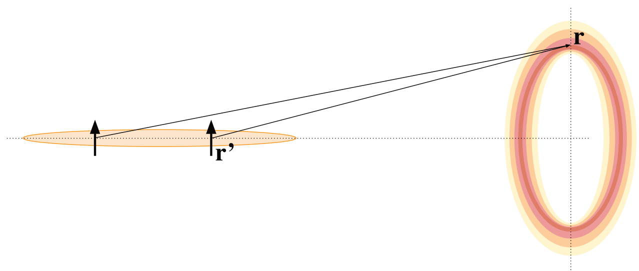

Fig. 71: Sketch describing the You model of conical emission. The conical emission was summed up from the superposition of continously distributed point sources along the filament. Distances $\vec{A}$ and $\vec{B}$ interfere constructively in the perimeter of the conical emission.

The You model describes the emission pattern by superposition of waves from point sources along a 1D filament distribution:

$$E_{THz} \propto \int_V \frac{\tilde{P}(r', \Omega)\ e^{ik_{THz}|r-r'|}}{|r-r'|}\, d^3r' \tag{21}$$

Where the THz source in point r' is locally defined as the polarization $\tilde{P}$:

$$\tilde{P}(r',\Omega) = \tilde{A}(r',\Omega)\sin\left[\theta(z')\right]\ \mathrm{e}^{in_g k_{THz} z' - i\Omega t} \tag{22}$$

Where $\tilde{A}$ is the generator amplitude in a point r' along the filament, at a specific THz frequency Ω. $\theta(z')$ is the phase walkoff between the ω and the 2ω optical beams from the BBO crystal, due to the slight variation in the refractive index in air. The last term describes the walkoff between the THz field and the optical fields.

By iterating through the points in an acquisition plane and summing up the contributions from the filament positions, the electric field may be mapped out. Fig. 72 show sections of the real part of the electric field radiated from a gaussian filament with FWHM of 10 mm.

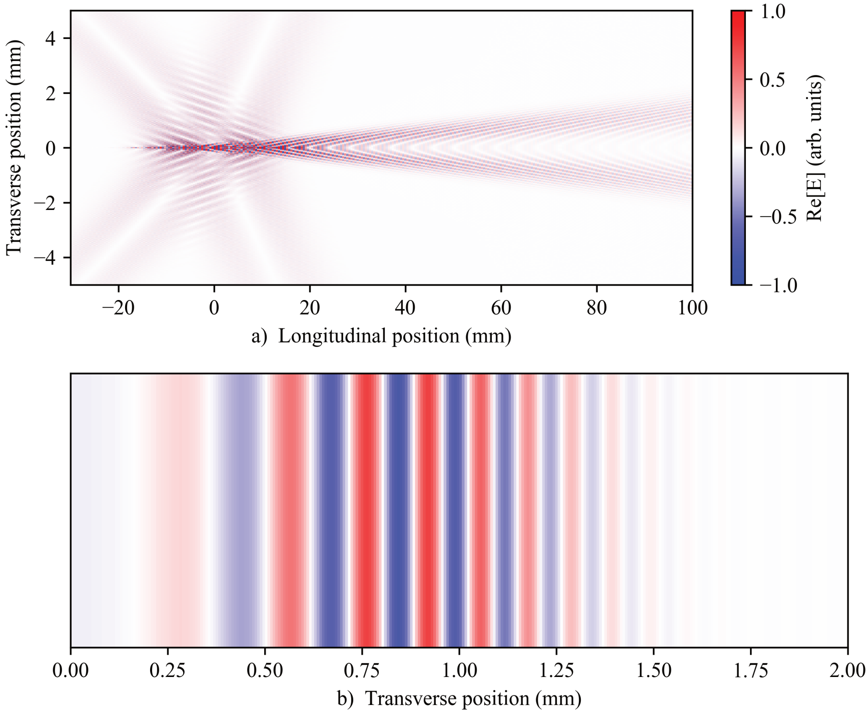

Fig. 72: a) The real part of the predicted E-field from the You model at 1THz, from a gaussian distribution of emitters in the plasma. Note the fast oscillations in the transverse plane. The upper panel show a forward emitted cone-like pattern. b) show a section near longitudinal position 100mm, on the upper lobe of the emission pattern.

The absolute magnitude of the emission profile is emitted in a conical fashion from the filament. The real part of the output does however predict very fast spatial variations that would be easily identifiable in a coherent 2D measurement. Transverse details are visible in fig. 72 b).

10.1 Incoherent angular resolved sampling

Hypothesis 1. *The silicon filter does not influence the spatial distribution of large-bandwidth THz radiation.*

To compare with previous measurements, an incoherent detector has also been used. A Golay cell was was set up to scan the THz intensity with angular resolution on the optical table plane. It was presumed that the intensity would be symmetric around the optical axis. The setup presented in fig. 73 was employed to do measure the THz intensity as a function of angle. The angular scanning was used to avoid parallax errors between the measurement aperture (AP) and the Golay cell aperture. Furthermore, two filters are employed to filter away forward propagating waste light (THz++ in fig. 73): A ceramic filter (96% alumina, thickness 1 mm, CSC ltd.) and a conventional silicon filter (thickness 1 mm, HR-FZ silicon, Tydex).

The silicon filter usefully transmits THz radiation, with the significant drawback that light below the bandgap ($\lambda < 1.1\,\mu m$) will excite charge carriers and induce strong reflective and absorptive losses in the filter.

The ceramic filter has only mediocre transmission properties for THz, but is a robust dielectric that scatters visible and IR light very well. The interchange of the filters was done to investigate the role that the silicon filter play in the generation of conical beams.

The laser input was 65 fs pulses with a center wavelength of 800 nm, and pulse power of 2 mJ where nothing else is mentioned.

Fig. 74 show the emission profiles measured with the incoherent detection setup. As the silicon filter precedes the ceramic filter, a strong central depression of intensity was developed. For the case of the ceramic filter preceding the silicon filter, there was a near-gaussian emission profile.

As mentioned, previous work has described a dependence between pump beam NA and emission profile, but for the ceramic filter preceding the silicon, no transition to conical emission profiles is observed (data and Gaussian fit in fig. 75). A gaussian emission profile provides a good fit to the observed angular distribution.

10.1.1 BBO angle

Previous literature has reported the exact orientation of the BBO crystal, and specifying axial orientation[94] as well as the vertical angle with respect to

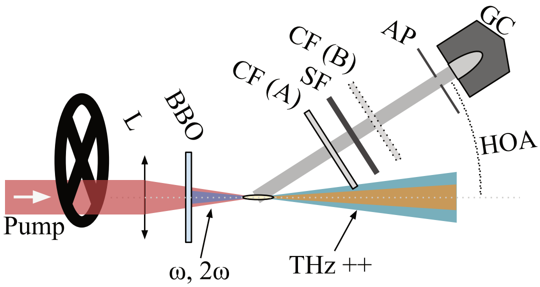

Fig. 73: The applied incoherent setup for angular resolved measurements of the THz intensity. A chopper (CH) modulates the pump beam generating the THz radiation, while a Golay cell (GC) may be scanned around the plasma center point. To provide some filtering, a silicon filter (SF) and a ceramic filter (CF) was used. The ceramic filter was either placed before the silicon (Case A) or after the silicon (Case B). An aperture (AP) provides the spatial resolution. Reproduced from[78], manuscript in preparation.

the beam normal[95]. While this work has followed the original method by Kim et al. for the axial orientation, and rotating to maximize the THz signal, it was found that the vertical angle displaced the conical emission.

Fig. 76 show the THz intensity behind the ceramic filter with a preceding silicon filter in an early iteration of the setup. Lines are added as guides to the eye, at the peak of each side of the conical emission, to demonstrate the imbalance in intensity. The y-scale shows the compound of the small angle deviation from normal in millirad (the grey lines) and the Golay cell signal. Contrary to the incoherent data reported elsewhere, this is acquired with a linear transversing Golay cell aperture.

A similar phenomenon was previously observed[79], where the authors observed an imbalance from the left side to the right side of the THz intensity map. For all other experiments in this work, the BBO crystal was adjusted accurately to be normal to the beam. Practically, this was done by aligning for counterpropagation of the frontside reflection through the beam delivery setup.

10.2 2D electro-optic sampling

Hypothesis 2. *The silicon filter has similar influence across all frequencies.*

The incoherent measurement techniques generally only image the intensity of the radiation (with the exception of FTIR-like measurements), and in any case does not provide any information on the phase of the frequency components.

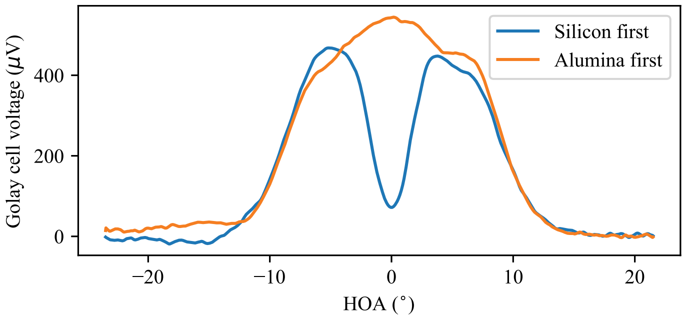

Fig. 74: Measurements of the angular resolved incoherent measurement signal, for the two orders of filters. It is seen that a strong central depression was only visible when the Si filter precedes the ceramic filter. The strong central depression could be mis-identified as conical emission. Reproduced from[78], manuscript in preparation.

A 2D EOS setup, as explained in section 9.2 was utilized to image the full waveform across the acquisition plane. A Ø25 mm ZnTe crystal was used to sample the electric field of the THz pulse.

10.2.1 Experimental geometry

Fig. 77 show the overview of the external beam delivery and delay that was used in all of the 2DEOS measurements presented here. The interaction region is specified in fig. 78.

In the general case, the coherent measurement requires a probe pulse that can be arbitrarily delayed (the light red beam in fig. 77). A telescope was used to expand the beam to minimize the gaussian fall-off near the edges, as the sampled signal would be proportional to the probe intensity.

Fig. 78 show the acquisition geometry for the experiments. The pump beam was modulated by a chopper, synchronized to the 1 kHz clock from the amplifier. A plano convex lens with a focal length between 150 mm to 500 mm focuses the pump light towards the plasma position. The BBO was placed as close to the plasma position as the laser induced damage threshold allowed.

The laser induced damage was the dominating driver of the sampling geometry; the plasma filament had lengths from 5-50mm, depending on the NA. Within the filament, damage would be immediate, but Kerr self-focusing was also observed, extending the zone where significant damage to the optics was problematic. The ceramic filter showed significant resilience towards ablation in the strong intensity after the plasma filament, but the silicon was damaged within 50 mm from the plasma center position. Some damage from ablation was considered acceptable, but catastrophic penetration of the silicon

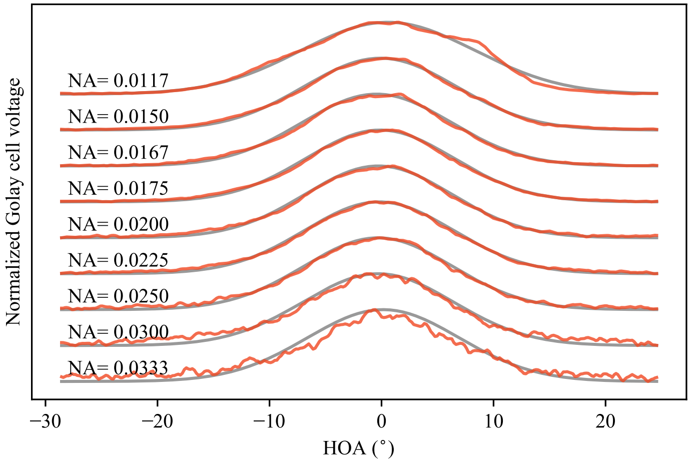

Fig. 75: Angularly resolved incoherent emission patterns (red lines), for a range of NAs. Note that the ceramic filter preceded the silicon filter in all cases. Gaussian distribution fits (grey lines) are overlaid.

would lead to damage of the large EO crystal.

Conversely, the separation between plasma region and EO crystal set the limit of the available half-opening angle (HOA) that could be measured, and increasing the available angle was a priority. A tolerable cumulative damage of the silicon filter was found in a position of 55 mm from the plasma center position. The first position of the ceramic filter (CF (A) in fig. 78) was approximately 5 mm further from the silicon position. The CF (B) position was between the silicon filter and the ZnTe EO crystal that was placed at 60 mm from the plasma center position. This gave an available HOA of 11.5°.

The probe beam was directed towards the EO crystal by a 50/50 beam splitter (BS), and reflected internally in the ZnTe, to co-propagate with the THz pulse in the crystal. This particular geometry leads to extra echos that have been cropped in time in the analysis, but it provides access to the near field of elements on the ZnTe surface, or as in this case, a very compact acquisition geometry. The reflection from the front surface was split again in the beam splitter, where an analyzer (a 15 mm Glan-Taylor polarizer, AN) and a large aperture objective lens (Nikon f1.4/50 mm, L2) focused the rotated probe beam onto the fast CCD. A variable ND filter was used to adjust the intensity, but this is not shown in fig. 78.

Software averaged the dynamic subtraction for 1000 frames on the camera (1 s). The probe delay line was moved 4 µm, and the process was repeated to acquire the THz waveform.

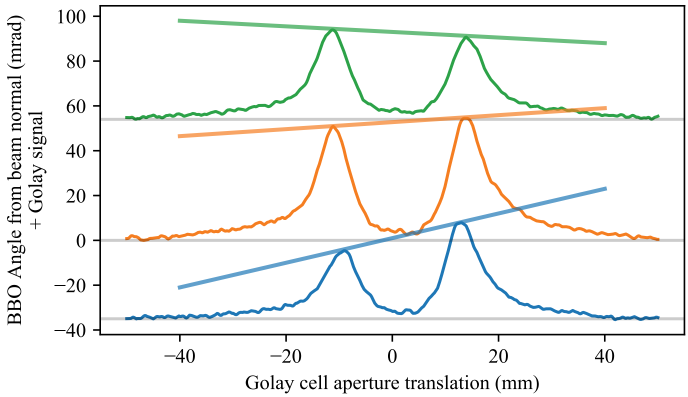

Fig. 76: The Golay cell signal for three BBO-beam incidence angles. Flat lines have been added as a guide to the eye to exemplify the imbalance between the peak intensities. Note that the vertical scale offset corresponds to the BBO-beam incidence angle in mrad.

10.2.2 Data analysis

The acquisition results in 876 temporal images with resolution 256x256 pixels. The assumed axial symmetry of the data was used to provide a 2D visualization of the data.

Hyperspy[96] was used for the data structuring and initial treatment of the data. The images are transposed into 1D vectors in time, and individually Fourier transformed. After a reverse transposition to slices in frequency, the absolute value of the slices yield images of the absolute magnitude of the THz radiation in the frequency bins.

By sampling and averaging in a polar coordinate system, the radial information could be plotted as a function of either time or frequency. Fig. 79 show the sampling positions in a given frequency slice as white dots. For the sake of this visualization, 14 different angles and 11 radii is sampled up to 80% of the full radius. In the full analysis 100 angles and 500 radii has been sampled up to 99% of the full radius. Significant oversampling was performed, but due to the polar sampling this did not lead to issues with different weighting of some radii.

As the probe beam was gaussian and not a flat top, this would influence the measured THz intensity. The dependency is linear, so a simple correction factor was made from an image of the beam intensity profile.

Fig. 80 show an example of a probe beam image, and the axial sampling points of the probe beam image. A gaussian function between 0 and 1 was fitted to the data that was within the aperture provided by the analyzer. The gaussian fit was chosen as division by the measured probe intensity would

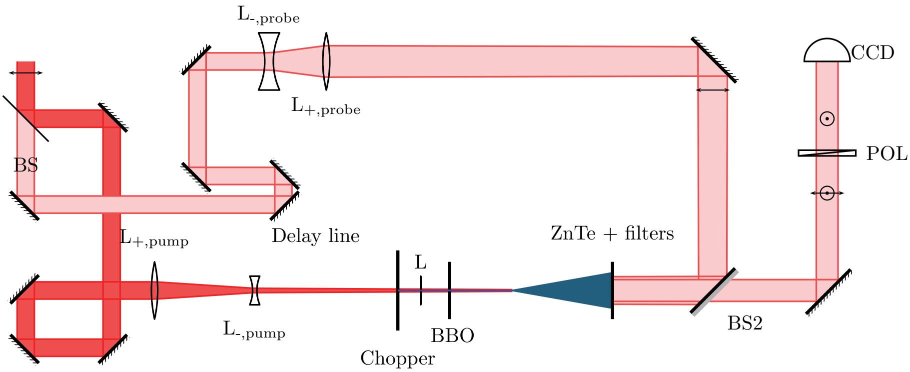

Fig. 77: The beam delivery layout for the 2DEOS system. A 95/5 beamsplitter separates the input beam into the probe and the pump arm. The probe arm contains a telescope ($L_{-,pump}$ and $L_{+,pump}$) to access lower numerical apertures, and the probe includes a telescope to expand the beam to provide a more even illumination of the entire EO crystal. A chopper at 500Hz modulates the beam, while a plano convex lens (L) focuses the pump light onto the BBO crystal, and further into the filament region. A secondary beamsplitter (BS2) was used to direct the probe beam to the EO crystal, while allowing the reflected light to pass through a polarizer (POL), an objective lens (not shown) and onto a CCD.

lead to super-weighting of the noise outside of the functional aperture of the instrument. Furthermore, each radial slice in frequency was normalized between 0 and 1 to maintain contrast for all frequencies.

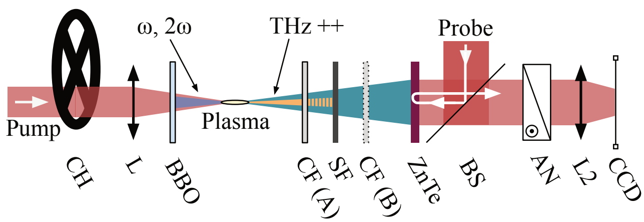

Fig. 78: Details of the 2DEOS setup used to characterize the THz wavefront produced by the two-color plasma filament. Abbreviations are: CH; chopper, L; Focusing lens, CF(A); Ceramic filter in position A, SF; Silicon filter, CF(B); Ceramic filter in position B, BS; Beamsplitter, AN; Analyzer (a crystal polarizer), L2; Objective lens for the CCD. Reproduced from[78], manuscript in preparation.

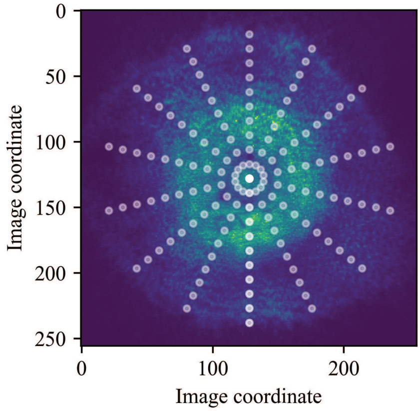

Fig. 79: Intensity distribution at an arbitrary frequency. An overlay visualizes the points for the axial sampling procedure that maps the hyperspectral datacube into a 2D plot, as a function of frequency and HOA. Each sample in discrete radii was summed around the . This image show the sampling positions in a given frequency slice, with 14 angles and 11 discrete radii.

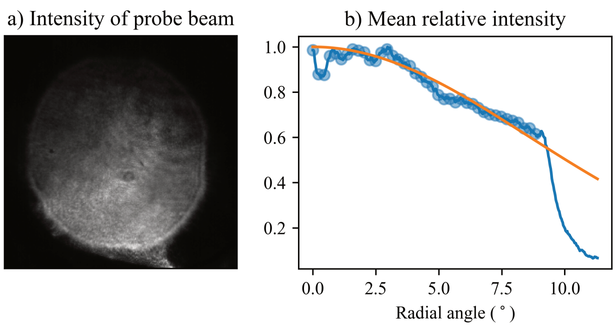

Fig. 80: a) Image of the probe beam intensity. b) The axially sampled mean relative intensity of the probe beam. The range of datapoints used for the fit is outlined with blue circles. The gaussian fit is shown in orange.

10.2.3 Results

Fig. 81 show the axially sampled amplitude of THz radiation for the two test cases. Inserts are provided to show the THz amplitude image. For the case of silicon preceding the ceramic filter, a significant depression is seen at most frequencies below 3 degrees HOA. The left panel in fig. 81 also show, in frequencies below 1.5 THz, a bright spot in the center of the frequency slices is present. The nature of this spot is compatible with diffraction around a central occlusion, a so-called Arago or Poisson spot. This is not visible where the ceramic filter precedes the silicon filter.

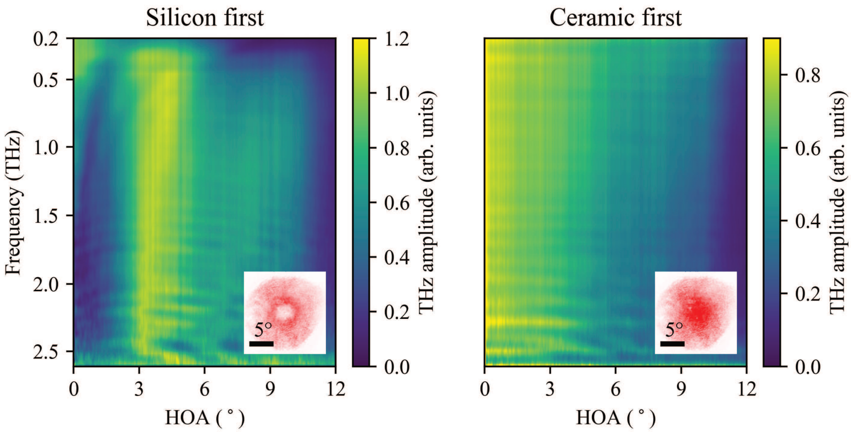

Fig. 81: The linear, normalized amplitude of the THz radiation as a function of HOA and frequency. The two relevant cases of the silicon filter first (where charge carrier generation and subsequent loss of transmission was possible), and the case where the silicon filter was protected from the forward propagating waste light by a ceramic filter. The inserts show the THz amplitude at 1.5 THz. Note the dark region in the lower angles of the *Silicon first* pane, where relatively smaller amplitude was measured. Adapted from [78], manuscript in preparation.

While the results in fig. 81 are normalized, the absolute power spectral density of the two experimental cases is relevant for future work. Fig. 82 show the sum of the power spectral density within the angle of acquisition. The sum total of the PSD of the two signals are 585.8 giga-units and 711.3 giga-units for the silicon preceding and ceramic filter preceding, respectively. This gives an increase in measured integrated power of 21% for the ceramic first case.

While the sum total power of the two cases favour the ceramic first case, it is worth noting that the observed summed power spectral densities show significantly higher low-frequency content in the silicon preceding configuration, compared to the ceramic preceding configuration. Conversely, higher intensity is observed for the ceramic first case at frequencies around 1 THz.

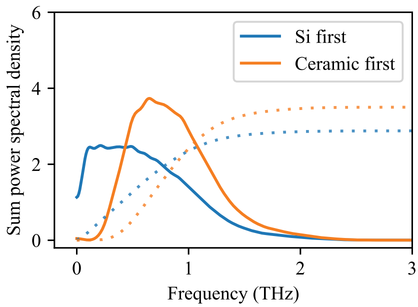

Fig. 82: The summed power spectral density of the two experimental cases. The dotted lines show the cumulative sum of the power spectral density.

To understand the apparent redistribution of power into lower frequencies, it is relevant to view the measured THz waveform in time with the same axial sampling method as fig. 81. This is shown in fig. 83, where time propagates along the y-axis, and the HOA is along the x-axis. The induced low frequency content is immediately observable for the low-angle part of the silicon preceding panel, compared with the ceramic first panel of the figure. The curvature of the diverging field is obvious in the ceramic first panel, and is consistent with emission from a point source.

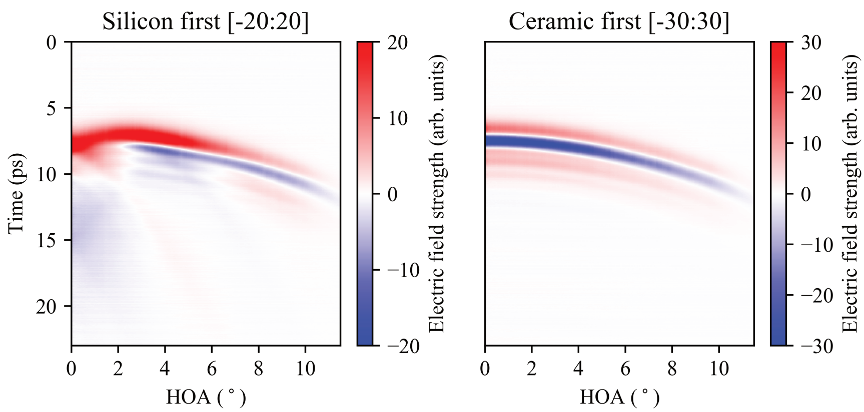

Fig. 83: The pulse propagation as a function of time and opening angle. The figures in the square brackets indicate the range of the data in the color scale.

It was investigated if the pump power of the ω light influenced the measured depression in the center. Fig. 84 show similar results for a pump power ranging from 0.25 mJ to 2 mJ. The SNR decays significantly for lower powers but the central depression was visible across the power ranges. The central depression was observable down to a ω pulse energy of 250 µJ. The silicon-ZnTe distance was very short in this case, leading to negligible diffraction around the central occlusion, and no central spot. A shift in opening angle was observed for the 500 µJ pulse energy, but the cause is unknown.

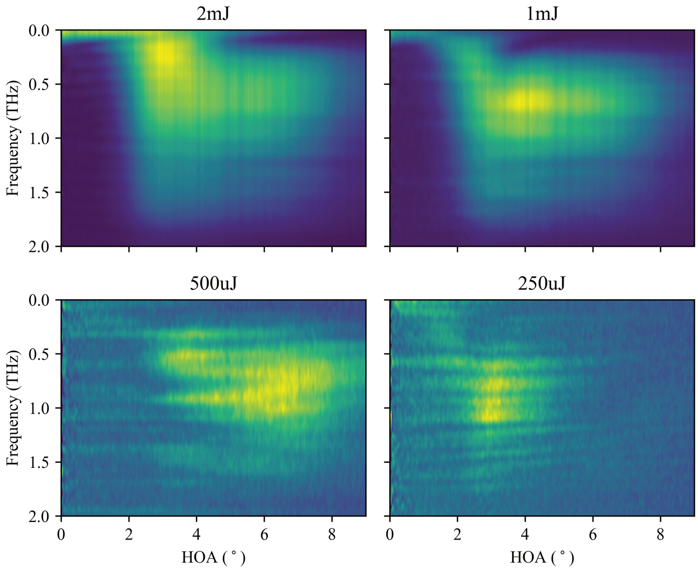

Fig. 84: Silicon first amplitude maps without normalization, for various input pulse energies. The SNR decays significantly at lower pulse energies.

The phase across a frequency slice is shown in fig. 85. Concentric circles are observed, leading to the conclusion that no topological charge is present in the THz beam.

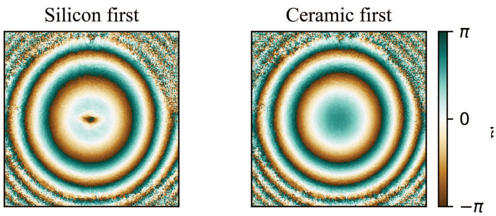

Fig. 85: The phase map at 1.5 THz is shown to support the secondary investigation of vorticity in the conical-like beams that are observed. The tendency is the similar across all frequencies (data not shown). The colormap ranges from π to $-\pi$ for brown and green respectively.

To characterize the terahertz emission angle as a function of frequency, Gaussian distributions have been fitted to the data for each frequency. The result is shown in fig. 86. It is observed that the HWHM of the THz radiation decreases with increasing frequency. The errorbars are a combination of the inverse of the signal-to-noise ratio and the standard deviation of the residuals. The inverse of the SNR is very low, and has been multiplied by an arbitrary weight of 50 to identify where the SNR is insufficient (above 2.5 THz). The standard deviation of the residuals are calculated from the residuals of a 6th order polynomial fit to the radial amplitude. The non-colinearity between the THz wavefront and the probe due to the assumed plasma point source has been taken into account, by weighting the data with $1/\cos(\mathrm{HOA})$.

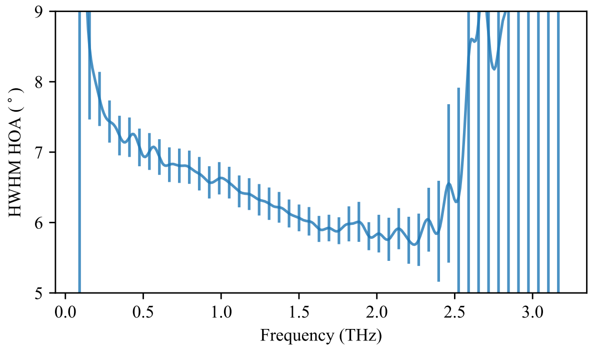

Fig. 86: The HWHM opening angle for the THz radiation shown in fig. 81, with the ceramic filter preceding. The vertical lines signify 1 standard deviation from the estimated HWHM. Note the steady decay with increasing frequency.

10.3 Diffraction around an opaque point

Hypothesis 3. *Diffraction can explain the low-frequency behaviour of the emission patterns measured by the 2D EOS setup.*

This subsection explores the claim regarding the diffractive nature of the low-frequency content of fig. 81. Assuming the existence of a central spot where the transmission of a silicon wafer is severely limited, it is straight-forward to approximate the diffraction pattern as a function of frequency. Further assumptions include a silicon pump beam with a gaussian cross-section, and that the central obstruction has soft edges, and an exterior diameter of 5.24

mm (calculated from a plasma center position to silicon filter distance of 50 mm, and a HOA of 3°).

10.3.1 Geometry of simulation

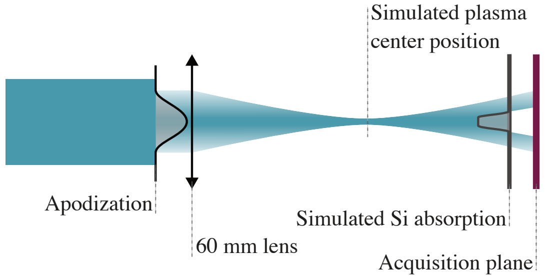

Fig. 87: Sketch of the geometry of the diffraction simulation. The distance between the lens and the silicon absorption plane is 110 mm, and the distance between the silicon and the acquisition plane is 10 mm.

The geometry of the simulation is shown in fig. 87. The diffraction and propagation was modelled using Lightpipes[97] with python. The source is a collimated beam at a specific THz frequency. To generate the assumed point-like source from the two-color plasma, the gaussian beam is focused by a thin lens with a focal length of 60 mm. This provides an opening angle and a HWHM that corresponds to the measurements from fig. 81. The light is propagated to the silicon plane, where the occlusion is introduced. The silicon plane is 50 mm from the imitated plasma source.

The model of the central occulter is a saturated spot, with expected soft edges. This is modeled by a simple flat-top, with a gaussian edge-shape. This model enables a fixed FWHM for the spot, regardless of the edge softness parameter. Fig. 88 show the influence the two parameters has on the model for the central spot occulter. The softness parameter is the FWHM parameter of the edge gaussian distribution (outlined with dashes). The light propagates further 10 mm, to the sampling plane, where the intensity is recorded.

The two parameters (FWHM and softness for the silicon occulter) are then manually tuned to provide a visual fit with the data from fig. 81. Fig. 89 show the near field propagation results for three different edge softnesses, and a fully transmitting Si filter. A good likeness to the data was found at a spot FWHM of 2.74 mm, and a softness of 1.5 mm. The Arago diffraction spot behind the silicon occlusion is visible, and very sharp for the hard-edged spot.

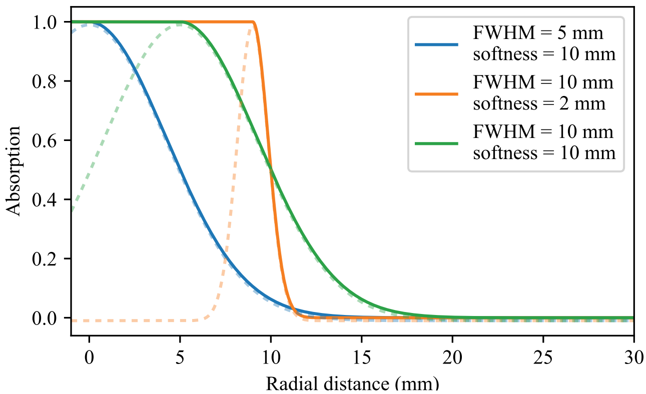

Fig. 88: Sketch of the radial model of the central occulter absorption. The parameters FWHM and softness define the shape. The softness parameter is the FWHM parameter of the edge gaussian distribution (outlined with dashes).

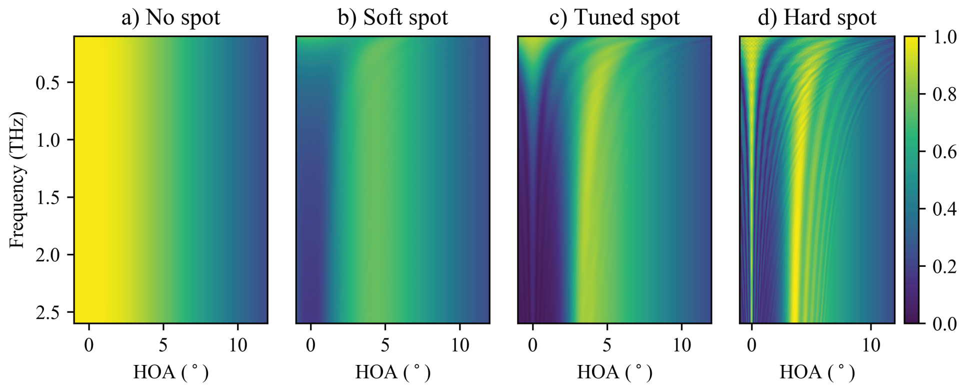

Fig. 89: Fresnel propagation simulation results for various geometries of center spot. All panes show the simulated amplitude distribution of THz radiation for the frequency spectrum. Panel a); No spot is introduced, model for preceding ceramic filter. Panel b); A gaussian spot (FWHM=2.74 mm) is simulated. No emergence of Fresnel bright spot. Panel c); visually tuned parameters for spot (FWHM=2.74 mm, softness=1.5 mm). Panel d); Simulation of results for a hard-edged spot (FWHM=2.74 mm, softness=0.01 mm).

10.4 Visible pump, THz probe imaging of silicon filters

Hypothesis 4. *A well-defined low power, single wavelength optical pump will generate charge carriers when irradiated onto the silicon filter.*

To verify whether a comparatively low power optical pump would generate the observed central depression in THz intensity, a secondary experiment was set up. 5% of the ω pump beam was picked off with a beamsplitter and attenuated to a pulse energy of 10 µJ with ND filters. The comparatively low power optical pump was then directed behind the ceramic filter, and irratiated the silicon filter. A delay line provided adjustable delay between the THz pulse from the plasma and the optical pump pulse. The setup is sketched in fig. 90.

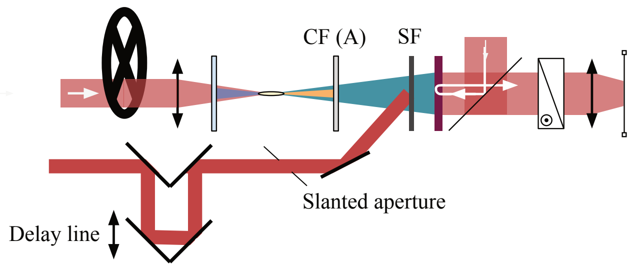

Fig. 90: By guiding a low power beam behind the ceramic filter and onto the silicon, charge carriers is expected to be generated. Identical 2D EOS acquisition geometry sample the THz electric field. A slanted aperture provides a round spot on the silicon filter even at oblique angles of incidence.

To provide a round beamshape on the silicon surface, a slanted aperture was applied. With an angle to the beam identical to the angle between the silicon and the beam, the aperture shape (round) was projected onto the silicon filter.

Fig. 91 show temporal slices for various delays between the THz pulse and the silicon pump pulse. The THz pulse is imaged at the same temporal instance in each image. Note the curtain effect, as the slanted wavefront excites charge carriers in the silicon when the optical pump pulse propagates across the filter. The excited charge carriers in the silicon negates transmission in the irradiated areas.

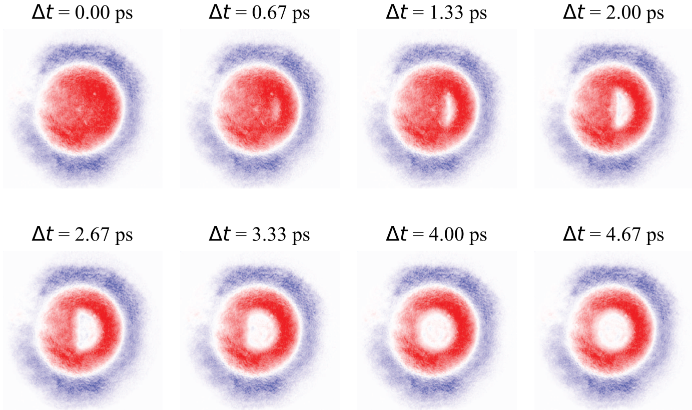

Fig. 91: Discrete temporal slices, showing the THz electric field, with a comparatively weak pump pulse isolated and led around the ceramic filter onto a silicon filter. The curtain effect is due to oblique incidence of the silicon pump beam. Reproduced from [78], manuscript in preparation.

10.5 Transmission properties of the used ceramic filter

Hypothesis 5. *The ceramic filter support transmission of broadband THz radiation.*

Time-domain spectroscopy has been performed on the ceramic filter, to characterize the transmission properties. A two-color plasma source was imaged with a 4-f configuration in the sample plane, where the ceramic filter was placed. The image of the sample plane was the focused in a GaP electro-optic crystal and the THz signal was measured with a balanced diode detection.

The data is shown in fig. 92. A refractive index of 3.05 was measured in the range of 0.4 THz to 2 THz, and an absorption of $5\,\mathrm{cm}^{-1}$ to $10\,\mathrm{cm}^{-1}$ with absorption increasing monotonously with frequency to $50\,\mathrm{cm}^{-1}$ at 3.5 THz. At frequencies below 0.4 THz, the SNR was low, so the large excursions here are attributed to noise.

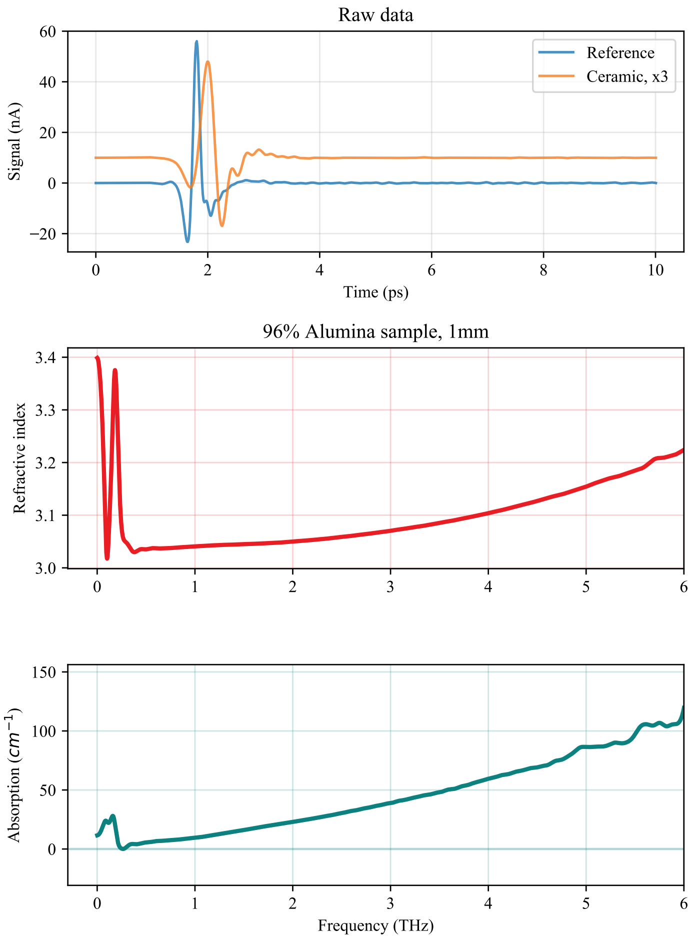

Fig. 92: Time-domain spectroscopy of the used ceramic filter. The large excursion below 0.4 THz is attributable to low SNR. Note that the temporal trace for the ceramic sample is multiplied by 3 in the plot.

11 Chapter summary

This chapter has primarily concerned itself with the emission characteristics of THz wavefronts from two-color plasma filaments. It was outlined initially that the previous literature shows a consensus towards a conical emission pattern from the plasma filament source, but disagree on other points.

The work by Zhong et al.[7] excel in being the only reference that did not implement a silicon as a filter to remove the high intensity forward-emitting waste light from the filament. Gorodetsky et al.[83] protects their silicon filter with a HDPE, but the geometry is not specified—it is the authors experience that significant distance between the filters is necessary to scatter the ω and 2ω beams. Ushakov et al.[81] indicate that they only use PTFE filters before the Golay cell, but they do not show clear conical emission profiles in their paper.

This work (published in part in [77] and in [78][manuscript in preparation]) argues that any conical emission was only due to a preceding silicon filter. If the order of the two filters were interchanged, to place the dielectric ceramic filter 10 mm before the silicon, no conical profiles were observed. This applied to both an incoherent setup as well as the coherent detection.

For the incoherent measurements it was shown that the conical emission did not occur with the ceramic filter first, regardless of numerical aperture. This is contrary to the conclusion by Gorodetsky et al.[83].

A simple model based on near field diffraction around an assumed central absorbing spot on the silicon was tuned to the amplitude distribution in fig. 81. The diffraction model relies on a parameterized model of the central occlusion, which in this work is defined as a combination of a flat top and the edge characteristics of a Gaussian distribution. This parameterized model has the drawback of being smooth in the transition between the flat top and the soft edge, where a sharp transition is expected towards a gaussian drop-off. The implemented model does however provide straight-forward control of the HWHM of the compound distribution.

Further, the diffractive model did not take the negative correlation between frequency and HWHM opening angle into account. Figure 86 show a decreasing opening angle of the emitted THz radiation with the ceramic filter preceding the silicon. At 0.25 THz the HWHM opening angle is 8.5°, while it decays to 6° at 2 THz. The emission angle is still significantly smaller than calculated from diffraction from a small aperture.

Unsurprisingly, the phase maps at a sample frequency of 1.5 THz did not show any topological charge in the beam. Neither did they show very fast spatial variations in the phase, as predicted by the You model[82].

The data analysis relies heavily on the assumption that all slices in time and frequency are symmetric around a pre-defined center point. Small changes in this center point may not influence the smooth characteristics for the ceramic-first configuration, but it may significantly attenuate the Arago peak for the silicon first case. This would lead to an underestimation of the softness parameter in the diffraction model fit.

The pump power was investigated and it was seen that the conical amplitude emission profiles were present from 250 µJ up to 2 mJ. This indicates that the sensitivity of the silicon filter is high. This was further motivated by the silicon pump-THz probe measurements performed with the oblique angle incidence. The experiment phenomenologically is enlightening, but it does not hold strong scientific value as it was performed only at 10 µJ silicon pump energies.

The bandwidth in the EO experiments is limited to 2.5 THz, due to two factors: Firstly, the ceramic filter absorbs significantly, and the absorption is positively correlated with frequency, as seen in fig. 92. Secondly, the retro-reflection in the relatively thick (1 mm) ZnTe filter means that the probe pulse is dispersed, and that the interaction length between the THz and the probe is long—this leads to higher response at low frequencies. The front-side reflection from the ZnTe crystal did however provide a large opening angle to be imaged directly.

Furthermore, the single-ended system was shown to give high-frequency artefacts due to the sine vs sine square response of the detection system. This was observed to be problematic with a GaP EO crystal and a sample rate of 4 µm/37.5 THz. It is however not assumed problematic for the low-frequency response in the ZnTe crystal, but the magnitude of the effect has not been calculated. From fig. 70 the difference in response in the relevant frequency range is insignificant.

The increased low-frequency response for the silicon-first configuration was qualified by the temporal response shown in fig. 83. A time-dependent diffraction model should be developed to fully understand the re-distribution of power from the high to the lower frequencies. It was observed from the integral of the frequency response that the ceramic first configuration did provide a higher power. This is consistent with the hypothesis of loss of transmission in a region of the silicon filter.

Part IV

Low cost fabrication of optical components

12 Introduction

This chapter describes the work performed on the feasibility of rapid manufacturing of transmissive and reflective optical elements for THz radiation. The work presented here is based on the poster "Rapid prototyping of optical elements in the THz domain"[98]. Supplementary details on the fabrication was made available online[99].

The motivation of the work comes from the prohibitively large price of off-axis parabolic mirrors (OAPMs), as they reach a significant size. For reference, Thorlabs' largest OAPM has a diameter of 76 mm, and a reflected focal length of 228 mm, while priced at 676€(as of September 2019). Due to the long wavelength of terahertz radiation, large diameter optics are relevant to avoid diffraction. Furthermore, flexibility in shape and geometry of THz optics is advantageous. The setup for characterizing the antennas in section 2.3 has benefited from longer focal lengths, while still providing a comparatively large numerical aperture. A strong driver for the geometry of the setup for characterizing the emission profile of THz in section 10, was the diffraction patterns that were visible when imaging with 2" optics.

In general additive manufacturing is a stimulating subject for THz optics. The long wavelength relaxes the geometrical constraints that are imposed on the optical elements. This enables new fabrication methods; here-amongst 3D printing and manual machining.

From the simplest perspective, two geometrical terms decide the optical performance of components: The surface roughness with high spatial frequency (typically grinding marks, scratches and surface roughness on the microscopic level), and the surface roughness with low spatial frequency components (typically geometric errors in the optical blank and gross errors in grinding/polishing). This simplified view allows different tools for experimental characterization of the two domains in surface roughness. The two terms are also known as finish and figure, respectively.

12.1 Previous work on additive manufacturing

The intersection between the two popular topics of additive manufacturing and THz optics has recently arisen. Recently, fabricated OAPMs were fabricated[100] using a stereolithographic (SLA) resin printer (Formlabs Form 2), printing a castable methacrylate mirror, and subsequently coated with gold in a DC magnetron sputter coater. They report a surface roughness of Ra=4 µm, concluding that this will support imaging at a frequency up to 560 GHz, and showing the mirrors focusing abilities at 530 GHz by imaging the focal point of a collimated THz laser beam onto a camera.

Futhermore, there has been a plethora of work regarding additive manufacturing of optical components, ranging from aspheric lenses[101], phase waveplates[102], waveguides[103]. Previous PhD theses have also been published on the subject([104, 105]). Exciting work has been done with optical computation engines, where pretrained neural networks has been demonstrated to identify handwritten digit recognition[106]. Varying the diameter of a pattern of holes in a flat dielectric surface has also been presented for lensing and phase control[107].

In contrast to the previously applied physical vapour deposition (PVD) methods, recent work has shown waveguides with electroless wet chemistry deposition of hollow copper waveguides in polycarbonate tubes[108]. Furthermore, electroless plating has been shown on 3D print relevant materials such as polylactic acid (PLA) and polyethylene terephtalate glycol (PETG)[109], as well as acrylonitrile butadiene styrene (ABS)[110].

12.2 Diffuse reflection from high spatial frequency components

The reflective scattering from flat surfaces with high spatial frequency contributions to the roughness may be modelled[111] as:

$$R_s = R_t \exp^{-\left(\frac{4\pi R_q \cos\theta}{\lambda}\right)^2} \tag{23}$$

Where R_s is the scattered diffuse reflectance, R_t is the intrinsic total reflectance due to the material, R_q is the RMS surface roughness, θ is the angle of incidence from normal and λ is the wavelength.

Note that while previous literature discusses the RMS roughness (R_q), the present day standard is the R_a - the arithmetic mean deviation from the anticipated profile. Generally, the conversion from R_a to R_q implies adding 10%.

The term total indicated scattering loss (TIS) was defined by[112], as

$$TIS = \frac{\text{diffuse reflection}}{\text{total reflection}} = \frac{R_s}{R_t} = \exp^{-\left(\frac{4\pi R_q \cos\theta}{\lambda}\right)^2} \tag{24}$$

This expression allows a designer of optical elements to specify the tolerances of the surface roughness, by defining the greatest loss due to diffuse reflection allowable in the specific instance.

By specifying e.g. 1% maximum allowable loss (TIS), the limit to the surface roughness may be calculated. Conversely, various fabrication methods may be compared. Fig. 93 shows the scattering losses from perfect electric conductor surfaces ($R_t = 1$), fabricated by conventional turning (Ra = 1.6 µm[113]), as well as additive manufacturing with Fused Deposition Modelling (FDM) 3D printers (Ra = 9 µm to 35 µm[114]), and polished PLA polymer (Ra = 0.2 µm, measured). The angle of incidence is 45°.

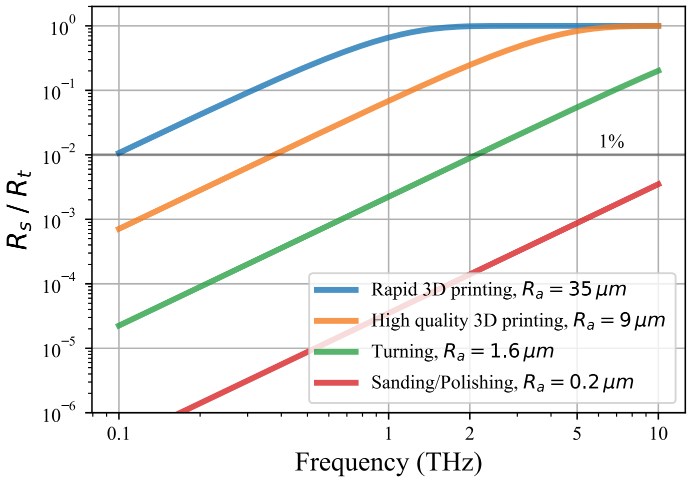

Fig. 93: TIS as a function of frequency, for a selection of fabrication methods. A perfect reflecting material and 45° incidence is assumed. A 1% loss tolerance line is included as a dense grey line. Adapted from[98] with permission.

In fig. 93, a 1% loss tolerance line is included, indicating that as-turned metal stock will support up to 2 THz, while significant scattering is expected when reflecting off of as-printed parts made with FDM technology. Polishing of as-printed material has been shown to decrease the surface roughness to sub-micron levels, supporting radiation of above 10 THz in frequency.

13 Additive manufacturing of off-axis parabolic mirrors

This section describes the developed procedure to manufacture curved surfaces for reflective optics. Specifically, OAPMs are used as a relevant case. This is an example of fabrication driven design, and thus the fabrication procedure is discussed first.

The first step is the design; a solid 3D model is drawn in a relevant Computer Aided Design (CAD)-package and exported as a .stl file. This file is imported in a 'slicer' software, that generates machine code for the 3D printer. This machine code is 'G-code' and contains a low-level description of the motion of the 3D printer. This allows the computationally heavy calculation of tool trajectories to be spared from the micro-controller that provides the critical timing of the motion.

The physical workflow is (very briefly): The 3D model is printed, and has its support structure removed, edges cleaned, optically relevant surfaces polished and cleaned, and finally the metallisation is performed in a sputter coater. Further details is described below, but a general overview is helpful.

The additive manufacturing (i.e. 3D printing) technique used here was Fused Filament Fabrication (FFF). A thermoplastic polymer is extruded through a numerically controlled heated nozzle. By controlling the extrusion rate and the position of the nozzle, a solid 3D model can be build in layers. The model was (in experience) generally accurate within 0.2 mm, and has optically coarse features.

The model is extruded with the tool moving in the horizontal plane along the X and Y coordinates. When a layer has been fully printed, the vertical Z-axis moves a discrete distance to allow the tool to extrude a new layer on top. This repeats until the entire model is created. To achieve better control of the exterior geometry, the interior is not entirely filled. Instead, a parameter called 'infill' is used to describe the volume percentage of the central part that is extruded thermoplastic. Figure 94 shows the infill lines in orange.

The shell of a model has a wall thickness which is defined through the line width and the number of interior lines from the exterior perimeter. The exterior is shown in red in fig. 94, while the interior wall lines is shown in green. The subsequent polishing step requires a significant wall thickness, so this parameter must be changed from the default setting.

It must also be noted that the printer is controlled with stepper motors, which provide only discrete positions. Due to a technique called 'microstepping' and the intrinsic resolution of the stepper motors, the theoretical lower bound on the horizontal plane resolution is 11 µm. The system is purely open-loop control, so any slips or errors from the motor controller and out is not corrected.

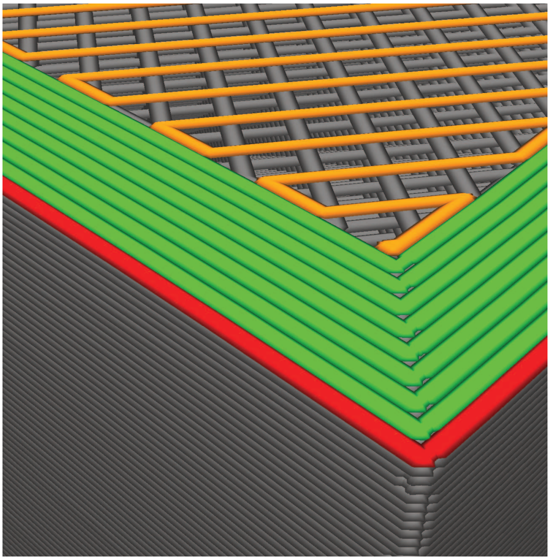

Fig. 94: Example from the slicer software. Orange is the infill, green is the shell thickness build-up lines and red is the exterior line. The image was taken from the Cura slicer software, with a perspective viewport, at 20% infill. The lower grey layers are the preceding layers in the stack.

13.1 Guidelines for settings and model orientation

Ultimaker Cura was the slicer software that was used to generate the G-code. It presents the user with more than 100 different parameters, not including the position and orientation of the model. No attempt was made to exhaustively optimize the print parameters, but the settings in tab. 4 was found adequate.

The orientation of the model has been found critical. It is a tradeoff between two factors: To minimize printing time and maximize the in-plane stiffness during printing, the optimal orientation would be with the optically relevant surface on top, printing as large an area as possible per layer.

However, the discrete approximation of the true surface is done with three distinct strategies, shown in fig. 95. The exclusive strategy will provide an exterior point contact to the true surface, and is not suitable for abrasive post-processing. It could be suitable for coating with e.g. a low surface tension liquid resin. The middle approximation would generally keep the volume true to the original object, but does not limit the material removal rate near the true surface.

The inclusive strategy for approximation is chosen due to the behaviour of the polishing step. If the material volume removal rate is considered constant for wet polishing, the material depth removal rate will decrease towards the true surface, and finally remain constant on a global scale when this is

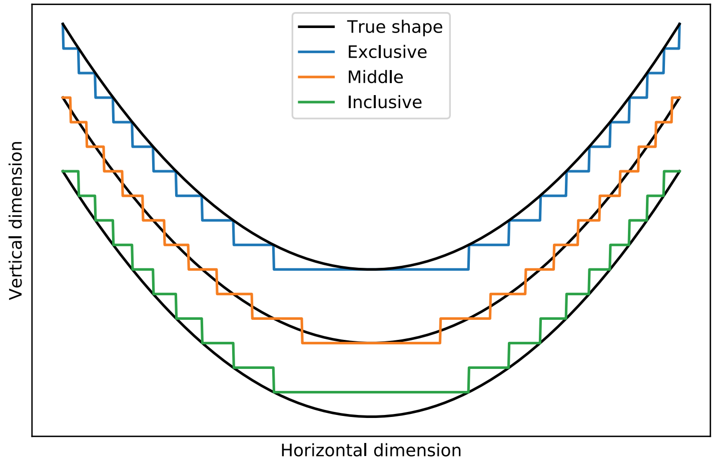

Fig. 95: Slicer strategies. The discretization of the vertical layers allow for three distinct strategies in approximation of the true surface. The interior of the surface is below the black lines, while the exterior of the surface is above.

reached.

This motivates the inclusive strategy for the curved surfaces, but the choice is detrimental at any points in the model that are parallel to the discretization plane. Here, an error is observed in fig. 95 where the error-volume is locally large. Experience has shown that this is very difficult to remove, as the sanding predominantly attacks on edges. With no edge to start from, polishing must be done with a geometrical control that is inhibiting.

To remove the occurence of plane-parallel surfaces (and hence large error volumes), the model of the mirror is always positioned to have optically relevant surfaces greater than 40° off the horizontal plane. Furthermore to improve the discretization of the in-plane motion, the model is also oriented at 45° from X and Y. Figure 96 shows the suggested and used orientation of printing.

The free choice of geometry allows helpful structures for e.g. alignment. Fig. 96 also show grooves on the perimeter of the mirror for alignment. The two grooves indicate the two normal directions for the OAPM, allowing very easy and accurate coarse alignment of the mirrors. A metal ruler extends the direction of the triangular groove very accurately, and the effective focal length is defined from the normal groove. The triangular groove allows mounting and alignment of mirrors within 1 mm from optimal, with no other aids than a ruler in minutes.

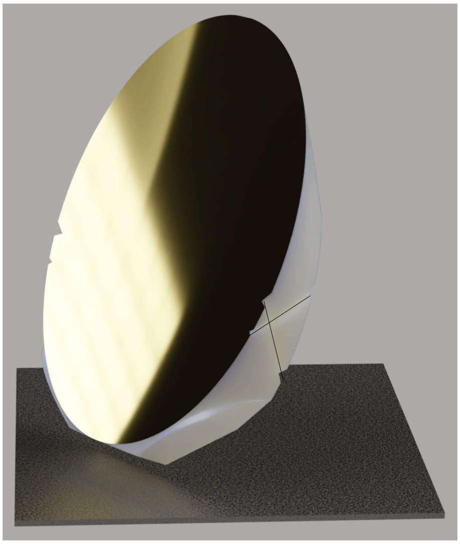

Fig. 96: Suggested model orientation in the pre-processing and printing, to minimize discretization errors after polishing. The grey floor signifies the buildplate in the horizontal plane.

Parameter	Value
Infill	20%
Wall thickness	2 mm
Vertical layer height	20 µm
Nozzle diameter	400 µm
Print speed	$100\,\mathrm{mm\,s^{-1}}$
Material	Only PLA max has been tested.
Slicer strategy	Inclusive, to improve intrinsic polish-stop at correct geometry.

Table 4: Suggested parameters for 3D printing of mirrors.

13.2 Polishing and coating

The primary novelty of the fabrication was the transition from an as-printed mirror blank to a mirror functional in the THz range: The polishing was performed by hand, without any polishing jigs. Struers silicon carbide abrasive paper was used, with a grit starting at #320, going to #4000. The abrasive paper was used wet, with a less than 1% detergent solution. The grinding procedure initially abrades the layer structure away, and subsequently polished the grinding marks off. Grit #320 left the surface with a dull surface, suitable for 3D scanning, while the subsequent polishing steps was assumed to remove little material. The detergent helped the large surface tension of the plastic, especially as the surface became smoother. Care was taken to abrade evenly on the entire surface.

After thorough rinsing with water, ethanol and IPA, the mirror blanks were blow dried with N_2, and mounted in a 6 inch DC magnetron sputter coater. 100 nm titanium and 300 nm gold was deposited. The DC power was 400 W, and no problems with excessive heating of the mirror blanks were observed. The mirrors were ready immediately after, but they were mounted in a 3D printed jig that interfaced the Ø100 mm OAPM with standard 1 inch optical mirror mounts. The fabricated OAPMs were low weight, and were reliably held in a standard optical mount.

14 Qualification of method

To qualify the method with respect to the requirements set in section 12, two measurements have been performed; profilometry of the surface shows the local surface roughness, while a 3D scan of the surface and a subsequent fit of the point cloud indicates the induced wavefront error. The results of this analysis was presented as a poster at the IRMMWTHz meeting in Paris[115].

14.1 Profilometry of polished surface

A profilometer (Ambios XP2) was used to characterize the high frequency components of the surface roughness. With a range of 400 µm and a vertical resolution of 15 Å, it can accurately gauge the surface topology in accordance with industry standard surface roughness measurements. The spatial frequency of the measurement is 250 nm on a sample length of 10 mm. See fig. 97 and fig. 98 for the data and roughness spectral density, respectively.

The curvature is subtracted from the raw data, by a 5th order polynomial fit. From this, the mean arithmetic deviation (Ra) is calculated and shown in table 5. The spatial frequency content is also calculated, and shown in figure 98. Note that the density of wavelengths is scaled by the inverse wavelength, to show a horizontal line. This is the cause of the inverse distance on the y-axis unit.

Element	Surface Roughness (Ra)
Lens	2.3 µm
Mirror	120 nm

Table 5: The surface roughness of the finished optical elements.

Essentially three domains are seen in the data from both the lens and the mirror; the low-wavelength region (0.5 µm to 1 µm) is not relevant as the frequency is much too high to scatter THz radiation.

The mid-range, from a characteristic wavelength of 2 µm to 200 µm is relevant as this scatters THz radiation. It is also where the majority of the signal

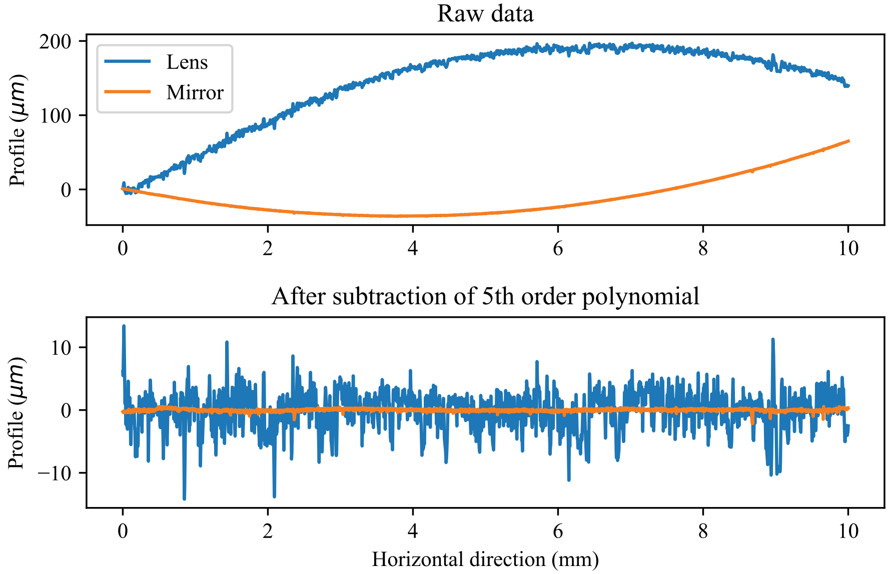

Fig. 97: The raw profilometry data and the result after baseline/curvature subtraction.

excursion lies. Finally, the long-wavelength range contains the curvature of the optical elements.

Note that the arithmetic surface roughness is a global amplitude parameter, and can not be identified in figure 98.

14.2 Error from true surface

To qualify the imaging properties (figure properties) of the fabricated mirror a 3D scan was performed using a linear laser scanner(wenglor sensoric GmbH MLWL131) mounted on a 6 axis robot(Kuka KR60). See figure 99. The laser scan head continuously sampled a linear profile along the line direction, while the robot scanned across the mirror blank (the scan direction). A point cloud was generated with 8M points in 3D for the curved surface.

Note the definition of direction; horizontal is assumed to be the plane that is spanned by the line direction and the scan direction. These are indicated in fig. 100. The vertical direction is normal hereto and pointing upwards away from the surface.

14.2.1 Calibrating to a flat plane

As the accuracy of the laser line scanner was only well defined within a line, the overall accuracy relied on the accuracy of the robot in the motion of the

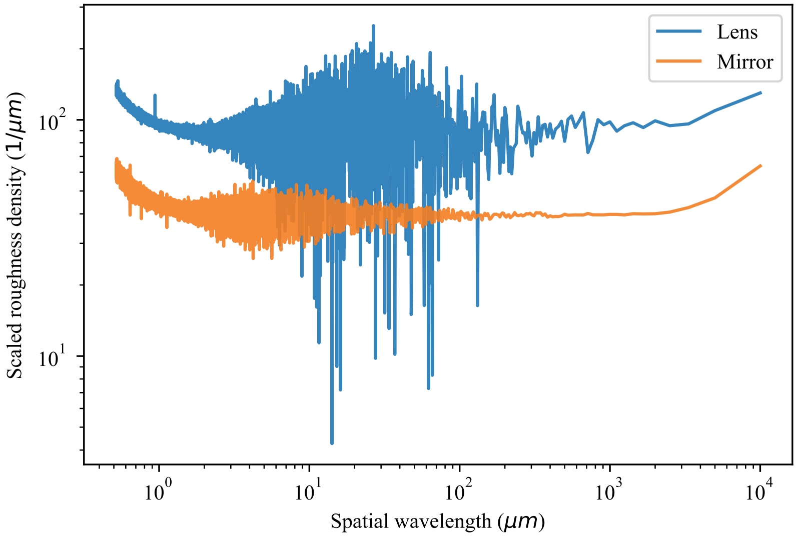

Fig. 98: The distribution of the characteristic roughness wavelengths show three significant domains for both the lens and the mirror; The short wavelength domain (below 2 µm) is not optically active for THz. The majority of the surface roughness lies in the mid-range(2 µm to 200 µm) and the curvature domain is in the order of millimeters.

end effector. The accuracy of the line scanner was quoted as 26 µm in the horizontal X direction, and a linearity deviation along Z of 15 µm.

To allow for this error in movement, a reference scan was performed with a metrologically flat granite surface (class B, Ra<1.63 µm, flatness<5 µm[116]). The deviations outside of the specified tolerances was atributable to the measurement apparatus and specified the error range.

The raw data of a scan is shown in fig. 101 a), where distinct variations are seen along the scan direction. Figure 101 b) shows the mean along the line direction (collapsing the 2D plot of fig. 101 a) to a 1D array along the horizontal axis of the plot), flanked by $\pm\sigma$, the standard deviation.

Note that the standard deviation is relatively small compared to the signal strength. The dominant factor in the mean scan line noise is the imperfect motion of the robot end effector.

After subtracting the mean variation along the scan line, the color map of fig. 102 a) is shown. Note the vertical scale which is less than half of fig. 101 a), and the appearance of striations along the line direction. These lines represent imperfections in the laser line scanner. The mean error from a perfect plane across the scan direction is shown in fig. 102 b) - note the significantly higher standard deviation compared to the error amplitude. This standard deviation represents the error noise in the measured surface geometry, and

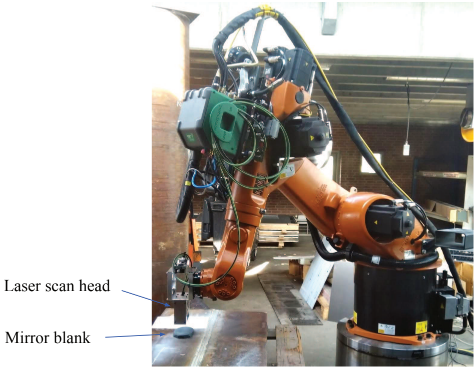

Fig. 99: The setup for 3D laser scanning of mirror blanks

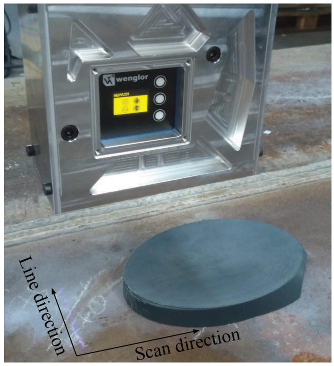

Fig. 100: The definitions of line direction and scan direction.

is around 5 µm, thus near the tolerance of the flat plane used for calibration. For the measurement of the mirror, the mean across scan direction may also be subtracted.

It should be noted, that the data has no predisposed orientation, as well as the motion of the robot end effector is also only visually approximated to the plane. Numerical optimisation of the rotation vectors around the two horizontal directions and a vertical displacement is performed to find the best fit to a plane. The cost function to be minimized was the RMS of the difference between the vertical coordinates of the data and the vertical coordinates of the sampled parabolic target function.

14.2.2 Point cloud fit to theoretical surface

Numerical optimization was performed for the scan of the curved surface. As the function definition (the theoretical surface) was oriented at roughly 45° from the horizontal plane and the scanned model was approximately parallel, a rotation had to be provided. The algorithm that wass used in the orientation was as follows:

-1. Subtract the mean across scan direction, shown in fig. 101 b).

0. Pre-transform the data to provide a robust and approximate initial guess. This is done visually and iteratively.

1. Displace the point cloud some distance in the scan direction.

2. Displace the point cloud some distance in the line direction.

3. Displace the point cloud some distance vertically.

4. Perform Euler rotation[117] with test angles α, β and γ.

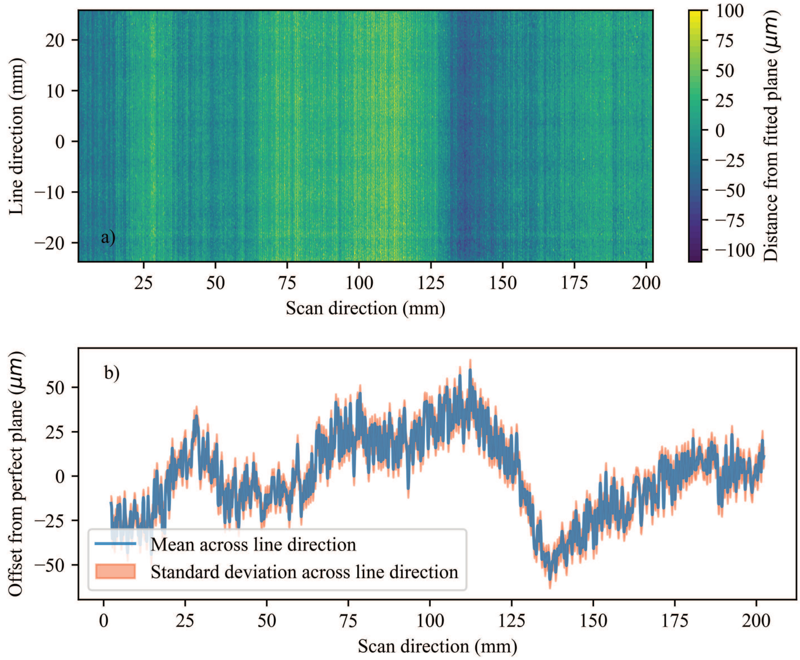

Fig. 101: a) shows the raw data of the flat plane scan, where variations are clearly visible along the scan direction. Some indistinct features can be seen along the line direction as well. b) shows the proportionally small standard deviation of the scan line excursions compared to the mean.

5. Sample the theoretical function with the displaced and rotated scan and line coordinates, to generate a test surface. If the rotation was optimal, the scan, line and vertical values will be identical.

6. The cost is calculated as the RMS of the 3-space vector distance between the sets of points.

7. Step 1-6 is repeated to minimize the RMS of the vector distances between the sampled function and the measurement.

8. The point cloud is now oriented approximately at 45° from the horizontal plane, in line with the parabolic surface. To find the normal displacement from the theoretical surface, the measured point cloud is manually transformed back onto the horizontal plane, along with a sampled point cloud.

9. Now, the error between the measured point cloud and the sampled point cloud may be evaluated along the vertical direction, and plotted.

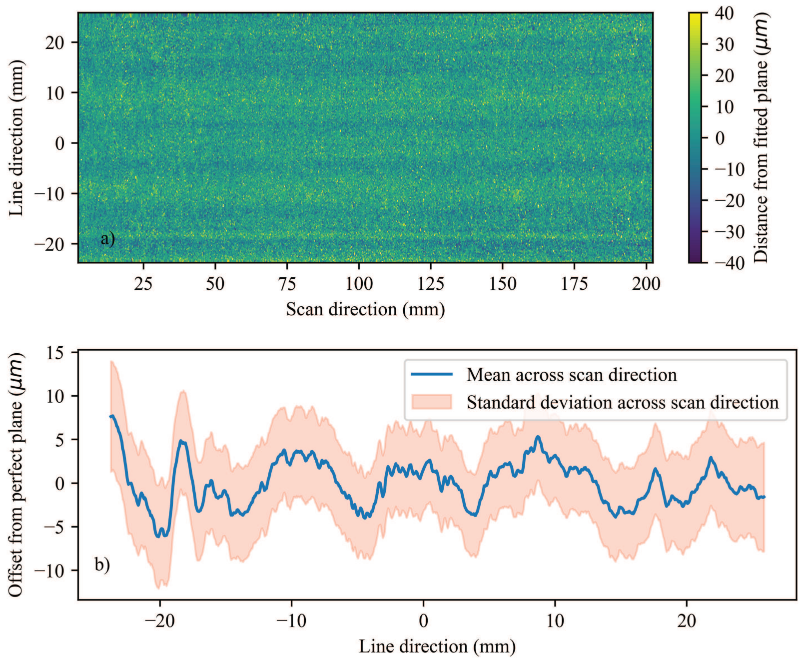

Fig. 102: a) The deviation from a flat plane after subtraction of the mean scan direction excursions. The subtraction attenuated the scan direction error to clearly show the line direction error. b) shows the measured mean offset between the corrected data and a flat plane.

A minimum is reached using the Python implementation of a Nelder-Mead approach, in `scipy.optimize.minimize`. The result of the error between the measured point cloud and the point cloud sampled on the function is shown in fig. 103. It is plotted in units of fractional wavelengths at 1 THz, 300 μm, similar to specifications given by manufacturers of conventional, machined OAPMs.

As can be seen from fig. 103, the significant part of the mirror is within $\lambda/2$. The lower bound of the measurement accuracy is assumed to be 10 μm, or $1/30\lambda$. It is noted that care must be taken in polishing as this might have been the cause of the excessive material removal near scan direction positions 40 μm to 100 μm. The significant striations that are visible in the plot may stem from the difference in measurement height between the flat calibration plane and the mirror, as the latter is only about 1/4 the thickness. The measurement plane for the calibration is thus slightly different. It must be noted that while the exact measure of deviation from the theoretical surface should be gauged along the normal of the mirror surface, the result in fig. 103 approximates this, by only gauging the vertical deviation from the theoretical surface.

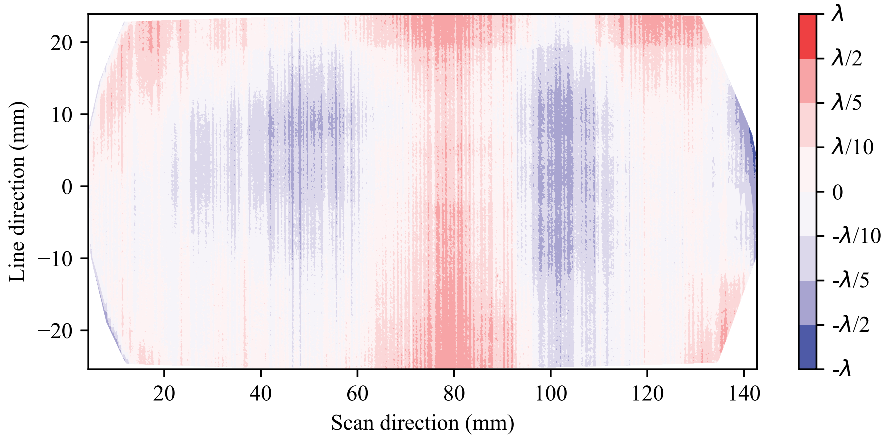

Fig. 103: The deviation from the theoretical surface in units of wavelengths at 1 THz (300 µm).

15 Manual machining of spherical lenses in polymers

Disclaimer 1. *This section is provided as a reference; the technique belongs to the toolbox of machining tradesmen, going hundreds of years back. The author claims no part in the ideas conception, but it is provided as a useful reminder for the THz community.*

Modern technology has enabled computer numerical controlled (CNC) lathes and mills to fabricate parts in polymers with only little cost, and high performance for THz optics[118]. However, if such machines are not available, spherical surfaces should not be outside consideration.

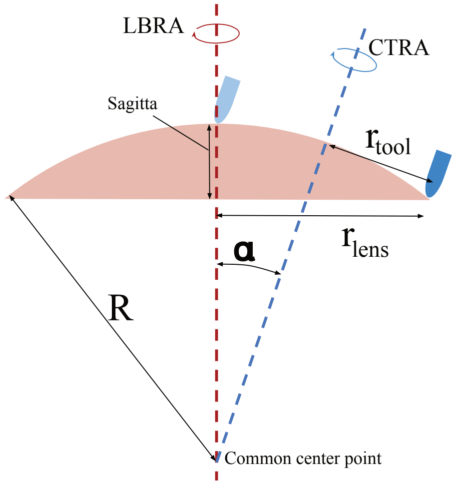

Fig. 104: Sketch of the cutter geometry. The lens blank rotation axis (LBRA, red dashed line) and the cutting tool rotation axis (CTRA, blue dashed line) is sketched, with the angle α between them. This angle and the cutting tool radius r_{tool} define the spherical surface. R is the radius of curvature for the fabricated lens. The lens is rotated around the lens blank rotation axis with a comparatively low rotational speed, while high rotational speed is imposed on the tool. Adapted from[98] with permission.

The spherical surface can be manufactured by using a large-diameter single point milling tool (fly-cutter), with an axis of rotation (cutting tool rotation axis, CTRA) that is not colinear with the axis of rotation of the lens blank (lens blank rotation axis, LBRA). By rotating the lens blank continously while feeding slowly towards the cutter, the lens will form. See fig. 104 for the schematic drawing at the situation near the operation finish.

The simple plano-convex lens is designed through the lensmakers equation:

$$\frac{1}{f} \approx (n-1)\left[\frac{1}{R_1} - \frac{1}{R_2}\right] \tag{25}$$

where f is the focal length, n is the refractive index of the lens medium, R_1 is the radius of curvature of the first surface, and R_2 is the radius of curvature of the second surface. Note that for the plano-convex lens we set the fraction $1/R_{1,2}$ to be 0. Another assumption is that the lens is in a medium of refractive index very close to 1.

With the relevant radius of curvature (R_{lens}) specified, the machining geometry may be calculated. The tool rotation angle is specified by the sagitta (the dimension of the thickest part of the plano-spherical lens) and the chord length (the diameter of the plano-spherical lens) of the desired lens. The relation between the sagitta, the chord and the radius of curvature is given by:

$$R_{lens}^2 = 2r_{lens}^2 + (R_{lens} - s_{lens})^2 \tag{26}$$

Where s_{lens} is the sagitta or the maximum lens thickness.

The cutting tool rotation radius r_{tool} is given by the length of the hypothenuse in the sagitta calculation, and the derived equations are as follows:

$$r_{tool} = \frac{\sqrt{r_{lens}^2 + s_{lens}^2}}{2} \tag{27}$$

$$\alpha = \tan^{-1}\left(\frac{r_{lens}/2}{R_{lens} - s_{lens}/2}\right) \tag{28}$$

where the sagitta $s_{lens} = R_{lens} - \sqrt{R_{lens}^2 - 2r_{lens}^2}$, calculated from eq. 26.

Holding the part on the rotation head can be done with cyano-acrylate (CA) glue. A slab of e.g. aluminium is bolted onto the rotation head, and it is milled flat. CA glue is applied in several spots on the surface. Then, the flat face of a lens blank may be glued on top, while ensuring that the blank is concentric with the rotation axis. Ensure also that there is a significant overhang from the mounting surface in one position along the edge. After machining the brittle CA glue bond can be broken by percussive excitation from below, onto the overhang. Access for the percussive tool could also be provided at the center. Remaining spots of CA glue can be dissolved with acetone.

By using a sharp, positive rake cutting insert with a small nose radius, the material removal rate can be high, and a lens blank may be formed in a few minutes. Exchanging to a tool with a large nose radius will improve the surface finish. Cooling can be done with ethanol, to improve surface finish.

With the macro-geometry shaped, polishing can also be performed by hand, to achieve a sufficiently low surface roughness.

The surface roughness has been measured with a profilometer, and when subtracting a 5th order polynomial background, the surface roughness is $R_a = 2.28\,\mu\mathrm{m}$.

16 Chapter summary

The work presented in the preceding chapter concerned itself with rapid and cost-efficient fabrication of transmitting and reflecting optics for the THz domain. For reference, an ancient method for fabricating plano-spherical lenses was re-iterated, and the surface roughness was documented. The method is well suited for fabrication of large-aperture optics, as it is limited only by the reach of the used single point cutter and the available stock. CNC turning is another relevant method that has not been discussed - aspheric lenses[118] and arbitrary rotationally symmetric elements were previously shown.

Furthermore, a novel, straight-forward method of fabricating large-aperture reflective optics was shown; by hand-polishing a mirror blank fabricated with the FFF 3D printing technology, smooth surfaces may be fabricated with arbitrary curvature.

As a relevant use case, the fabrication of large-diameter off-axis parabolic mirrors were documented. A simple perspective on optical reflection was assumed, showing that both the surface roughness and the surface geometry (finish and figure, respectively) were sufficient to support frequencies of up to a few THz. The figure may be improved with practice, and the measured surface roughness of 120 nm will support radiation of more than 10 THz.

The figure may also be improved by using a hard and brittle spray-on primer, that will both fill the voids between the layers and be polished easily. Note that the slicing strategy should change from "inclusive" presently used, to "exclusive". This change would likely also improve the discretization error in local minima.

Chemical smoothing is also a relevant option; by replacing the polymer with e.g. ABS (Acrylonitrile butadiene styrene), acetone may be used in a technique called vapor-smoothing. The outer-most layer of the polymer is softened sufficiently to allow it to flow. The surface tension causes the polymer to flow to a smoother state. It is inherently isotropic, so further testing is necessary to ensure the figure remains useful. More elaborately, by mounting several mirror blanks in a centrifuge rotating at the corresponding rate, the centripetal acceleration will smooth a layer of e.g. photo-resist or another viscous polymer solution with a volatile solvent to the parabolic curve necessary.

While methods for improving figure has some research relevance, the most prohibitive in terms of availability and cost is the metallization. Sputtering of the metal layer requires low outgassing postprocessed mirror blanks (by experience a non-issue), access to clean room tools with high tolerance for odd substrates and the financial cost of deposition of very pure noble metals. It is relevant to replace the PVD step with an electroless plating step.

Part V

Conclusion and outlook

17 Overall conclusion

The primary goal of this thesis was to experimentally show the potential for improvement of terahertz emitter characteristics. This was sought for by two complementary techniques; implementation of emitters in an array, and addition of deep-etched substrate lenses.

The emitter array-effect was shown to approximately double the electric field from the emitter. While this was significant, the expected 25 times increase in electric field from the linear model was not realized. This is presumably due to the mismatch between the emitter extent and detector active area.

The effect from the substrate lenses was also drastic; leading to a 10 dB increase in dynamic range at 0.5 THz and an overall 100% gain in power spectral density from 0.4 THz to 0.75 THz. The maximum improvement going from a single emitter on a bare substrate to an array emitter with substrate lenses is 1290%.

The optimal antenna design was not identified as reproducibility issues were severe in the introductory experiments. Subsequent, simpler fabrication procedures have shown some improvements in reproducibility of antenna performance metrics. The limitations of the work was likely set by the utilized substrate material. The semi-insulating gallium arsenide substrates presumably set the limits for the bandwidth and emission efficiency with the long carrier lifetimes. Furthermore, a scaling error in the outset of the project motivated a silicon-dioxide isolation spacer in the fabrication procedure. This has subsequently been deemed unneccessary.

The context of remote sensing requires a high signal to noise ratio and good directivity, and the implemented techniques are offered as solutions. Furthermore, the arrays and substrate lenses are likely to be a key enabling technology in scaling of terahertz emitters for mobile, light weight, power-limited systems. The potential for full wafer-scale fabrication of emitters and detectors is motivated, and the substrate lenses integrates the last of the gross-geometry elements in a continuous wave terahertz system.

Secondly, work has been done to characterize the spatial emission profile of terahertz radiation from two-color plasma filaments. A Gaussian spatial profile was observed when protecting the silicon filter with a ceramic filter. A conical emission profile was observed when the forward propagating broadband light from the plasma filament was permitted to irradiate the silicon filter. The measurements agreed for both frequency-specific 2-dimensional electro-optic sampling in a zinc-telluride crystal and incoherent thermal measurements of power with a Golay cell detector. A preliminary overview of contemporary literature concluding a conical emission profile, showed a general consensus on the use of the silicon filter. It was shown that the frequency-dependence of the radial intensity distribution corresponds to the diffraction pattern in the plane of the silicon filter.

Contrary to previous literature, it is concluded that the emission profile for two-color plasma filaments is Gaussian in the frequency span of 0.2 THz to 2.5 THz. Any conical emission observed in this work has been the result of photo-excited charge carriers in the silicon filter. The implications in the robustness of results for non-linear terahertz spectroscopy is significant, as it is no longer necessary to assume a complicated development of the focus point. For now, if the bandwidth is required, a simple near field diffraction model has shown reliable prediction power on the intensity distributions, as a function of frequency.

The ceramic alumina filter is suggested as a terahertz compatible, ablation-resistant, and fully dielectric filter for scattering visible and near-infrared radiation from the filament. When used in combination with a silicon filter, it allows a high confidence in a well known Gaussian beam geometry.

While the absorption in the ceramic filter is tolerable below 2 terahertz, further work in development of strongly visible/near-infrared scattering filters is necessary to apply the possibilities for high-bandwidth spectroscopy techniques.

Finally, the author has provided techniques and suggestions for accessible, bespoke reflective optics for terahertz radiation. It was shown that mirrors may be fabricated using low cost fused filament fabrication additive manufacturing techniques. Subsequent manual polishing of the mirror blanks was shown to retain a figure that supported radiation up to a few terahertz and a finish that supported up to 10 terahertz.

The technique opens up possibilities of bespoke free-form reflective optics at little monetary cost. It was shown that the free choice of geometry may allow features to greatly assist alignment of the fabricated off-axis parabolic mirrors. The post-processing procedure limits the geometry to smooth surfaces, with or without curvature.

18 Future work

While positive results have been achieved in increasing the output electric field from arrayed terahertz emitters, there is still significant work to do to unlock the full potential. First and foremost, the antennas should be fabricated on a more suitable substrate. A shorter carrier lifetime will allow antenna characterization on a wider bandwidth and with higher output power. It is also interesting to further scale the array, and 9 by 9 arrays of emitters with slanted feedlines have been designed although not fabricated. Further characterization of the emitters is very relevant. The array excitation should provide significantly different emission patterns and this has not been investigated.

To cross-validate the detector which has been used in this work, it is relevant to apply the electro-optic sampling principle. Planned investments in research infrastructure will include an incoherent camera detector, which should allow imaging of the emission patterns, and validation of the array factor that is achieved. This would also result in very few limitations of the detector area.

A multilayer substrate — consisting of a regular silicon carrier wafer and a thin, short lifetime material on top — would provide the mentioned integration. Antennas would be fabricated on the frontside, while backside alignment of the substrate lens mask would easily provide alignment accuracies towards 0.5 µm.

Other array configurations are relevant to test as well. The higher bandwidth would require a smaller pitch of the antennas to suppress grating lobes. Pseudo-random positioning of array elements would also help to suppress the grating lobes, while retaining a forward directivity.

The work with high-intensity plasma sources has indicated a new potential for further characterization and modelling of the emission profiles from filaments. There is also a clear motivation for work on ceramic filters compatible with high-frequency terahertz radiation. The ceramic structure is efficient at scattering the visible and near-infrared radiation, while still having grain sizes significantly smaller than the terahertz wavelength. Obvious candidates for future work include porous ceramic filters as well as testing with different purities.

Rapid prototyping of optical elements still retain one hurdle towards true public accessibility; the metallization. While a physical vapor deposition tool is available at many universities, the more elegant solution would be electroless plating of the mirror blank. Weakly conductive filaments or thick film coatings may also be sufficient to support electrodeposition of e.g. copper.

Bibliography

[1] M. Brincker, P. Karlsen, E. Skovsen, and T. Søndergaard, "Microstructured gradient-index lenses for THz photoconductive antennas", AIP Advances **6**, 025015 (2016).

[2] J. F. Federici, B. Schulkin, F. Huang, D. Gary, R. Barat, F. Oliveira, and D. Zimdars, "THz imaging and sensing for security applications—explosives, weapons and drugs", Semiconductor Science and Technology **20**, S266–S280 (2005).

[3] M. C. Kemp, P. F. Taday, B. E. Cole, J. A. Cluff, A. J. Fitzgerald, and W. R. Tribe, "Security applications of terahertz technology", in , edited by R. J. Hwu and D. L. Woolard (Aug. 1, 2003), p. 44.

[4] J. E. Bjarnason, T. L. J. Chan, A. W. M. Lee, M. A. Celis, and E. R. Brown, "Millimeter-wave, terahertz, and mid-infrared transmission through common clothing", Applied Physics Letters **85**, 519–521 (2004).

[5] J. L. Jia Liu, W. F. Wenhui Fan, and B. X. Bing Xue, "Study on the transmission characteristic of terahertz pulse through packing materials", Chinese Optics Letters **9**, s10202–310203 (2011).

[6] J. F. Federici, D. Gary, R. Barat, and D. Zimdars, "THz standoff detection and imaging of explosives and weapons", in Defense and Security (2005), pp. 75–84.

[7] H. Zhong, N. Karpowicz, and X.-C. Zhang, "Terahertz emission profile from laser-induced air plasma", Applied Physics Letters **88**, 261103 (2006).

[8] H. Zhong, N. Karpowicz, J. Partridge, X. Xie, J. Xu, and X.-C. Zhang, "Terahertz wave imaging for landmine detection", in , edited by R. J. Hwu and D. L. Woolard (Sept. 8, 2004), p. 33.

[9] Y. Yang, M. Mandehgar, and D. R. Grischkowsky, "Broadband THz Signals Propagate Through Dense Fog", IEEE Photonics Technology Letters **27**, 383–386 (2015).

[10] E. R. Brown, "THz Generation by Photomixing in Ultrafast Photoconductors", International Journal of High Speed Electronics and Systems **13**, 497–545 (2003).

[11] D. H. Auston, “Picosecond optoelectronic switching and gating in silicon”, Applied Physics Letters **26**, 101–103 (1975).

[12] G. Mourou, C. V. Stancampiano, A. Antonetti, and A. Orszag, “Picosecond microwave pulses generated with a subpicosecond laser-driven semiconductor switch”, Applied Physics Letters **39**, 295–296 (1981).

[13] D. H. Auston, K. P. Cheung, and P. R. Smith, “Picosecond photoconducting Hertzian dipoles”, Applied Physics Letters **45**, 284–286 (1984).

[14] K. Cheung and D. Auston, “A novel technique for measuring far-infrared absorption and dispersion”, Infrared Physics **26**, 23–27 (1986).

[15] M. van Exter, C. Fattinger, and D. Grischkowsky, “Terahertz time-domain spectroscopy of water vapor”, Optics Letters **14**, 1128 (1989).

[16] J. R. Birch, “The far infrared optical constants of polyethylene”, Infrared Physics **30**, 195–197 (1990).

[17] D. Grischkowsky, S. Keiding, M. Van Exter, and C. Fattinger, “Far-infrared time-domain spectroscopy with terahertz beams of dielectrics and semiconductors”, JOSA B **7**, 2006–2015 (1990).

[18] P. U. Jepsen, R. H. Jacobsen, and S. R. Keiding, “Generation and detection of terahertz pulses from biased semiconductor antennas”, JOSA B **13**, 2424–2436 (1996).

[19] E. R. Brown, K. A. McIntosh, K. B. Nichols, and C. L. Dennis, “Photomixing up to 3.8 THz in low-temperature-grown GaAs”, Applied Physics Letters **66**, 285–287 (1995).

[20] S. Verghese, K. A. McIntosh, S. Calawa, W. F. Dinatale, E. K. Duerr, and K. A. Molvar, “Generation and detection of coherent terahertz waves using two photomixers”, Applied Physics Letters **73**, 3824–3826 (1998).

[21] T. Göbel, D. Stanze, B. Globisch, R. J. B. Dietz, H. Roehle, and M. Schell, “Telecom technology based continuous wave terahertz photomixing system with 105 decibel signal-to-noise ratio and 35 terahertz bandwidth”, Optics Letters **38**, 4197 (2013).

[22] N. Katzenellenbogen and D. Grischkowsky, “Efficient generation of 380 fs pulses of THz radiation by ultrafast laser pulse excitation of a biased metal-semiconductor interface”, Applied Physics Letters **58**, 222–224 (1991).

[23] M. Tani, S. Matsuura, K. Sakai, and S.-i. Nakashima, “Emission characteristics of photoconductive antennas based on low-temperature-grown GaAs and semi-insulating GaAs”, Applied optics **36**, 7853–7859 (1997).

[24] S. M. Duffy, S. Verghese, A. McIntosh, A. Jackson, A. C. Gossard, and S. Matsuura, “Accurate modeling of dual dipole and slot elements used with photomixers for coherent terahertz output power”, IEEE Transactions on Microwave Theory and Techniques **49**, 1032–1038 (2001).

[25] I. S. Gregory, W. R. Tribe, B. E. Cole, M. J. Evans, E. H. Linfield, A. G. Davies, and M. Missous, “Resonant dipole antennas for continuous-wave terahertz photomixers”, Applied Physics Letters **85**, 1622–1624 (2004).

[26] Kyungsik Moon, Haewook Han, and Ikmo Park, “Terahertz Folded Half-Wavelength Dipole Antenna for High Output Power”, in 2005 International Topical Meeting on Microwave Photonics (2005), pp. 301–304.

[27] H. Tanoto, J. H. Teng, Q. Y. Wu, M. Sun, Z. N. Chen, S. A. Maier, B. Wang, C. C. Chum, G. Y. Si, A. J. Danner, and S. J. Chua, “Nano-antenna in a photoconductive photomixer for highly efficient continuous wave terahertz emission”, Scientific Reports **3** (2013).

[28] E. A. Michael, B. Vowinkel, R. Schieder, M. Mikulics, M. Marso, and P. Kordoš, “Large-area traveling-wave photonic mixers for increased continuous terahertz power”, Applied Physics Letters **86**, 111120 (2005).

[29] B. Sartorius, H. Roehle, H. Künzel, J. Böttcher, M. Schlak, D. Stanze, H. Venghaus, and M. Schell, “All-fiber terahertz time-domain spectrometer operating at 1.5 *M*m telecom wavelengths”, Optics Express **16**, 9565 (2008).

[30] I. Gregory, W. Tribe, B. Cole, C. Baker, M. Evans, I. Bradley, E. Linfield, A. Davies, and M. Missous, “Phase sensitive continuous-wave THz imaging using diode lasers”, Electronics Letters **40**, 143 (2004).

[31] C. W. Berry and M. Jarrahi, “Terahertz generation using plasmonic photoconductive gratings”, New Journal of Physics **14**, 105029 (2012).

[32] N. Vieweg, M. Mikulics, M. Scheller, K. Ezdi, R. Wilk, H.-W. Hübers, and M. Koch, “Impact of the contact metallization on the performance of photoconductive THz antennas”, Optics express **16**, 19695–19705 (2008).

[33] Y.-S. Lee, *Principles of Terahertz Science and Technology* (Springer New York, Corvallis, Oregon, Sept. 2008).

[34] M. van Exter, C. Fattinger, and D. Grischkowsky, “High-brightness terahertz beams characterized with an ultrafast detector”, Applied Physics Letters **55**, 337–339 (1989).

[35] L. Duvillaret, F. Garet, J.-F. Roux, and J.-L. Coutaz, “Analytical modeling and optimization of terahertz time-domain spectroscopy experiments, using photoswitches as antennas”, IEEE Journal of Selected Topics in Quantum Electronics **7**, 615–623 (2001).

[36] D. Grischkowsky and N. Katzenellenbogen, “Femtosecond Pulses of Terahertz Radiation: Physics and Applications”, in OSA Proceedings on Picosecond electronics and optoelectronics, Vol. 9 (Mar. 13, 1991), pp. 9–14.

[37] E. R. Brown, F. W. Smith, and K. A. McIntosh, “Coherent millimeter-wave generation by heterodyne conversion in low-temperature-grown GaAs photoconductors”, Journal of Applied Physics **73**, 1480–1484 (1993).

[38] H. Hamster, A. Sullivan, S. Gordon, W. White, and R. W. Falcone, "Subpicosecond, electromagnetic pulses from intense laser-plasma interaction", Physical Review Letters **71**, 2725–2728 (1993).

[39] D. J. Cook and R. M. Hochstrasser, "Intense terahertz pulses by four-wave rectification in air", Optics Letters **25**, 1210 (2000).

[40] T. I. Oh, Y. S. You, N. Jhajj, E. W. Rosenthal, H. M. Milchberg, and K. Y. Kim, "Intense terahertz generation in two-color laser filamentation: energy scaling with terawatt laser systems", New Journal of Physics **15**, 075002 (2013).

[41] V. A. Andreeva, O. G. Kosareva, N. A. Panov, D. E. Shipilo, P. M. Solyankin, M. N. Esaulkov, P. González de Alaiza Martínez, A. P. Shkurinov, V. A. Makarov, L. Bergé, and S. L. Chin, "Ultrabroad Terahertz Spectrum Generation from an Air-Based Filament Plasma", Physical Review Letters **116** (2016).

[42] M. Li, W. Li, Y. Shi, P. Lu, H. Pan, and H. Zeng, "Verification of the physical mechanism of THz generation by dual-color ultrashort laser pulses", Applied Physics Letters **101**, 161104 (2012).

[43] M. Kress, T. Löffler, S. Eden, M. Thomson, and H. G. Roskos, "Terahertz-pulse generation by photoionization of air with laser pulses composed of both fundamental and second-harmonic waves", Optics Letters **29**, 1120 (2004).

[44] K.-Y. Kim, J. H. Glownia, A. J. Taylor, and G. Rodriguez, "Terahertz emission from ultrafast ionizing air in symmetry-broken laser fields", Optics Express **15**, 4577–4584 (2007).

[45] M. V. Ammosov, V. P. Krainov, and N. Delone B, "Tunnel ionization of complex atoms and of atomic ions in an alternating electromagnetic field", Soviet physics, Journal of Experimental and Theoretical Physics, 1191–1194 (1986).

[46] Q. Wu and X.-C. Zhang, "Free-space electro-optic sampling of terahertz beams", Applied Physics Letters **67**, 3523–3525 (1995).

[47] C. Kübler, R. Huber, and A. Leitenstorfer, "Ultrabroadband terahertz pulses: generation and field-resolved detection", Semiconductor Science and Technology **20**, S128–S133 (2005).

[48] O. Madelung, *Semiconductors: Data Handbook* (Springer Science and Business Media, 2012).

[49] Y. Berozashvili, S. Machavariani, A. Natsvlishvili, and A. Chirakadze, "Dispersion of the linear electro-optic coefficients and the non-linear susceptibility in GaP", Journal of Physics D: Applied Physics **22**, 682–686 (1989).

[50]M. Nagai, K. Tanaka, H. Ohtake, T. Bessho, T. Sugiura, T. Hirosumi, and M. Yoshida, "Generation and detection of terahertz radiation by electro-optical process in GaAs using 1.56 m fiber laser pulses", 4 (2014).

[51]S. Bauerschmidt, S. Preu, S. Malzer, G. H. Döhler, L. J. Wang, H. Lu, and A. C. Gossard, "Continuous wave terahertz emitter arrays for spectroscopy and imaging applications", in , edited by M. Anwar, N. K. Dhar, and T. W. Crowe (Apr. 23, 2010), p. 76710D.

[52]Z. Liu, K. Su, D. E. Gary, J. F. Federici, R. B. Barat, and Z.-H. Michalopoulou, "Video-rate terahertz interferometric and synthetic aperture imaging", Applied optics **48**, 3788–3795 (2009).

[53]S. T. Bauerschmidt, G. H. Döhler, H. Lu, A. C. Gossard, S. Malzer, and S. Preu, "Arrayed free space continuous-wave terahertz photomixers", Optics Letters **38**, 3673 (2013).

[54]N. T. Yardimci, H. Lu, and M. Jarrahi, "High power telecommunication-compatible photoconductive terahertz emitters based on plasmonic nano-antenna arrays", Applied Physics Letters **109**, 191103 (2016).

[55]G. H. Dohler, L. E. Garcia-Munoz, S. Preu, S. Malzer, S. Bauerschmidt, J. Montero-de-Paz, E. Ugarte-Munoz, A. Rivera-Lavado, V. Gonzalez-Posadas, and D. Segovia-Vargas, "From Arrays of THz Antennas to Large-Area Emitters", IEEE Transactions on Terahertz Science and Technology **3**, 532–544 (2013).

[56]N. M. Froberg, B. B. Hu, X.-C. Zhang, and D. H. Auston, "Terahertz radiation from a photoconducting antenna array", IEEE journal of quantum electronics **28**, 2291–2301 (1992).

[57]S. Preu, S. Malzer, G. H. Döhler, J. Zhang, Z. H. Lu, and L. J. Wang, "Highly collimated and directional continous-wave Terahertz emission by photomixing in semiconductor device arrays", in , edited by D. Jäger and A. Stöhr (Apr. 21, 2006), 61940F.

[58]C. W. Berry, M. R. Hashemi, and M. Jarrahi, "Generation of high power pulsed terahertz radiation using a plasmonic photoconductive emitter array with logarithmic spiral antennas", Applied Physics Letters **104**, 081122 (2014).

[59]C. Berry, M. R. Hashemi, M. Unlu, and M. Jarrahi, "Design, Fabrication, and Experimental Characterization of Plasmonic Photoconductive Terahertz Emitters", Journal of Visualized Experiments (2013).

[60]S.-H. Yang, M. R. Hashemi, C. W. Berry, and M. Jarrahi, "7.5% Optical-to-Terahertz Conversion Efficiency Offered by Photoconductive Emitters With Three-Dimensional Plasmonic Contact Electrodes", IEEE Transactions on Terahertz Science and Technology **4**, 575–581 (2014).

[61] A. Rivera-Lavado, K. Atia-Abdalmalak, G. Santamaria-Botello, D. Gonzalez-Ovejero, G. Carpintero, D. Segovia-Vargas, I. Camara-Mayorga, and L. E. Garcia-Munoz, "High-power terahertz emitter for a communication link: The chessboard array", in 2017 11th European Conference on Antennas and Propagation (EUCAP) (Mar. 2017), pp. 1377–1380.

[62] M. Theurer, T. Göbel, D. Stanze, U. Troppenz, F. Soares, N. Grote, and M. Schell, "Photonic-integrated circuit for continuous-wave THz generation", Optics Letters **38**, 3724 (2013).

[63] F. M. Soares, M. Baier, T. Gaertner, N. Grote, M. Moehrle, T. Beckerwerth, P. Runge, and M. Schell, "InP-Based Foundry PICs for Optical Interconnects", Applied Sciences **9**, 1588 (2019).

[64] H. Zhao, S. Pinna, F. Sang, B. Song, S. T. Suran Brunelli, L. A. Coldren, and J. Klamkin, "High-Power Indium Phosphide Photonic Integrated Circuits", IEEE Journal of Selected Topics in Quantum Electronics **25**, 1–10 (2019).

[65] R. Guzmán, G. Carpintero, C. Gordon, and L. Orbe, "Millimeter-wave signal generation for a wireless transmission system based on on-chip photonic integrated circuit structures", Optics Letters **41**, 4843 (2016).

[66] A. Rivera-Lavado, L. E. García-Muñoz, G. Dohler, S. Malzer, S. Preu, S. Bauerschmidt, J. Montero-de-Paz, E. Ugarte-Muñoz, B. Andrés-García, V. Izquierdo-Bermúdez, and D. Segovia-Vargas, "Arrays and New Antenna Topologies for Increasing THz Power Generation Using Photomixers", Journal of Infrared, Millimeter, and Terahertz Waves **34**, 97–108 (2013).

[67] A. I. Hernandez-Serrano, M. Weidenbach, S. F. Busch, M. Koch, and E. Castro-Camus, "Fabrication of gradient-refractive-index lenses for terahertz applications by three-dimensional printing", Journal of the Optical Society of America B **33**, 928 (2016).

[68] C. A. Balanis, *Antenna theory: analysis and design*, 2nd ed (Wiley, New York, 1997), 941 pp.

[69] J. Neu and C. A. Schmuttenmaer, "Tutorial: An introduction to terahertz time domain spectroscopy (THz-TDS)", Journal of Applied Physics **124**, 231101 (2018).

[70] T. Søndergaard, C. B. Sørensen, and E. Skovsen, "Design of a compact cylindrical micro-lens for efficient out-coupling and collimation of THz radiation from a photoconductive antenna", in 2019 44th International Conference on Infrared, Millimeter, and Terahertz Waves (IRMMW-THz) (Sept. 2019), pp. 1–2.

[71] T. Søndergaard, C. B. Sørensen, and E. Skovsen, "Design of a compact cylindrical micro-lens for efficient out-coupling and collimation of THz radiation from a photoconductive antenna", JOSA B, In review., 1–2 (2020).

[72]F. Laermer and A. Schilp, “Verfahren zum anisotropen Ätzen von Silicium”, German pat. 4241045C1 (Robert Bosch GMBH, May 26, 1994).

[73]M. H. Kristensen, “Optimization and benchmarking of a terahertz timedomain spectrometer”, Master thesis (Aalborg University, Aalborg, Aug. 6, 2017).

[74]C. B. Sørensen, T. Søndergaard, and E. Skovsen, “Experimental binary optimization of resonant dipole antennas for remote sensing below 2THz”, 43rd International Conference on Infrared, Millimeter, and Terahertz Waves (2018).

[75]K. Pearson, “Notes on Regression and Inheritance in the case of two parents”, Proceedings of the Royal Society of London **58**, 240–242 (1895).

[76]D. R. Bacon, A. D. Burnett, M. Swithenbank, C. Russell, L. Li, C. D. Wood, J. Cunningham, E. H. Linfield, A. G. Davies, P. Dean, and J. R. Freeman, “Free-space terahertz radiation from a LT-GaAs-on-quartz large-area photoconductive emitter”, Optics Express **24**, 26986 (2016).

[77]C. B. Sørensen, J. Degert, M. Tondusson, E. Skovsen, E. Freysz, and E. Abraham, “Conical vs Gaussian Terahertz Emission from Two-Color Laser-Induced Air Plasma Filaments”, in 2019 44th International Conference on Infrared, Millimeter, and Terahertz Waves (IRMMW-THz) (Sept. 2019), pp. 1–1.

[78]C. B. Sørensen, L. Guiramand, J. Degert, M. Tondusson, E. Skovsen, E. Freysz, and E. Abraham, “Conical vs Gaussian Terahertz Emission from Two-Color Laser-Induced Air Plasma Filaments”, Manuscript in preparation (2019).

[79]P. Klarskov, A. C. Strikwerda, K. Iwaszczuk, and P. U. Jepsen, “Experimental three-dimensional beam profiling and modeling of a terahertz beam generated from a two-color air plasma”, New Journal of Physics **15**, 075012 (2013).

[80]V. Blank, M. D. Thomson, and H. G. Roskos, “Spatio-spectral characteristics of ultra-broadband THz emission from two-colour photoexcited gas plasmas and their impact for nonlinear spectroscopy”, New Journal of Physics **15**, 075023 (2013).

[81]A. A. Ushakov, P. A. Chizhov, V. A. Andreeva, N. A. Panov, D. E. Shipilo, M. Matoba, N. Nemoto, N. Kanda, K. Konishi, V. V. Bukin, M. Kuwata-Gonokami, O. G. Kosareva, S. V. Garnov, and A. B. Savel’ev, “Ring and unimodal angular-frequency distribution of THz emission from two-color femtosecond plasma spark”, Optics Express **26**, 18202 (2018).

[82]Y. S. You, T. I. Oh, and K. Y. Kim, “Off-Axis Phase-Matched Terahertz Emission from Two-Color Laser-Induced Plasma Filaments”, Physical Review Letters **109** (2012).

[83] A. Gorodetsky, A. D. Koulouklidis, M. Massaouti, and S. Tzortzakis, "Physics of the conical broadband terahertz emission from two-color laser-induced plasma filaments", Physical Review A **89** (2014).

[84] A. V. Borodin, M. N. Esaulkov, I. I. Kuritsyn, I. A. Kotelnikov, and A. P. Shkurinov, "On the role of photoionization in generation of terahertz radiation in the plasma of optical breakdown", JOSA B **29**, 1911–1919 (2012).

[85] W. L. Chan, J. Deibel, and D. M. Mittleman, "Imaging with terahertz radiation", Reports on Progress in Physics **70**, 1325–1379 (2007).

[86] F. Simoens, "THz Bolometer Detectors", in *Physics and Applications of Terahertz Radiation*, Vol. 173, Springer Series in Optical Sciences (Springer, Dordrecht, Sept. 27, 2013).

[87] Q. Wu, T. D. Hewitt, and X.-C. Zhang, "Two-dimensional electro-optic imaging of THz beams", Applied Physics Letters **69**, 1026–1028 (1996).

[88] Z. Jiang, X. G. Xu, and X.-C. Zhang, "Improvement of terahertz imaging with a dynamic subtraction technique", Applied Optics **39**, 2982 (2000).

[89] E. Abraham, H. Cahyadi, M. Brossard, J. Degert, E. Freysz, and T. Yasui, "Development of a wavefront sensor for terahertz pulses", Optics Express **24**, 5203 (2016).

[90] F. Blanchard, A. Doi, T. Tanaka, H. Hirori, H. Tanaka, Y. Kadoya, and K. Tanaka, "Real-time terahertz near-field microscope", Optics Express **19**, 8277 (2011).

[91] M. Brunken, H. Genz, P. Gottlicher, C. Hessler, M. Huning, H. Loos, A. Richter, H. Schlarb, P. Schmuser, S. Simrock, D. Suetterlin, M. Tonutti, and D. Turke, "Electro-Optic Sampling at the TESLA Test Accelerator: Experimental Setup and First Results", 24 (2003).

[92] Z. Jiang, F. G. Sun, Q. Chen, and X.-C. Zhang, "Electro-optic sampling near zero optical transmission point", Applied Physics Letters **74**, 1191–1193 (1999).

[93] M. Sheik-Bahae, A. Said, T.-H. Wei, D. Hagan, and E. Van Stryland, "Sensitive measurement of optical nonlinearities using a single beam", IEEE Journal of Quantum Electronics **26**, 760–769 (1990).

[94] K.-Y. Kim, J. H. Glownia, A. J. Taylor, and G. Rodriguez, "High-Power Broadband Terahertz Generation via Two-Color Photoionization in Gases", IEEE Journal of Quantum Electronics **48**, 797–805 (2012).

[95] M. Thomson, V. Blank, and H. G. Roskos, "Terahertz white-light pulses from an air plasma photo-induced by incommensurate two-color optical fields", Optics Express **18**, 23173–23183 (2010).

[96]F. de la Peña, E. Prestat, V. Fauske, P. Burdet, P. Jokubauskas, M. Nord, T. Ostasevicius, K. MacArthur, M. Sarahan, D. Johnstone, J. Taillon, J. Lähnemann, V. Migunov, a. Eljarrat, J. Caron, T. Aarholt, S. Mazzucco, M. Walls, T. Slater, F. Winkler, pquinn-dls, B. Martineau, G. Donval, R. McLeod, E. Hoglund, I. Alxneit, D. Lundeby, T. Henninen, L. Zagonel, and A. Garmannslund, "Hyperspy/hyperspy: Hyperspy v1.5.2", Zenodo (2019).

[97]G. Vdovin and F. van Goor, *LightPipes*, version 1.2, Rijswijk, Netherlands: Flexible Optical, Dec. 2019.

[98]C. B. Sørensen and E. Skovsen, "Rapid Prototyping of Simple Optical Elements for the Terahertz Domain", in 2019 44th International Conference on Infrared, Millimeter, and Terahertz Waves (IRMMW-THz) (Sept. 2019), pp. 1–2.

[99]C. B. Sørensen, *THzOAPMs*, in collab. with A. F. Mikkelstrup and E. Skovsen, (Sept. 18, 2019) `https://github.com/cbuhl/THzOAPMs`.

[100]D. B. Fullager, S. Park, C. Hovis, Y. Li, J. Reese, E. Sharma, S. Lee, C. Evans, G. D. Boreman, and T. Hofmann, "Metalized Poly-methacrylate Off-Axis Parabolic Mirrors for Terahertz Imaging Fabricated by Additive Manufacturing", Journal of Infrared, Millimeter, and Terahertz Waves **40**, 269–275 (2019).

[101]A. D. Squires, E. Constable, and R. A. Lewis, "3D printing of aspherical terahertz lenses and diffraction gratings", in 2014 39th International Conference on Infrared, Millimeter, and Terahertz waves (IRMMW-THz) (Sept. 2014), pp. 1–2.

[102]J. Gospodaric, A. Kuzmenko, A. Pimenov, C. Huber, D. Suess, S. Rotter, and A. Pimenov, "3D-printed phase waveplates for THz beam shaping", Applied Physics Letters **112**, 221104 (2018).

[103]S. Pandey, B. Gupta, and A. Nahata, "Terahertz plasmonic waveguides created via 3D printing", Optics Express **21**, 24422 (2013).

[104]A. I. Hernandez-Serrano, "Terahertz quasi-optical devices fabricated by 3D printing", PhD Thesis (Centro de Investigaciones en Óptica A.C., Leon, Mexico, Mar. 2018).

[105]A. D. Squires, "Terahertz Technology and Applications: 3D Printing and Art Conservation" (The University of Wollongong, Wollongong, Nov. 2017).

[106]X. Lin, Y. Rivenson, N. T. Yardimci, M. Veli, Y. Luo, M. Jarrahi, and A. Ozcan, "All-optical machine learning using diffractive deep neural networks", Science **361**, 1004–1008 (2018).

[107]H. Guerboukha, K. Nallappan, Y. Cao, M. Seghilani, J. Azaña, and M. Skorobogatiy, "Planar Porous Components for Low-Loss Terahertz Optics", Advanced Optical Materials **7**, 1900236 (2019).

[108]A. Bandyopadhyay, A. Sengupta, V. Johnson, J. A. Harrington, and J. F. Federici, "Characterization of hollow polycarbonate metal waveguides using Terahertz time domain spectroscopy", in , edited by R. J. Hwu and K. J. Linden (Feb. 9, 2006), 61200B.

[109]R. Bernasconi, G. Natale, M. Levi, and L. Magagnin, "Electroless Plating of NiP and Cu on Polylactic Acid and Polyethylene Terephthalate Glycol-Modified for 3D Printed Flexible Substrates", Journal of The Electrochemical Society **163**, D526–D531 (2016).

[110]Ş. Macit and C. Uraz, "Electroless Cu Plating on ABS Plastic by Using Environmentally Friendly Chemicals", Deu Muhendislik Fakultesi Fen ve Muhendislik **20**, 369–375 (2018).

[111]H. E. Bennett, "Specular Reflectance of Aluminized Ground Glass and the Height Distribution of Surface Irregularities", Journal of the Optical Society of America **53**, 1389 (1963).

[112]J. E. Harvey, N. Choi, S. Schroeder, and A. Duparré, "Total integrated scatter from surfaces with arbitrary roughness, correlation widths, and incident angles", Optical Engineering **51**, 013402 (2012).

[113]J. E. Frylund, *Ra ved forskellige bearbejdningsmetoder*, (Jan. 1, 2008) `http://www.fagteori.dk/maaling/overfladeruhed/opnaaelig-overfladeruhed.aspx` (visited on 09/27/2019).

[114]M. S. Alsoufi and A. E. Elsayed, "How Surface Roughness Performance of Printed Parts Manufactured by Desktop FDM 3D Printer with PLA+ is Influenced by Measuring Direction", American Journal of Mechanical Engineering **5**, 211–222 (2017).

[115]C. B. Sørensen, A. F. Mikkelstrup, and E. Skovsen, "Rapid Prototyping of Simple Optical Elements for the Terahertz Domain", Poster, IRMMWTHz 2019 (Paris), Sept. 4, 2019.

[116]U. Government, *Federal Specification GGG-P-463c*, Sept. 12, 1973.

[117]G. Arfken, *Mathematical Methods for Physicist*, 3rd (Academic Press, 1985), 198-200.

[118]Y. H. Lo and R. Leonhardt, "Aspheric lenses for terahertz imaging", Optics Express **16**, 8 (2008).

Appendix A

Papers and abstracts

This section contains the list of publications that have been published during the project, with a significant body of work by the author:

Experimental binary optimization of resonant dipole antennas for remote sensing below 2 THz C. B. Sørensen, T. Søndergaard and E. Skovsen. *2018 43rd International Conference on Infrared, Millimeter, and Terahertz Waves (IRMMW-THz)*

Rapid Prototyping of Simple Optical Elements for the Terahertz Domain C. B. Sørensen and E. Skovsen. *2019 44th International Conference on Infrared, Millimeter, and Terahertz Waves (IRMMW-THz)*

Conical vs Gaussian Terahertz Emission from Two-Color Laser-Induced Air Plasma Filaments C. B. Sørensen, J. Degert, M. Tondusson, E. Skovsen, E. Freysz and E. Abraham. *2019 44th International Conference on Infrared, Millimeter, and Terahertz Waves (IRMMW-THz)*

Conical vs Gaussian emission profiles of terahertz radiation generated in two-color plasmas C. B. Sørensen, J. Degert, M. Tondusson, E. Skovsen, E. Freysz and E. Abraham. *Manuscript in preparation*.

The author has also provided limited contributions to:

Design of a compact cylindrical micro-lens for efficient out-coupling and collimation of THz radiation from a photoconductive antenna T. Søndergaard, C. B. Sørensen and E. Skovsen. *2019 44th International Conference on Infrared, Millimeter, and Terahertz Waves (IRMMW-THz)*

Theoretical analysis of compact cylindrical micro-lenses for THz photoconductive antennas T. Søndergaard, M. Sauer, C. E. M. Nielsen, L. Merring-Mikkelsen, C. B. Sørensen and E. Skovsen. *JOSA B, submitted for peer-review 26/9-19*.

Appendix B

Cleanroom standard operating procedures

This appendix is provided as a functional starting point for fabrication. It describes the fabrication procedure for photoconductive antennas, but it will work for general geometries on GaAs, with a feature size greater than 3um.

Three SOP's are enclosed. They contain the wafer-scale fabrication steps for the rectilinear arrays, as well as the die-scale steps regarding the EBL process.

Lastly, the wafer scale process description for the slanted feedline array fabrication.

Fabrication procedure for rectilinear array antennas

Date: 2019-11-08
Tags:
Created by: Christian SØRENSEN

Wafer scale fabrication

Step #	Step description	Details	Comments
1	**Starting wafer**	4" GaAs wafer, DSP. mi(100)	
SiO2 PE CVD			
2	**Cleaning**	15 minutes sonication with acetone, w-i-w rinse with ethanol, spindry. 15min O2 oxyclean program, 300W, immediate transfer to PE CVD oven	
3	**SiO2 PE CVD**	40nm SiO2 Use hfsio2-w program, for 65s. Rate: 100nm/min, gives ca 80nm. Immediate transfer to spin coater	Warm up the PE CVD a day before. Use program ROOMTEMP to go to vacuum, and go onwards to the chosen program to warm up. The isotropic etch gives very slopy sidewalls - thus I can use much thicker SiO2 layers.
Contact pad definition			
4	**Spin on photoresist (ma-N 1410)**	2000rpm to spin to 1.0um, 60s. Keep syringe inserted to avoid excessive drying in the center	
5	**Solvent bakeout**	160degC, 90s, hotplate, cool on metal block.	
6	**UV exposure**	450mJ/cm2 (standard), 11s in maskaligner	
7	**Developer**	maD 533, neat, 120s	
8	**Rinse and Dry**	Submerge in water, and agitate carefully. Rough and fine rinse.	
9	**Flood exposure**	30s in maskaligner	
10	**PVD/etch**	PVD: 3nm Ti, 150nm Au, Sputtercoater 56s Au, 11s Ti	

Fabrication procedure for rectilinear array antennas

Date: 2019-11-08
Tags:
Created by: Christian SØRENSEN

11	**Lift-off**	Remove the bulk of the gold with hot acetone. Afterwards, rinse and use ultrasonication lvl5, 15 minutes. Remove during sonication to avoid scattering particles.	
Oxide Window definition			
12	**Spin on photoresist (ma-N 1410)**	2000rpm to spin to 1.0um, 60s. Keep syringe inserted to avoid excessive drying in the center	
13	Solvent bakeout	160degC, 90s, hotplate, cool on metal block	
14	UV exposure	11s	
15	Developer	maD 533, neat, 120s	
16	Rinse and dry	Submerge in water and agitate carefully. Rough and fine rinse	
17	Flood exposure	30s in mask aligner	
18	Etch	BHF etch (70nm/min = 1.1min etch) Use 4 mins. Transfer to water and rinse carefully	
19	Cleaning	Rinse with acetone, hot acetone 20 mins, rinse with acetone, rinse with ethanol, spin dry.	
EBL resist deposition			
20	Cleaning	1min 300W O2 plasma, transfer directly to spincoater.	Expected to remove 20nm of oxide
21	Spin on MMA	Dispense to cover, MMA 8.5 in ethyl lactate. Spin at 2500rpm, keep syringe inserted.	
22	Bakeout	30s, hotplate, 180degC	
23	Spin on PMMA	Dispense to cover, PMMA 950k C2. Spin at 2500rpm	
24	Bakeout	30s, hotplate, 180degC	
25	Dicing	Use great care, clean gloves and light scribes.	

End of wafer scale fabrication			

Die scale fabrication:

Step #	Step description	Details	Comments
	Starting substrate	From step 25.	
26	**Expose in XB**	Standard: 80uC/cm2, 10keV, 270pA. Double exposure to avoid charging.	
27	**PMMA Develop**	45s in MIBK:IPA 1:3,	
28	**Rinse and dry**	IPA/CDA	
29	**Plasma Descum**	10s, 30W, 100 sccm O_2 flow	
30	**Oxide Etch**	HCl:H_2O 3:10 vol, 30s. Immediate transfer to rinse, then to beaker containing water to avoid oxide build up. Dry and transfer quickly.	
31	**PVD of Ti/Au**	Ebeam coater, 2nm Cr, 70nm Au.	Preferably pump to 2e-6mbar.
32	**Perform lift off.**	10 min, warm acetone. Set hotplate to 100degC.	

Unique eLabID: 20191108-19b7714a18f2f9c437955acecc0c43a4b1557de2
link : https://elabftw.nano.aau.dk:443/experiments.php?mode=view&id=234

Fabrication procedure for slanted feedline antennas

Date: 2019-11-08
Tags:
Created by: Christian SØRENSEN

Step #	Step description	Details	Comments
1	**Starting wafer**	4" GaAs wafer, DSP. mi(100)	
SiO2 PE CVD			
2	**Cleaning**	15 minutes sonication with acetone, w-i-w rinse with ethanol, spindry. 15min O2 oxyclean program, 300W, immediate transfer to PE CVD oven	
3	**SiO2 PE CVD**	40nm SiO2 Use hfsio2-w program, for 65s. Rate: 100nm/min, gives ca 80nm. Immediate transfer to spin coater	Warm up the PE CVD a day before. Use program ROOMTEMP to go to vacuum, and go onwards to the chosen program to warm up. The isotropic etch gives very slopy sidewalls - thus I can use much thicker SiO2 layers.
Alignment marker definition			
4	**Spin on photoresist (ma-N 1410)**	2000rpm to spin to 1.0um, 60s. Keep syringe inserted to avoid excessive drying in the center	
5	**Solvent bakeout**	160degC, 90s, hotplate, cool on metal block.	
6	**UV exposure**	450mJ/cm2 (standard), 11s in maskaligner	
7	**Developer**	maD 533, neat, 120s	
8	**Rinse and Dry**	Submerge in water, and agitate carefully. Rough and fine rinse.	
9	**Flood exposure**	30s in maskaligner	
10	**PVD/etch**	PVD: 3nm Ti, 50nm Au, Sputtercoater 25s Au, 11s Ti	
11	**Lift-off**	Remove the bulk of the gold with hot acetone. Afterwards, rinse and use ultrasonication lvl5, 15 minutes. Remove during sonication to avoid scattering particles.	Note that a very large vat of acetone is highly suggested - if the wafer is held vertically in the acetone, re-deposition of gold particles is highly decreased.

Fabrication procedure for slanted feedline antennas

Date: 2019-11-08
Tags:
Created by: Christian SØRENSEN

Oxide Window definition			
12	**Spin on photoresist (ma-N 1410)**	2000rpm to spin to 1.0um, 60s. Keep syringe inserted to avoid excessive drying in the center	
13	Solvent bakeout	160degC, 90s, hotplate, cool on metal block	
14	UV exposure	11s	
15	Developer	maD 533, neat, 120s	
16	Rinse and dry	Submerge in water and agitate carefully. Rough and fine rinse	
17	Flood exposure	30s in mask aligner	
18	Etch	BHF etch (70nm/min = 1.1min etch) Use 4 mins. Transfer to water and rinse carefully	
19	Cleaning	Rinse with acetone, hot acetone 20 mins, rinse with acetone, rinse with ethanol, spin dry.	
Contact pad and antenna definition			
20	**Spin on photoresist (ma-N 1410)**	2000rpm to spin to 1.0um, 60s. Keep syringe inserted to avoid excessive drying in the center	
21	**Solvent bakeout**	160degC, 90s, hotplate, cool on metal block.	
22	**UV exposure**	450mJ/cm2 (standard), 11s in maskaligner	
23	**Developer**	maD 533, neat, 120s	
24	**Rinse and Dry**	Submerge in water, and agitate carefully. Rough and fine rinse.	
25	**Flood exposure**	30s in maskaligner	
26	**PVD/etch**	PVD: 3nm Ti, 150nm Au, Sputtercoater 56s Au, 11s Ti	

27	**Lift-off**	Remove the bulk of the gold with hot acetone. Afterwards, rinse and use ultrasonication lvl5, 15 minutes. Remove during sonication to avoid scattering particles.	
28	**Dicing**	Using the Disco DAD321 saw.	
End of wafer scale fabrication			

Unique eLabID: 20191108-fa7e2a4155eebc8009928ea3317daaa872419323
link : https://elabftw.nano.aau.dk:443/experiments.php?mode=view&id=236

Appendix C

Implementation of estimators

This appendix provides the estimators that have been used for analysis of the terahertz signals in section 6.2.4. Note that each sample measurement is loaded into an object (`obj`), that immediately subtracts a baseline polynomial and calculates the fourier transform. These are available as `obj.time_signal` and `obj.freq_signal`, respectively. Other relevant constants such as the frequency bin vector `obj.freqs`, the sample frequency `obj.fs`, and the delay per step `obj.T` are available as well.

```python
import scipy.signal as ssig
import numpy as np


def find_nearest(a, a0, mode='index'):
    idx = np.abs(a - a0).argmin()
    if mode=='value':
        return a.flat[idx]
    elif mode=='index':
        return idx
    else:
        print('Mode error. Use either index or value')
        return -1


def smooth(sigin, n):
    kernel = ones(n)/n
    return ssig.fftconvolve(sigin, kernel, mode= 'same')


def rms(inp):
    return np.sqrt(np.mean(inp**2))


def dynamic_range(yf, mode = 'dB'):
    l = len(yf)
    RMSnoise = rms(yf[int(l/2):])
    if mode == 'dB':
        return 20*np.log10(yf/RMSnoise)
    elif mode == 'linear':
        return yf/RMSnoise
    else:
        print('Wrong mode. Specify either dB(default) or linear')


def estimator_1THz(obj):
    indx1THz = find_nearest(obj.freqs, 1e12)
    #Calculate the integrated signal strength:
    return dynamic_range(obj.freq_signal, mode='dB')[indx1THz]


def estimator_05THz(obj):
    indx05THz = hf.find_nearest(obj.freqs, 5e11)
    #Calculate the integrated signal strength:
    return dynamic_range(obj.freq_signal, mode='dB')[indx05THz]


def estimator_signal_strength(obj):
    #Calculate the peak signal dynamic range:
    return np.max(dynamic_range(obj.freq_signal, mode='dB'))
```

```python
def estimator_signal_bandwidth95(obj):
    csum = np.cumsum(smooth(dynamic_range(obj.freq_signal,
    mode='linear'), 50))
    indx = np.searchsorted(csum/csum.max(), 0.95)
    bw = obj.freqs[ indx ] /1e12
    return bw


def estimator_signal_bandwidth99(obj):
    f, y = ssig.welch(obj.time_signal, fs=obj.fs,
    scaling='density', nperseg=2000, noverlap=50)
    csum = np.cumsum(smooth(dynamic_range(y, mode='linear'), 1))
    indx = np.searchsorted(csum/csum.max(), 0.99)
    bw = obj.freqs[ indx ] /1e12
    return bw


def estimator_max_linear_freq(obj):
    y = smooth(dynamic_range(obj.freq_signal, mode='linear'), 10)
    return np.max(y)


def estimator_robust_bw(obj):
    def searchbw(vec, a0):
        #Backwards search to a specific value
        bwpos = 0
        l = len(vec)
        for i in range(l):
            if vec[-i-1] >= a0:
                bwpos = l-i-1
                break
        return bwpos
    #Calculate the integrated signal strength:
    DR = smooth(dynamic_range(obj.freq_signal), 10)
    indx = searchbw(DR, 15)
    return obj.freqs[indx]/1e12
```

Appendix D

Balanced photodiode amplifier

The following page contains the schematic for a balanced photodiode that was developed and used in the antenna characterisation.

It provides a measured bandwidth of 35 kHz. The expected bandwidth of the first amplifier stage is 72 kHz, not taking the photodiode capacitance into account. Only the first stage amplifier has been useful, as a gain of 1000 has been sufficient. A faster detector may be achieved by distributing the gain between the two.

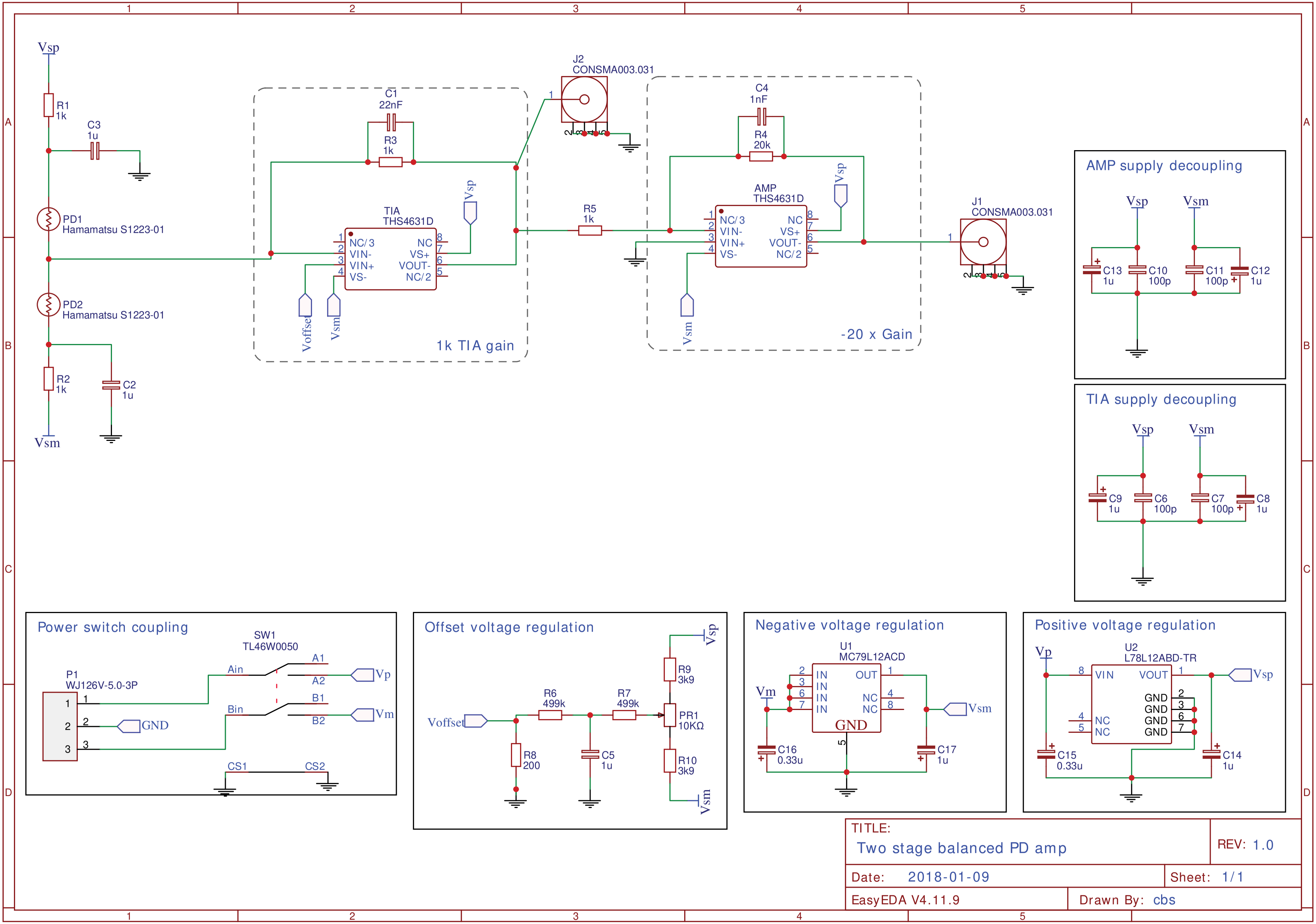

Vsp
R1
1k
C3
1u
PD1
Hamamatsu S1223-01
PD2
Hamamatsu S1223-01
R2
1k
C2
1u
Vsm
C1
22nF
R3
1k
TIA
THS4631D
NC/3
VIN-
VIN+
VS-
NC
VS+
VOUT-
NC/2
Voffset
1k TIA gain
J2
CONSMA003.031
R5
1k
C4
1nF
R4
20k
AMP
THS4631D
-20 x Gain
J1
CONSMA003.031
AMP supply decoupling
C13
1u
C10
100p
C11
100p
C12
1u
TIA supply decoupling
C9
1u
C6
100p
C7
100p
C8
1u
Power switch coupling
SW1
TL46W0050
P1
WJ126V-5.0-3P
Ain
Bin
A1
A2
B1
B2
CS1
CS2
GND
Vp
Vm
Offset voltage regulation
R6
499k
R7
499k
R8
200
C5
1u
R9
3k9
PR1
10KΩ
R10
3k9
Negative voltage regulation
U1
MC79L12ACD
IN
OUT
NC
GND
C16
0.33u
C17
1u
Positive voltage regulation
U2
L78L12ABD-TR
VIN
VOUT
C15
0.33u
C14
1u
TITLE:
Two stage balanced PD amp
REV: 1.0
Date: 2018-01-09
Sheet: 1/1
EasyEDA V4.11.9
Drawn By: cbs

ISSN (online): 2446-1636
ISBN (online): 978-87-7210-577-2
AALBORG UNIVERSITY PRESS